



seit 1558

**Tip-enhanced Raman Spectroscopy (TERS) for Biomolecular
Analysis at Nanometer / Sub-nanometer Scale**

Dissertation

zur Erlangung des akademischen Grades
doctor rerum naturalium (Dr. rer. nat.)

vorgelegt dem Rat der Chemisch-Geowissenschaftlichen Fakultät der
Friedrich-Schiller-Universität Jena von Master-Chemiker

Xiu-Mei Lin

geboren am 29.09.1982 in Fujian China

1. Gutachter:

2. Gutachter:

3. Datum der öffentlichen Verteidigung:

This thesis is dedicated to my father Xianxing Qian, my mother Meijiao Lin, my husband Yanxin Chen, and my beloved daughter Sixuan Chen.



Contents

List of Abbreviations.....	v
-----------------------------------	----------

Zusammenfassung und Ausblick.....	vii
--	------------

Chapter 1 Introduction.....	1
------------------------------------	----------

Chapter 2 From Raman via SERS to TERS.....	6
---	----------

2.1 Raman spectroscopy.....	7
2.2 Surface-enhanced Raman spectroscopy (SERS).....	10
2.2.1 The discovery of SERS.....	10
2.2.2 The enhancement mechanism of SERS.....	11
2.3 Tip-enhanced Raman spectroscopy (TERS).....	14
2.3.1 The theoretical proposal and experimental realization of TERS.....	14
2.3.2 The enhancement mechanism of TERS.....	16
2.3.3 TERS instrumentation.....	16
2.3.3.1 Different SPM feedback systems in TERS	16
2.3.3.2 Different illumination / collection geometries in TERS.....	18
2.3.3.3 The fabrication of TERS tips.....	19
2.3.3.4 The choice for the optimal TERS configuration.....	20
2.3.4 The high spectral sensitivity in TERS-single molecule (SM)-TERS.....	20
2.3.5 The high lateral resolution in TERS.....	23
2.3.6. The spectral fluctuation in TERS.....	24
2.4 References.....	25

Chapter 3 Experimental part	28
--	-----------

3.1 TERS setup in the present work.....	28
3.2 The preparation of TERS tips and SERS substrates.....	29
3.3 Sample preparation.....	30

Contents

3.4 How to do a TERS measurement.....	30
3.5 References.....	31
Chapter 4 TERS for label-free DNA sequencing.....	32
4.1 The aim in this chapter	32
4.2 Introduction.....	32
4.2.1 Structure of DNA and RNA.....	33
4.2.2 DNA sequencing and detection methods.....	34
4.2.2.1 Nanopore method.....	35
4.2.2.2 STM method.....	36
4.2.2.3 SERS method.....	38
4.2.2.4 TERS method.....	40
4.3 Materials and methods.....	41
4.3.1 Materials.....	41
4.3.2 Sample preparation.....	41
4.3.3 TERS measurements.....	42
4.4 Results and discussion.....	42
4.4.1 Proposal of DNA sequencing using TERS.....	42
4.4.2 Important experimental prerequisites required for the realization of DNA sequencing using TERS	45
4.4.3 TERS spectra of uracil homopolymer – reproducibility of TERS spectra....	46
4.4.4 TERS spectra of calf thymus DNA – detection of all four DNA nucleobases and observation of sequence change.....	51
4.4.5. TERS spectra of a (A ₁₀ C ₁₅) ₈ DNA single strand – distinction of adenine and cytosine nucleobases at sub-nanometer resolution and the sequence reading information in the TERS spectra.....	56
4.5 Conclusion and outlook.....	64
4.6 References.....	64
Chapter 5 TERS for the direct detection of 5-methylcytosine sites on DNA strands.....	68

Contents

5.1. The aim of this chapter.....	68
5.2 Introduction: epigenetics and DNA methylation.....	68
5.3 Materials and methods.....	71
5.3.1 Materials.....	71
5.3.2 Sample preparation and TERS measurements.....	71
5.4 Results and discussion.....	71
5.5 Conclusion and outlook.....	77
5.6 References.....	78

Chapter 6 AFM-TERS investigations on skin penetration of invasomes.80

6.1 The aim of this chapter	80
6.2 Introduction.....	80
6.2.1 Skin barrier and penetration pathway.....	80
6.2.2 Liposomes as tools for the skin drug delivery.....	83
6.3 Materials and methods.....	86
6.3.1 Materials.....	86
6.3.2 Preparation of invasomes.....	86
6.3.3 Skin preparation	87
6.3.4 Franz diffusion cell preparation.....	87
6.3.5 Tape Stripping of the stratum corneum (SC).....	88
6.3.6 AFM, SERS and TERS measurements.....	88
6.4 Results and discussion.....	89
6.4.1 AFM measurements on control and invasomes treated SC.....	89
6.4.2 Spectra measurements.....	94
6.5 Conclusion and outlook.....	98
6.6 References.....	99

Chapter 7 Summary and outlook.....101

Publications and manuscripts in preparation.....103

Contents

Conference posters.....103

Acknowledgments.....105

Selbstständigkeitserklärung.....107

Curriculum Vitae.....108

List of Abbreviations

List of Abbreviations

TERS:	Tip-enhanced Raman spectroscopy
SERS:	Surface-enhanced Raman spectroscopy
LSP:	Localized surface plasmons
EM:	Electromagnetic
CT:	Charge transfer
RRS:	Resonance Raman scattering
HOMO:	Highest occupied molecular orbital
LUMO:	Lowest unoccupied molecular orbital
IR:	Infrared
DNA:	Deoxyribose nucleic acid
ssDNA:	Single-stranded DNA
dsDNA:	Double-stranded DNA
RNA:	Ribonucleic acid
PCR:	Polymerase chain reaction
5meC:	5-methylcytosine
CpGs:	Cytosine–phosphate–guanosine dinucleotides
SC:	Stratum corneum
SPM:	Scanning probe microscope
AFM:	Atomic force microscopy
STM:	Scanning tunneling microscope
SFM:	Shear force microscopy
SWNT:	Single-walled carbon nanotube
SM:	Single molecule
A:	Adenine; G: Guanine; C: Cytosine; T: Thymine; U: Uracil
UHV:	Ultra-high vacuum
SNR:	Signal-to-noise ratio
HEPES:	4-(2-hydroxyethyl)-1-piperazineethanesulfonic acid
LPC:	Lysophosphatidylcholine
POPC:	1-palmitoyl-2-oleoyl-sn-glycero-3-phosphocholine

Zusammenfassung und Ausblick

Für die vorliegende Arbeit machte man sich die hohe spektrale Spezifität, Empfindlichkeit und extrem hohe laterale Auflösung der Spitzen-verstärkten Raman Spektroskopie (tip-enhanced Raman scattering - TERS) zunutze, um Biomoleküle im Nano/ Sub-Nanometerbereich zu untersuchen.

TERS für die Marker-freie DNA Sequenzierung

Es wurden TERS Experimente an verschiedenen DNS/RNS Einzelsträngen durchgeführt, um die Eignung von TERS als Marker-freie Sequenzierungsmethode zu überprüfen. In ersten TERS Messungen an Uracil Homopolymersträngen konnte die Reproduzierbarkeit dieser Methode anhand von einheitlichen Spektren deutlich herausgestellt werden.

In TERS Spektren einer Kalbsthymus DNS Probe wurden alle vier verschiedenen Nukleobasen detektiert werden, wobei es Anzeichen einer Sequenzänderung unter der Spitze gab.

Die Untersuchungen wurden auf speziell für diese Arbeit synthetisierte DNS Proben ausgedehnt. So konnten in den TERS Spektren von $(A_{10}C_{15})_8$ DNS Einzelsträngen die Nukleobasen Adenin und Cytosin mit einer lateralen Auflösung im Subnanometerbereich unterschieden werden.

Aus diesen Ergebnissen lässt sich schließen, dass TERS das Potential zur direkten DNS/RNS Sequenzierung hat, wobei diese Methode für andere kettenförmige Biomakromoleküle (z. B. Proteine) zum Einsatz kommen könnte. In zukünftigen Projekten soll TERS auf synthetische DNA Stränge bekannter Sequenz mit allen vier Nukleobasen angewandt werden. Das ultimative Ziel ist die Untersuchung von Strängen mit einer unbekannten Abfolge der Nukleobasen.

Zusammenfassung und Ausblick

TERS zur direkten Detektion von 5-Methylcytosine substituierten DNS Strängen

Zum ersten Mal wurden TERS Messungen an methylierten DNS Einzelsträngen des Typs $(A_{10}5meC_{10})_4$ durchgeführt. Anhand von Markerbanden konnten in den Spektren deutlich verschiedene Schwingungsmoden für Adenin und 5-Methylcytosin zugeordnet werden. Weiterhin war es möglich, die Nukleobase Cytosin in der unsubstituierten DNS $(A_{10}C_{15})_8$ von 5-Methylcytosin in der methylierten DNS $(A_{10}5meC_{10})_4$ anhand zusätzlicher Methylgruppenbande in den TERS Spektren zu unterscheiden. Diese Ergebnisse zeigen deutlich, dass es möglich ist, 5-Methyl substituierte Cytosineinheiten in DNS Strängen mit TERS mit Subnanometerauflösung zu detektieren und zu lokalisieren. Gleichzeitig kann die Nukleobase von ihrem unsubstituierten Analogon unterschieden werden.

Weitere Untersuchungen auf diesem Gebiet werden sich auf die Identifizierung von Stickstoff methylierten Basen (N-4-Methylcytosin, N-6-Methyladenin) in DNS Strängen konzentrieren. Das Ziel ist die direkte Lokalisierung derartig substituierter Stellen. Dies könnte einen Schritt Richtung klinischer Diagnostik und Therapie darstellen.

AFM-TERS Untersuchungen auf Penetration von Invasomen in die Haut

Im Rahmen dieser Arbeit wurden AFM und TERS Messungen an verschiedenen (mit Klebeband abgezogenen) unbehandelten und mit Invasomen behandelten äußeren Hautschichten (Stratum Corneum, SC) durchgeführt. Es wurde gezeigt, dass Invasome wahrscheinlich als Medikamenten Transportsysteme fungieren, durch die intakte Vesikel 7-10 μm tief in das SC eindringen können. Die Invasome wurden spektroskopisch identifiziert und konnten somit von ihrer Umgebung (SC) unterschieden werden. Diese ersten Ergebnisse zeigen, dass der Mechanismus der Penetration von Invasomen in die Haut mit TERS untersucht werden kann. Für eine systematische Studie auf diesem Gebiet sind allerdings weitere Messungen im Hinblick auf statistische relevante Daten nötig.

Zusammenfassend kann gesagt werden, dass die Ergebnisse der hier vorliegenden Arbeit deutlich das Potential von der Spitzen-verstärkten Raman Spektroskopie (TERS) aufzeigen:

Zusammenfassung und Ausblick

zum einen ist sie für eine Marker-freie Sequenzierung von DNS / RNS Strängen geeignet, zum anderen ist eine direkte Detektion von methylierten Stellen in DNS Strängen möglich. Schließlich wurde gezeigt, dass mit TERS der Mechanismus des Eindringens von Invasomen in die Haut untersucht werden kann.

All diese Ergebnisse machen deutlich, dass die besonderen Eigenschaften von TERS (laterale Auflösung im Nanometerbereich und darunter, hohe Empfindlichkeit und Spezifität) eine Vielzahl von Untersuchungen auf dem Gebiet der Biowissenschaften ermöglichen, um bislang ungeklärte Fragen zu beantworten.

Chapter 1: Introduction

With the advantage of obtaining qualitative and at least semi-quantitative information of specimens real-time and non-invasively, vibrational spectroscopy techniques, as for instance, infrared (IR) and Raman have become more and more important in the analysis of biomolecular samples. Although the sensitivity and spatial resolution of these techniques are sufficient for numerous applications, the detection and analysis of biosamples at very low concentration (single molecule) and high spatial resolution (nanometer/sub-nanometer scale) requires more powerful techniques.

Raman scattering (1) is an intrinsically weak inelastic scattering process with cross sections smaller than infrared spectroscopy and fluorescence (2). To overcome these inherently low Raman cross sections and increase the weak Raman signals, surface-enhanced Raman scattering (SERS) (3-5) was introduced. In SERS, noble metals (eg. Au, Ag, and Cu) rough nanoparticles are used to generate localized surface plasmons (LSP) (6) on the surface. When the sample is located close to metal surface, the incident photons couple with the surface plasmons, which enhances Raman scattering. SERS provides large signal enhancement up to a factor of 10^6 - 10^{12} enabling single molecule detection (7, 8). The main obstacles associated with SERS are the inhomogeneity of the field enhancement across the substrate and the spatial resolution. The different shapes, sizes and roughness of aggregated nanoparticles result in strong variations of the field enhancement and consequently the Raman signal. Therefore a quantitative analysis of samples using SERS is challenging. Furthermore, the resolution of SERS is still limited to 200-250 nm by the Abbe diffraction limit (9). The majority of the obtained SERS signal is an average information of the chemical components in the irradiated region.

Tip-enhanced Raman spectroscopy (TERS) (10-12) overcomes the mentioned obstacles of SERS by exchanging the “mass particle substrate” through one single particle that is attached to the apex of the scanning probe microscope (SPM) tip. TERS is the combination of Raman spectroscopy and SPM, which is realized by scanning the noble metal coated or metalized SPM tip across the sample surface to obtain the topography images and to record the enhanced Raman signal simultaneously. In TERS, as only one single nanoparticle is

Chapter 1

used as enhancement source, the electromagnetic enhancement effect is constant. Furthermore, in TERS, the strong electric fields confined to the vicinity of the metal tip providing high spatial resolution as well as an enormous signal enhancement. To date, the reported highest experimental lateral resolution is 2-3 nm (13-15) and the detection limit is single molecule sensitivity (16-19).

Taking advantage of the promising features of TERS, many open questions in biological science could be investigated. Here we put our emphasis on nanoscale samples like ribonucleic acid (RNA), DNA, methylated DNA and flexible liposomes (invasomes) treated skin. Consequently, this thesis is organized as follows.

In Chapter 2, the general principles of Raman scattering, the SERS enhancement mechanism and the evolution from Raman via SERS to TERS are outlined or described in detail. Also, the principle of TERS, the variety of TERS experimental setups employed to date, the promising features of TERS (high spectral sensitivity and high lateral resolution) and the special effect (spectral fluctuation) in TERS are introduced in this chapter.

Chapter 3 is the experimental part of this thesis. The TERS setups used in the present work, the preparation of TERS tips and SERS substrates, the general methods of sample preparation (for each sample, any special sample preparation procedure will be described in the corresponding chapter), and the procedure of doing TERS measurements are introduced in this chapter.

Chapter 4 is focused on TERS for label-free DNA sequencing. DNA sequencing deciphers the role of genetic variation among individuals, which is central to modern molecular biology. The Sanger method (20) is very robust and has been the dominant method of the DNA sequencing for some 30 years. It is based on the polymerase chain reaction (PCR) amplification and other modifications of the molecules, which is procedurally complex and needs large number of reagents. Improvements in DNA sequencing are being developed and current advances show a tendency towards a label-free and direct sequencing with reasonable costs and expenditure of time (21). Providing the inherently distinguishable

Chapter 1

fingerprint information of the four DNA nucleobases, high spectral sensitivity and lateral resolution, TERS is applied for direct DNA sequencing (19). In this chapter, TERS measurements on single stranded uracil homopolymer, calf thymus DNA and $(A_{10}C_{15})_8$ are investigated and discussed. Namely, the reproducibility of TERS, the detection of all four DNA nucleobases (adenine, cytosine, guanine, and thymine) and the distinction of different DNA nucleobases with TERS at sub-nanometer lateral resolution were investigated. This demonstrates the feasibility of TERS as an alternative direct DNA sequencing method.

Chapter 5 is the investigation of TERS for direct 5-methylcytosine sites detection on methylated DNA strands. Although DNA methylation changes the chemical structure of individual bases without changing the DNA sequence, it alters the gene expression and is believed to result in frequently deleterious phenotypic changes, such as cancer (22). Methylation of DNA cytosine residues at the carbon-5 position (5-methylcytosine, 5meC) in DNA strands is the most common chemical modification in DNA methylation. Typical biological methods for detecting DNA methylation sites include bisulphate conversion, endonuclease digestion, and affinity enrichment (23). All these methods require multiple-step sample preparation with chemicals that may induce additional chemical modifications in the DNA and interfere with the detection of modified DNA. With the above mentioned promising features, in this chapter, TERS measurements on methylated single stranded DNA $(A_{10}5meC_{10})_4$ were performed. The obtained spectra not only demonstrate the direct detection of 5-methylcytosine sites on DNA strands using TERS, and also further confirm the feasibility of TERS for label-free biopolymer sequencing.

In chapter 6, skin penetration of flexible liposomes (invasomes) is investigated via TERS. Invasomes offer a promising strategy for successfully improving skin drug delivery. In general, molecular aspects of the mechanism of invasomes penetrating through the skin are not available. Raman and IR have been previously used in the study of interactions of invasome vesicles with skin and provided important information at the spatial resolution of a few hundred nanometers (24-26). However the size of the invasome vesicles is about 50 to 200nm in diameter, which is smaller than the spatial resolution Raman and IR can achieve. This challenge can be achieved by TERS. On one hand, the topography imaging

Chapter 1

capability of AFM can provide the morphology of the control and invasomes treated skin sample at nanometer spatial resolution. This can provides the physical state changes in both the exogenous (invasomes) and endogenous (skin) components. On the other hand, the spectroscopic capability of TERS can be used to identify those changes at a molecular level. The obtained primary AFM, SERS and TERS results show the promising prospects but also the challenges of the project.

Chapter 7 summarizes my PhD thesis and concludes with a future outlook.

References

1. C. V. Raman, K. S. Krishnan, A new type of Secondary Radiation. *Nature* **121**, 501 (1928).
2. N. Hayazawa, Y. Inouye, Z. Sekkat, S. Kawata, Near-field Raman imaging of organic molecules by an apertureless metallic probe scanning optical microscope. *Journal of Chemical Physics* **117**, 1296 (2002).
3. M. Fleischmann, P. J. Hendra, A. McQuillan, Raman-Spectra of Pyridine Adsorbed at a Silver Electrode. *Chemical Physics Letters* **26**, 163 (1974).
4. D. L. Jeanmaire, R. P. Van Duyne, Surface Raman Spectroelectrochemistry .1. Heterocyclic, Aromatic, and Aliphatic-Amines Adsorbed on Anodized Silver Electrode. *Journal of Electroanalytical Chemistry* **84**, 1 (1977).
5. M. G. Albrecht, J. A. Creighton, Anomalous Intense Raman-Spectra of Pyridine at a Silver Electrode. *Journal of the American Chemical Society* **99**, 5215 (1977).
6. K. A. Willets, R. P. Van Duyne, Localized surface plasmon resonance spectroscopy and sensing. *Annual Review of Physical Chemistry* **58**, 267 (2007).
7. S. M. Nie, S. R. Emery, Probing single molecules and single nanoparticles by surface-enhanced Raman scattering. *Science* **275**, 1102 (1997).
8. K. Kneipp, Y. Wang, H. Kneipp, L. T. Perelman, I. Itzkan, R. Dasari, M. S. Feld, Single molecule detection using surface-enhanced Raman scattering (SERS). *Physical Review Letters* **78**, 1667 (1997).
9. E. Abbe, *Archiv Microskope Anatomie* **9**, 413, (1873).
10. R. M. Stockle, Y. D. Suh, V. Deckert, R. Zenobi, Nanoscale chemical analysis by tip-enhanced Raman spectroscopy. *Chemical Physics Letters* **318**, 131 (2000).
11. N. Hayazawa, Y. Inouye, Z. Sekkat, S. Kawata, Metallized tip amplification of near-field Raman scattering. *Optics Communications* **183**, 333 (2000).
12. M. S. Anderson, Locally enhanced Raman spectroscopy with an atomic force microscope. *Applied Physics Letters* **76**, 3130 (2000).
13. T. Ichimura *et al.*, Subnanometric Near-Field Raman Investigation in the Vicinity of a Metallic Nanostructure. *Physical Review Letters* **102**, (2009).
14. T.-a. Yano, P. Verma, Y. Saito, T. Ichimura, S. Kawata, Pressure-assisted tip-enhanced Raman imaging at a resolution of a few nanometres. *Nature Photonics* **3**, 473 (2009).
15. T. Deckert-Gaudig, E. Kaemmer, V. Deckert, Tracking of nanoscale structural variations on a single amyloid fibril with tip-enhanced Raman scattering. *Journal of Biophotonics* **5**, 215 (2012).
16. C. C. Neacsu, J. Dreyer, N. Behr, M. B. Raschke, Scanning-probe Raman spectroscopy with single-molecule sensitivity. *Physical Review B* **73**, (2006).

Chapter 1

17. W. Zhang, B. S. Yeo, T. Schmid, R. Zenobi, Single molecule tip-enhanced Raman spectroscopy with silver tips. *Journal of Physical Chemistry C* **111**, 1733 (2007).
18. J. Steidtner, B. Pettinger, Tip-enhanced Raman spectroscopy and microscopy on single dye molecules with 15 nm resolution. *Physical Review Letters* **100**, (2008).
19. E. Bailo, V. Deckert, Tip-enhanced Raman spectroscopy of single RNA strands: Towards a novel direct-sequencing method. *Angewandte Chemie-International Edition* **47**, 1658 (2008).
20. F. Sanger, S. Nicklen, A. R. Coulson, DNA Sequencing with Chain-Terminating Inhibitors. *Proc. Natl. Acad. Sci. U. S. A.* **74**, 5463 (1977).
21. M. Xu, D. Fujita, N. Hanagata, Perspectives and Challenges of Emerging Single-Molecule DNA Sequencing Technologies. *Small* **5**, 2638 (2009).
22. S. B. Baylin, DNA methylation and gene silencing in cancer. *Nature clinical practice. Oncology* **2 Suppl 1**, S4 (2005).
23. P. W. Laird, Principles and challenges of genome-wide DNA methylation analysis. *Nature Reviews Genetics* **11**, 191 (2010).
24. R. Mendelsohn, C. R. Flach, D. J. Moore, Determination of molecular conformation and permeation in skin via IR spectroscopy, microscopy, and imaging. *Biochimica Et Biophysica Acta-Biomembranes* **1758**, 923 (2006).
25. C. H. Xiao, D. J. Moore, M. E. Rerek, C. R. Flach, R. Mendelsohn, Feasibility of tracking phospholipid permeation into skin using infrared and raman microscopic imaging. *Journal of Investigative Dermatology* **124**, 622 (2005).
26. C. H. Xiao, D. J. Moore, C. R. Flach, R. Mendelsohn, Permeation of dimyristoylphosphatidylcholine into skin - Structural and spatial information from IR and Raman microscopic imaging. *Vibrational Spectroscopy* **38**, 151 (2005).

Chapter 2 From Raman via SERS to TERS

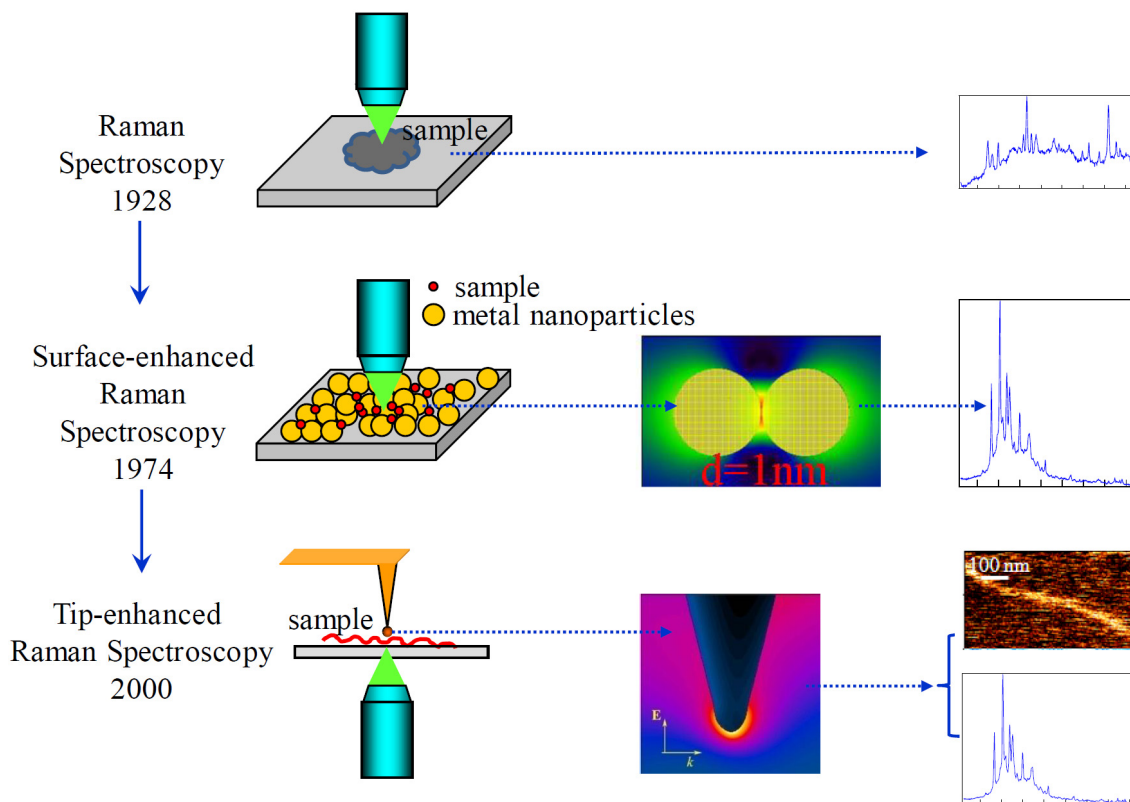


Fig. 2.1: The evolution from Raman via SERS to TERS, adapted from (1, 2).

Fig. 2.1 schematically illustrates the evolution from Raman spectroscopy via SERS to TERS. The Raman scattering effect was discovered by Indian physicist C. V. Raman in 1928 (3). It reveals molecular energy level based on the frequency shift between incident and scattered laser light and generally is an inherent weak process. The Raman signal is strikingly enhanced by introducing noble metals (eg. Au, Ag, and Cu) particles as substrates, commonly known as surface-enhanced Raman scattering (SERS) first observed by M. P. Fleischmann et al. in 1974 (4) and then explained by Van Duyne, Jeanmarie (5) and Albrecht, Creighton (6) in 1977. But SERS suffers from inhomogeneous enhancement of the substrates and the limit of lateral resolution to 200-250 nm (determined by the wavelength of the light applied and the numerical aperture of the lens). By exchanging the multiple particle substrate by one single particle attached to the apex of the scanning probe microscope tip, the obstacles can be avoided. The related technique is known as tip-enhanced Raman spectroscopy (TERS). The first experiment on TERS was realized by

Chapter 2

Deckert and co-workers (7) in 2000 and followed closely by Anderson (8) and Kawata and co-workers (9). More details of the evolution process, the related mechanisms, and the instrumentations are introduced in this chapter.

2.1 Raman spectroscopy

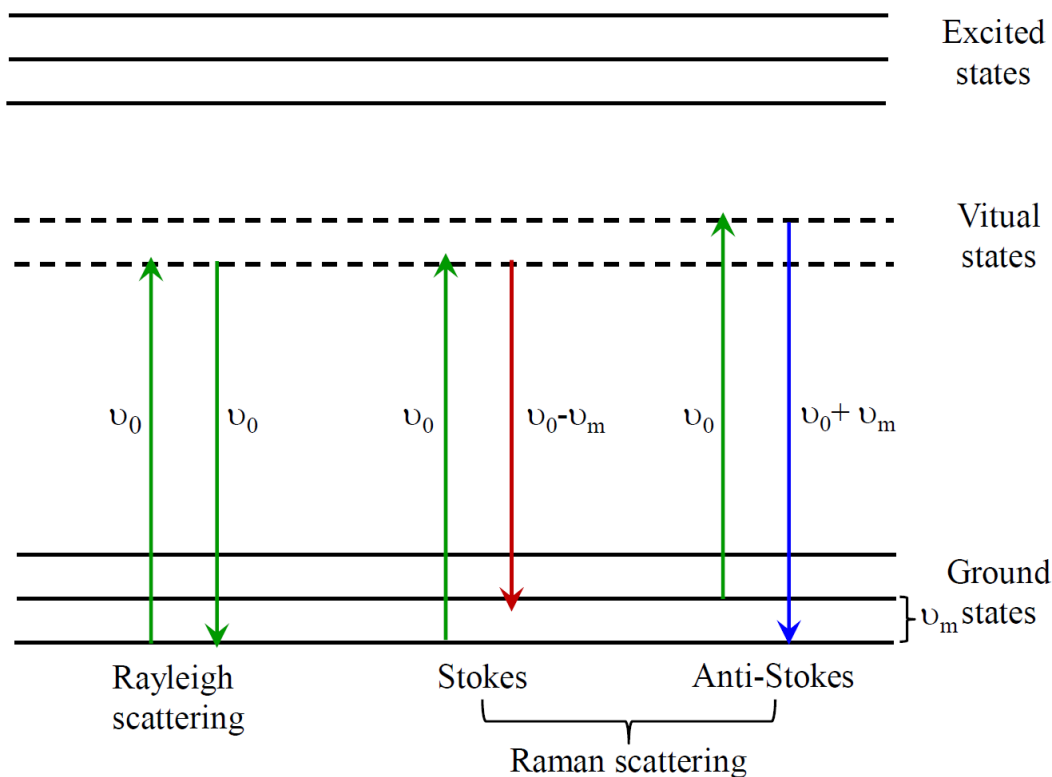


Fig. 2.2: Energy level diagram of the Rayleigh, Stokes and anti-Stokes scattering

When a sample is irradiated by an EM-wave, a part of this radiation is scattered in all directions. The scattered light consists of two types, see fig. 2.2: one is the elastic scattering, also known as Rayleigh scattering, which has the same frequency (ν_0) as the incident light; and the other is the inelastic scattering, is very weak and has a shift in frequency (ν_m) compared to the incident radiation, which was discovered by the Indian physicist C.V. Raman in 1928 and bears his name as Raman scattering (3). Most of these scattered photons have lower frequency ($\nu_0 - \nu_m$), while the rest show higher frequency ($\nu_0 + \nu_m$) than incident photons; the former is termed Stokes scattering, and the latter is anti-Stokes scattering.

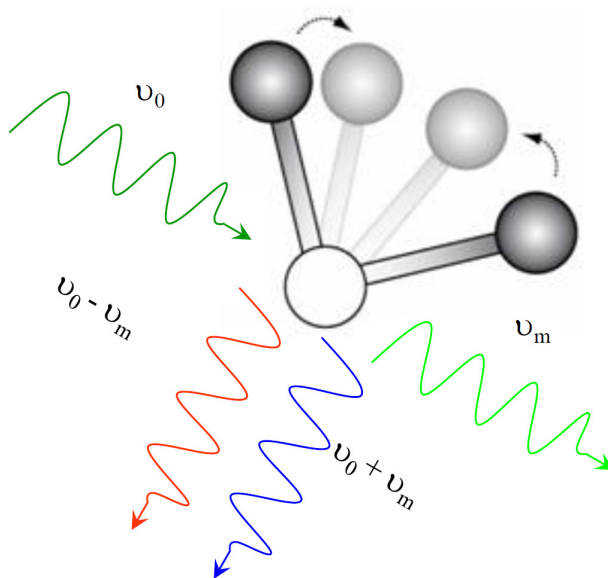


Fig. 2.3: Photons with frequency (ν_0) interact with a molecule and induce a molecular motion on the radiated molecule and immediately a photon with a different frequency ($\nu_0 \pm \nu_m$) is reemitted.

Raman spectroscopy is based on the inelastic scattering of light radiation. Inelastic scattering is characterized by a frequency shift of photons by interacting with the sample when subsequently reemitted (scattered) (fig. 2.2). The frequency of scattered photons is shifted to higher or lower frequencies in comparison to that of the incident radiation. The variations in frequency observed in this phenomenon are equivalent to variations in energy. Atoms and ions are bound to each other to form molecules and crystal systems and constantly perform vibrational and rotational motions. These oscillations are performed at exact frequencies as a function of the involved particle mass and the dynamic behaviors of the existent bonds, the force constants (fig. 2.3). Each vibrational and rotational mode has a corresponding energy level. Raman spectroscopy is specific for each chemical compound and is widely applied to identify and analyze chemical and condensed physical materials in research and industry currently.

A laser is commonly used as a radiation source in Raman spectroscopy. It can be considered as a polarized electromagnetic wave traveling in z-direction. It consists of the

Chapter 2

electric component (E, x-direction) and magnetic component (H, y-direction), which are perpendicular to each other, see fig. 2.4.

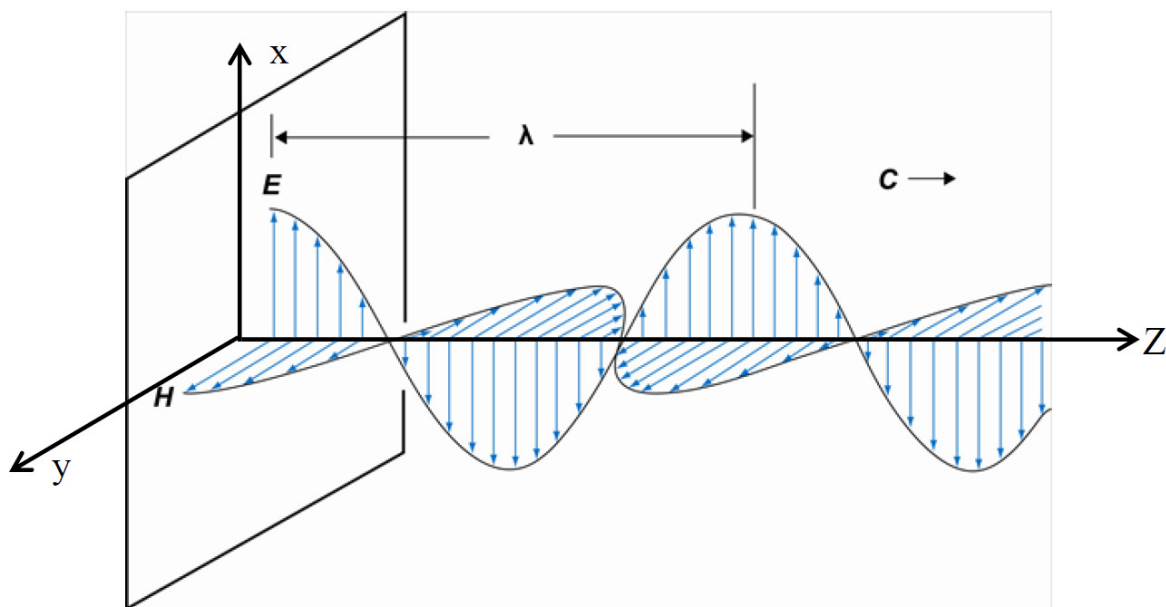


Fig. 2.4: Plane-polarized electromagnetic radiation, adapted from (10).

Raman scattering occurs when the laser beam (electric field) interacts with the electron cloud of the molecule. According to classical theory, Raman scattering can be explained as follows: the electric field strength (E) of the electromagnetic wave (laser beam) fluctuates with the time (t) as expressed by the following equation:

$$E = E_0 \cos(2\pi\nu_0 t) \quad (2-1)$$

Where (E_0) is the vibrational amplitude and (ν_0) is the frequency of the laser.

If a molecule is irradiated by this light, an electric dipole moment μ is induced:

$$\mu = \alpha E = \alpha E_0 \cos(2\pi\nu_0 t) \quad (2-2)$$

Where α is the polarizability of the molecule, which varies also with the time and is represented by:

Chapter 2

$$\alpha = \alpha_0 + \alpha_m \cos(2\pi\nu_m t) \quad (2-3)$$

Where α_0 is the polarizability of the equilibrium conformation of the molecule, α_m is the polarizability change with molecular vibration, and ν_m is the vibrational frequency of the molecule.

Combining equations (2-2) and (2-3) the dipole results as:

$$\mu = [\alpha_0 + \alpha_m \cos(2\pi\nu_m t)] \cdot E_0 \cos(2\pi\nu_0 t) \quad (2-4)$$

Equation (2-4) can be developed into three terms as:

$$\mu = \alpha_0 \cdot E_0 \cos(2\pi\nu_0 t) + 0.5\alpha_m \cdot E_0 \cos[2\pi(\nu_0 + \nu_m)t] + 0.5\alpha_m \cdot E_0 \cos[2\pi(\nu_0 - \nu_m)t] \quad (2-5)$$

These three terms refer to the fact that the oscillating dipole reemits the photons in three characteristic frequencies as has been mentioned: the first term is Rayleigh scattering, the second and third terms are anti-Stokes scattering and Stokes scattering. It is important to note that if the molecular vibration does not cause changes in polarizability ($\alpha_m=0$) and vibrational frequency ($\nu_m=0$), then no Raman scattering can be observed.

Each vibrational or rotational mode corresponds to a relative frequency shift, which is independent of the wavelength of the laser source. The collection of the different frequencies or Raman shifts undergone by a molecule is known as Raman spectrum and provides an individual fingerprint (composition of Raman shifts) characteristic for each molecule, which allows its identification and structural analysis.

2.2 Surface-enhanced Raman spectroscopy (SERS)

2.2.1 The discovery of SERS

As has been mentioned the Raman signal is generally weak, although this situation can be improved by using high-power laser to increase the amount of incident photons and/or increasing the accumulation time. The sensitivity is still very low and a huge number of

Chapter 2

molecules are needed, with the limit of detection generally higher than 10^{-3} M in solution. An effective strategy for enhancing the Raman signal is bringing the molecules close to a metallic surface, which enhances the Raman signal by several orders of magnitude. This effect is referred to as surface-enhanced Raman scattering (SERS). It was first observed in 1974 by Fleischmann, Hendra and McQuillan (4). They recorded unexpected strong Raman signals of pyridine adsorbed on a rough silver electrode. However, their interpretation was that the higher intensity results from a bigger quantity of molecules adsorbed on a rough surface. In 1977, Van Duyne, Jeanmarie (5) and Albrecht, Creighton (6) explained this effect independently from each other as a real electromagnetic (EM) enhancement of the signal by a factor of 10^6 which does not only result from the number of molecules probed.

2.2.2 The enhancement mechanism of SERS

The exact nature of the mechanism causing the enhancement is still unclear, but so far two mechanisms have been widely accepted in the community, namely the electromagnetic enhancement (11, 12) and the chemical enhancement (13). As has been mentioned, the Raman scattering intensity is proportional to the square of the transition dipole moment μ , which is given by:

$$\mu = \alpha E \quad (2-2)$$

Where α is the polarizability tensor of the molecule, and E is the electromagnetic field of the incident light. Therefore there are two possibilities to increase the signal, one is to alter the polarizability of the molecule and second is to simply increase the electromagnetic (EM) field strength. The first possibility relates to the chemical enhancement while the second relates to the electromagnetic enhancement theory which treats the amplification of the EM field.

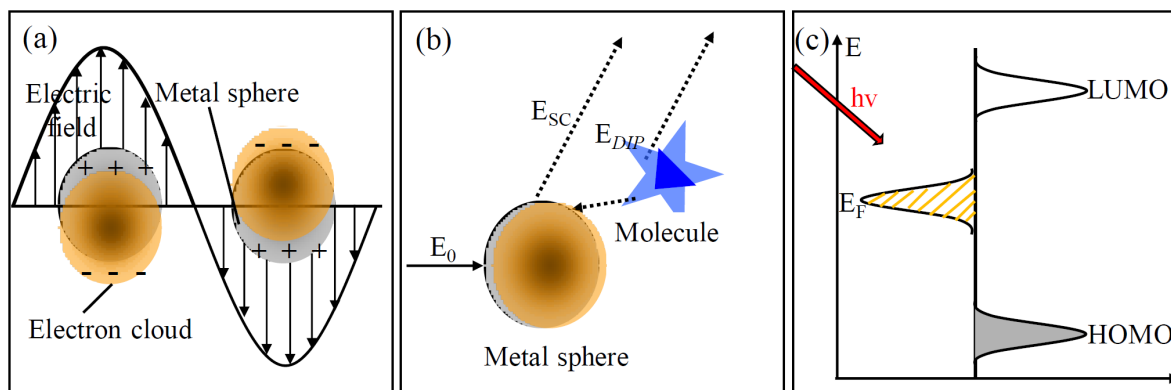


Fig. 2.5: Schematic diagrams illustrating localized surface plasmon (LSP) **(a)** and two main enhancement mechanisms for SERS signals of molecules, **(b)** electromagnetic enhancement and **(c)** chemical enhancement. E_0 : incoming electric field; E_{DIP} : dipolar field; E_{SC} : Raman-scattered field; E_F : Fermi level; HOMO: highest occupied molecular orbital; LUMO: lowest unoccupied molecular orbital. Adapted from (12-15).

Electromagnetic enhancement

The electromagnetic enhancement theory refers to the excitation of localized surface plasmons (LSP) (fig. 2.5 (a)), by which field enhancement occurs because of the resonance interaction between the electric fields and the surface plasmons in the metal, which is shown in fig. 2.5 (b). In essence, the incident light from a laser beam excites the localized surface plasmons, which are collective oscillations of conduction electrons. These plasmons then radiate a dipolar field (E_{DIP}). The coherent interaction of the incoming electric field (E_0) with the dipolar field (E_{DIP}) leads to a redistribution of the electric field intensities in areas around the metal clusters. Molecules nearby or adsorbed on the metal then “feel” a enhanced excitation intensity. In the same way as the incident laser field, the Raman-scattered field (E_{SC}) is enhanced as well. In SERS, the dominant enhancement of the Raman signal is due to EM, which is a long range effect, with an interaction length of the order of a few to a few tens of nanometers between the molecules and the substrates, with an enhancement factor of typical 10^6 up to 10^{10} (16).

Chemical enhancement

For the electromagnetic enhancement the molecule must be close to the metal particle, but does not need to be adsorbed on the surface. For the chemical enhancement of the Raman

Chapter 2

signal it is mandatory that the molecules are adsorbed on the surface and thus sometimes is also called short range effect relative to the EM. In the chemical enhancement, molecules are believed to build a charge transfer (CT) complex with the metal atoms at the surface, thereby changing the Raman polarizability tensor. The charge transfer is possible when the Fermi level (E_F) of the surface falls in between the highest occupied molecular orbital (HOMO) and the lowest unoccupied molecular orbital (LUMO) of the molecule, whereas both transfers from HOMO to E_F and E_F to LUMO are possible (fig. 2.5 (c)) (17). Considerable band shifts are associated with this effect and can be used to distinguish whether the metal particle is in direct contact with the sample. The estimated typical enhancement factor is 10^2 - 10^3 (18, 19). The EM and the chemical mechanism act in conjunction and it is difficult or even nearly impossible to discern the different contributions experimentally.

SERS provides wealth information on structural and dynamical of samples due to its huge enhancement effect. Furthermore, the combination of SERS with optical microscope enables the spectral features spatially defined. Therefore, SERS has been widely applied in surface science, material science and biomedicine (20). The main obstacle associated with SERS is the inhomogeneity of the field enhancement across the sample. SERS effect is shown for different substrate types including metal roughened electrodes, colloids, metal films, and periodic nanostructures (21). The different shapes, sizes and roughness of single particles and clusters result in strong variations of the field enhancement and consequently the Raman signal. Furthermore, these physical parameters also depend critically on the substrate preparation. For periodic nanostructures, the field enhancement is more constant but the fabrication is complex and costly. Therefore, a quantitative analysis of interfaces using SERS is difficult.

It is well known that the large field enhancement at metal particles occurs in regions of high curvature and maximum enhancement occurs for elongated particles with dimensions of about 10-100 nm. While clusters are considered to yield a better overall enhancement, also a single isolated metal nanoparticle can enhance the field considerably (22-24).

Chapter 2

2.3 Tip-enhanced Raman spectroscopy (TERS)

2.3.1 The theoretical proposal and experimental realization of TERS

Scanning probe microscopy (SPM) (25, 26) has enabled researchers to image surfaces at the nanometer scale. SPM is a general term, used to describe a growing number of techniques that mechanically move the probe in a raster scan over the specimen, line by line, and recording the probe-surface interaction as a function of position displayed in image form. SPM offers superb spatial resolution but lacks chemical specificity.

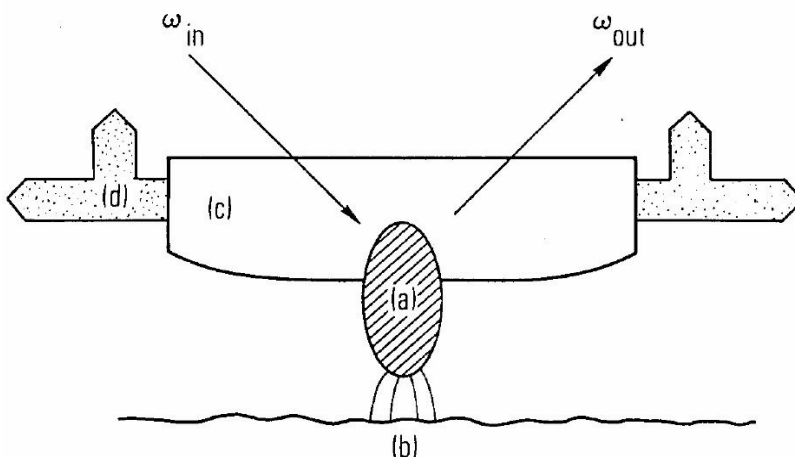


Fig. 2.6: Single metal nanoparticle working as optical probe particle designed by Wessel (24).

The concept of a single-particle surface-enhanced microscope using SPM tip emerged in 1985. Wessel (24) theoretically proposed the combination of the then newly invented STM technique with a submicrometer-sized metal particle antenna scanning over and investigating the surface. Fig. 2.6 illustrates the idea proposed by Wessel for the construction of a single-particle surface-enhanced microscope. Wessel's idea for the first time replaced the rough metal SERS substrates by a sharp metal tip that would act as an exclusively active site with constant field enhancement, which overcame the limits of SERS (inhomogeneity of substrates and diffraction limit).

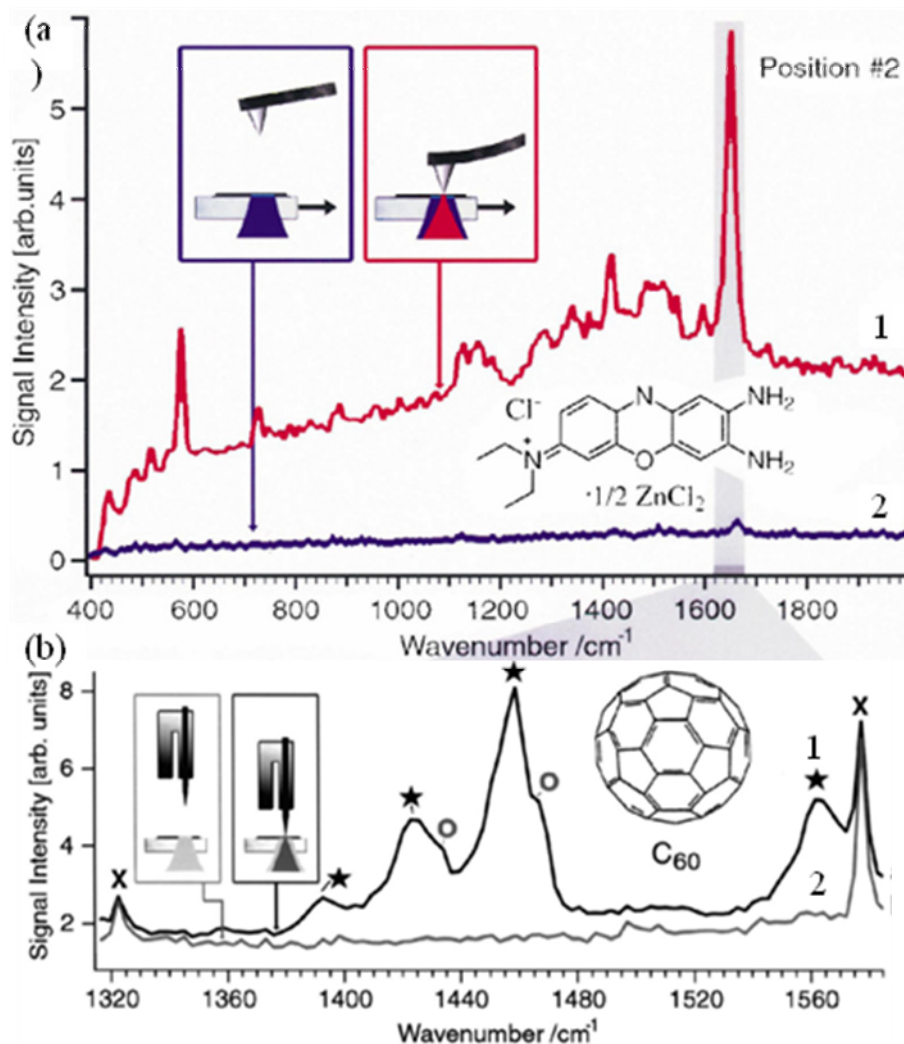


Fig. 2.7: TERS spectra of brilliant cresyl blue (BCB) (a), and C₆₀ (b). 1. The tip contacted with the sample; 2. Tip retracted. From ref. (7).

The experimental realization of Wessel's idea is known as TERS. It took 15 years to actually prove this concept experimentally. The first such proof was done by Deckert and co-workers (7). In their experiment they showed that the Raman spectra of brilliant cresyl blue (BCB) can be enhanced by bringing a metal coated atomic force microscope (AFM) tip into contact with the sample (fig. 2.7 (a)). A similar phenomenon was observed with C₆₀ when an electrochemically etched gold tip was used (fig. 2.7 (b)). In the same year Kawata and coworker (9) and Anderson (8) also developed a TERS setup independently.

Chapter 2

2.3.2 The enhancement mechanism of TERS

The large enhancement of Raman scattering from single metal probe used in TERS can be discussed on the same basis as the SERS effect, namely the electromagnetic effect and the chemical effect. One of the most important features of TERS is the ability to highly confine the electromagnetic field at the apex of a sharp metal or metalized tip. This is due to an electrostatic lightning rod effect as a result of the shape of the particle at the tip apex and results in the high spatial resolution of the technique (27).

2.3.3 TERS instrumentation (27-30)

2.3.3.1 Different SPM feedback systems in TERS

TERS is the combination of SPM and Raman. Here the SPM can be AFM, fig. 2.8 (a)), STM, fig. 2.8 (b)), and shear force microscope (SFM, fig. 2.8 (c)).

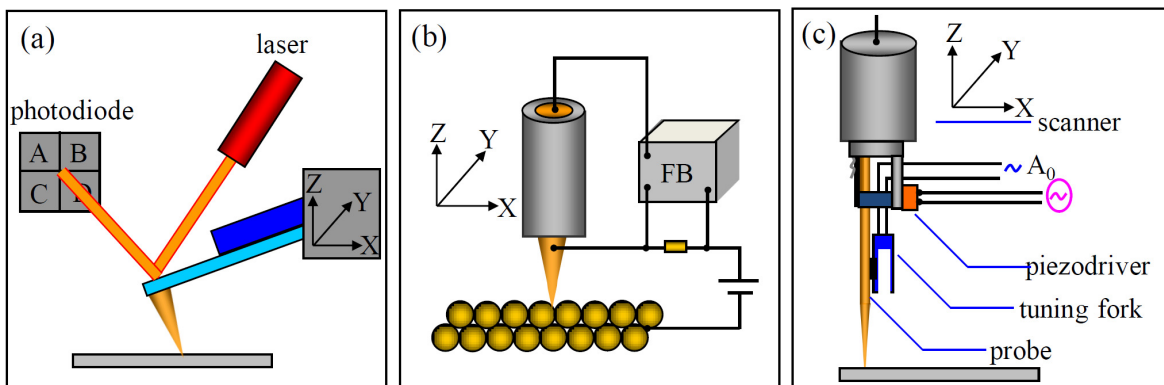


Fig. 2.8: Schematic illustration of three different SPM instruments: **(a)** Atomic force microscopy (AFM); **(b)** Scanning tunneling microscope (STM); **(c)** shear force microscopy (SFM).

AFM: AFM measures the interaction force between the tip and the surface. When the tip is mechanically brought into proximity of a sample surface, forces between the tip and the sample lead to a deflection of the cantilever. The deflection is measured using a laser spot reflected from the top surface of the cantilever into an array of photodiodes showing the topography information of the measured surface (fig. 2.8 (a)). In AFM, contact mode and tapping mode are usually used for imaging. In contact mode, as the name already suggests, the surface is tracked by the tip in close contact. The tip can either be held at a constant distance or at a constant force relative to the sample (fig. 2.9 (a)). The advantages of contact

Chapter 2

mode are: fast scanning, good for rough samples, and can be used in friction analysis; the disadvantage is at time forces can damage/deform soft samples. In tapping mode, the imaging is similar to contact. However, in this mode the cantilever is oscillated at its resonant frequency. The probe lightly “taps” on the sample surface during scanning, contacting the surface at the bottom of its swing. By maintaining a constant oscillation amplitude, a constant tip-sample interaction is maintained and an image of the surface is obtained (fig. 2.9 (b)). The advantages of tapping mode are: allows high resolution on samples that are easily damaged and/or loosely held to a surface, good for biological samples; the disadvantages are: more challenging to image in liquids, slower scan speeds are needed. The main advantages of AFM feedback are: it has no sample requirements and can work on virtually any surface (conductive and insulated) with a roughness of up to several microns and a scan area up to tens square-microns, which make AFM powerful for observing biological samples in physiological states.

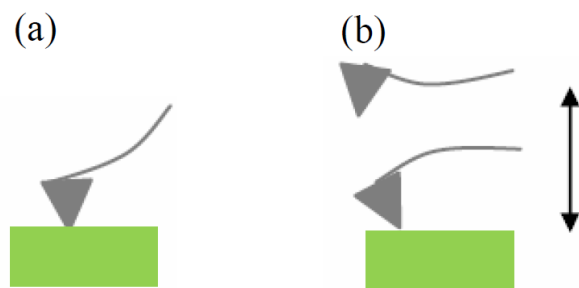


Fig. 2.9: Two mainly used imaging modes in AFM **(a)** Contact mode and **(b)** Tapping mode.

STM: The fundamental principle of STM is that a conducting tip is kept in tunneling distance ($< 1\text{ nm}$) to the conductive surface, a bias (voltage difference) applied between the two can allow electrons to tunnel between them. The resulting tunneling current displays the examined surface information in image form (fig. 2.8 (b)). The main advantages of STM feedback are: the high spatial resolution and high control precision because of the tunneling current effect. The disadvantages are the limitations to the conductive tips and samples, the limitation to the sample height to approximately 1 nm , due to the sensitivity of the tunnel current.

Chapter 2

SFM: In SFM, a nanotip is stuck to a high frequency tuning fork to detect the proximity of the surface by damping of the free oscillation (fig. 2.8 (c)), similar to tapping mode AFM. The major difference is the oscillation direction of the tuning fork laterally to the sample surface, which keeps the sample-tip distance more or less constant. The main advantage is: convenient to be combined with inverted and upright microscope respectively. The drawback is that it does not fit the standard AFM equipment.

2.3.3.2 Different illumination/collection geometries in TERS

Depending on the properties of different samples and the collection efficiency of the Raman signal, there are three different types of illumination/collection geometries in TERS: bottom, side and parabolic mirror, which are shown in fig. 2.10 (a), (b), and (c) respectively

Bottom illumination/ collection: in this configuration (fig. 2.10 (a)), an SPM tip is placed on top of an inverted optical microscope and illuminated by the excitation laser from below using an immersion objective with a high numerical aperture (NA, 1.2-1.6). The Raman signal is collected through the same objective. This configuration ensures a high efficiency and avoids a large contribution of unenhanced signal compared to the reflection mode. The major shortcoming for this configuration is the restriction to transparent samples.

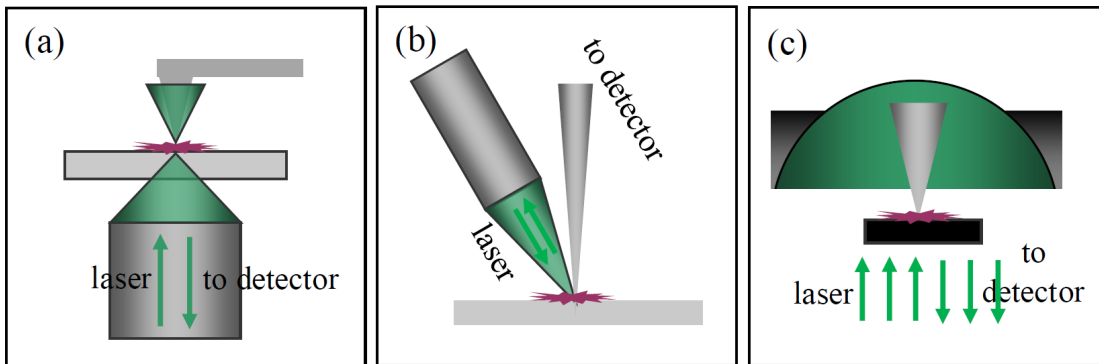


Fig. 2.10: Different illumination geometries: (a) Backscattering illumination; (b) Side illumination; (c) Illumination with a parabolic mirror.

Side illumination/ collection: in this configuration (fig. 2.10 (b)), an SPM tip is illuminated by the excitation laser from side through a long working distance objective with lower NA (< 0.6). The Raman signal can be collected through the same objective from the

Chapter 2

side. The major advantage of this configuration is that the sample can be opaque. A disadvantage is the low contrast between the near-field and far-field signals because of the unfavorable ratio between the illuminated and enhanced areas.

Illumination/ collection based on parabolic mirror: The high NA objective used in TERS is limited to bottom illumination/collection configuration. To overcome this problem, the objective with high NA is replaced by a parabolic mirror allows the collection of scattered Raman signal from all directions (fig. 2.10 (c)). The parabolic mirror based TERS setup works in reflection mode so it is capable of detecting both transparent and opaque samples. Very good enhancements are achieved with radially polarized light. The main challenge is the highly sensitive alignment.

2.3.3.3 The fabrication of TERS tips

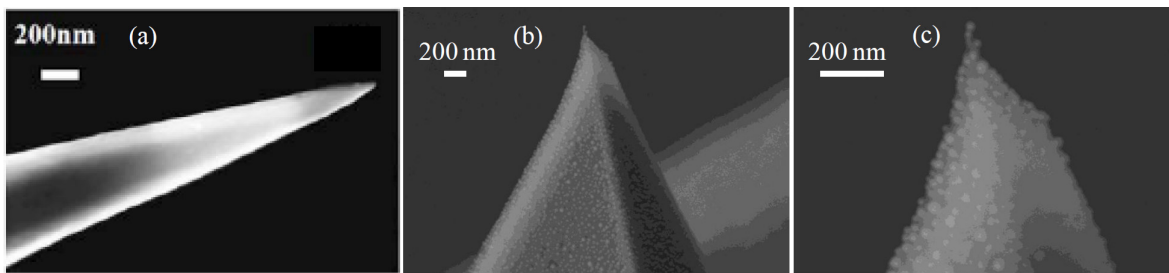


Fig. 2.11: SEM images of TERS tips fabricated by different methods. **(a)** Electrochemically etched Au tip (31); **(b), (c)** Silver-coated AFM tip with different amplifications, which was fabricated in IPHT, Jena and used in the present TERS measurements.

The tip fabrication in TERS is crucial as tip works as a SPM probe and more important as an enhancement resource as well. The material and shape of TERS tip determines field enhancement and the lateral resolution occurring at the apex of the tips (32-34). Mainly silver and gold tips are used because of their superior plasmon resonances in the visible regime, which can be metal-coated standard AFM tips by evaporation or can be pure metal tips made by electrochemical etching of metal wires. For more details on TERS tip fabrication see ref. (27). Fig. 2.11 (a) shows a electrochemical etched Au tip (31), and (b),

Chapter 2

(c) show a silver-coated AFM tip with different amplifications fabricated in IPHT, Jena and used in the present TERS measurements.

Compared to silver tips, gold tips are more frequently used because they are easy to manufacture and are more stable. Silver tips in general have better optical properties with respect to the surface enhancement properties than gold tips and were used here. To date, the STM and SFM based TERS setups both use metallic Au tips, while the AFM based TERS setups usually use silver coated tips. So far all the produced TERS tips are relatively fragile, where the tip apex is either broadened or the coating is peeled off after several hours of scanning. Furthermore, the silver coated tips are easily oxidized in air therefore are stored under inert gas.

2.3.3.4 The choice for the optimal TERS configuration

The choice of the optimal TERS configuration critically depends on the specific requirements of the samples involved. The feedback system required depends either on the conductivity properties or the thickness of the sample. The appropriate illumination mode configuration for a TERS experiment depends on the transparency of the sample. Finally, the choice of the proper tip depends on the spectral absorption characteristics of the sample and therefore which excitation wavelength is desirable.

2.3.4 The high spectral sensitivity in TERS - single molecule (SM)-TERS

First reports of SM-TERS came from the group of Raschke in 2006 (35), who used malachite green sample adsorbed on vacuum evaporation flat Au films. The spectra from Raschke showed great fluctuations in signal intensities and band positions, fig. 2.12. These observations were attributed to a single molecule moving within the enhancement zone, to electric field gradient effects, and to different Raman selection rules. Later on, Pettinger presented fingerprint-quality TERS spectra of green isothiocyanate adsorbed on Au (111) surface exhibiting no spectral fluctuations (36). The signals were ascribed to scattering from < 5 dye molecules which is confirmed by STM images. No variation in band positions or relative band intensities was observed at the single- or few-molecule detection level when employing TERS spectroscopy was attributed to well-defined adsorption sites at

Chapter 2

atomically smooth Au (111) surfaces. In 2007, Zenobi & coworkers presented the evidence for the SM-TERS of brilliant cresyl blue adsorbed on vapor coated flat Au film (37). Spectroscopic fluctuations, including intensity fluctuations, small frequency shifts, and line shape changes were also observed, although the fluctuations were much smaller in magnitude than those reported by Raschke et al..

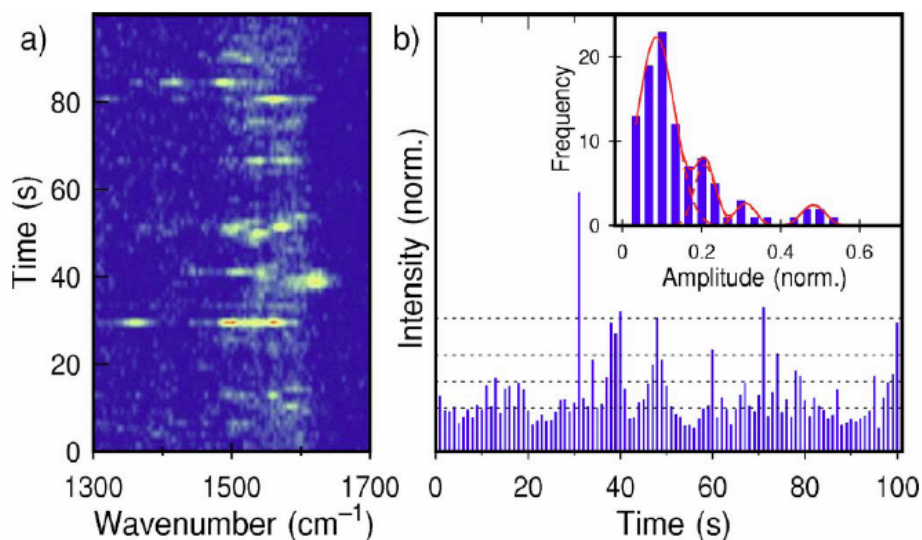


Fig. 2.12: Time series of tip-scattered Raman spectra for a submonolayer MG surface coverage **(a)** The spectral diffusion observed is characteristic for observing single MG molecules; **(b)** Temporal variation of the intensities of the integrated 1480–1630 cm^{-1} Raman band with 170–230 $\text{counts mol}^{-1} \text{s}^{-1}$ (dashed line increment). From the corresponding histogram inset a discretization of Raman intensities can be seen (35).

In SERS and TERS, evidence cited to SM interpretation are: (a) low analyte concentrations were used to ensure that there is less than one molecule on average in the scattering volume, and (b) spectral fluctuations of the Raman signals were observed, analogous to the blinking behavior reported in single molecule fluorescence spectroscopy. In Raschke and Zenobi's SM experiments, the molecules were adsorbed on vapor coated flat Au film. The non well-defined Au film surface cannot ensure the low concentration and homogeneous distribution of the molecules. Concerning on the fluctuation phenomenon, there can be several causes (37-39): (a) a molecule diffusing/re-orienting under the tip, i.e., single molecule behavior; (b) physical (e.g., morphology) and chemical (e.g., oxidation) changes of the TERS tip during the experiment because of laser irradiation; (c) tip moving by itself due to instability

Chapter 2

of the SPM system or due to laser heating effects, and (d) carbon contamination diffusing in the enhancement zone. Only (a) is a SM effect. Therefore, the evidences presented for the SM behavior characterization are still argumentative.

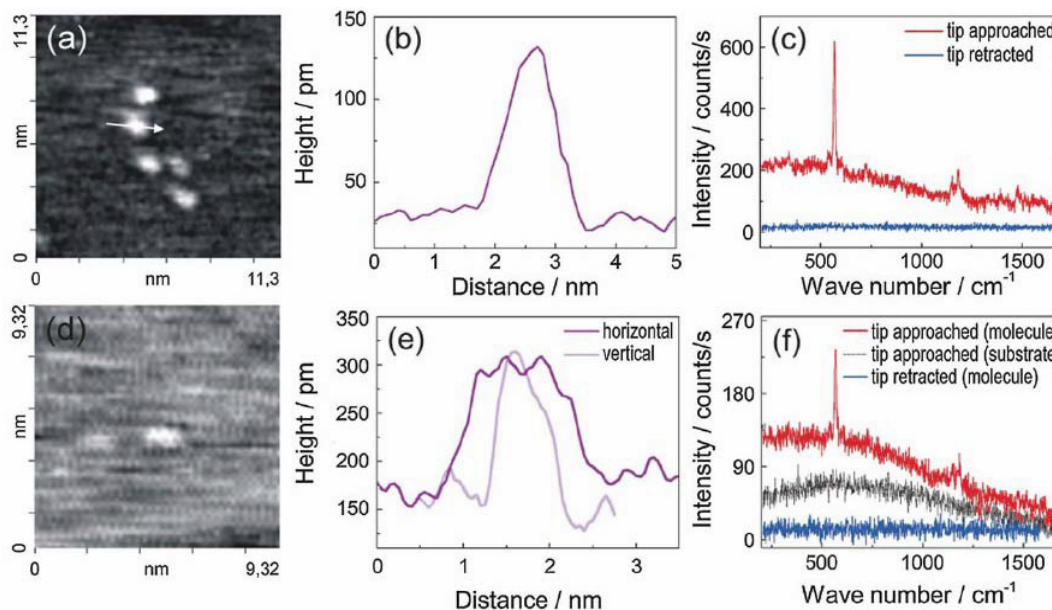


Fig. 2.13: STM images of five (a) and a single BCB molecule (d) adsorbed on Au (111), the corresponding height cross sections (b), (e) and the UHV-RR and UHV-TERR spectra (c), (f) (40).

In 2008, Steidtner and Pettinger solidly demonstrated the SM detection capability of TERS (40). They imaged a BCB molecule chemisorbed on an Au (111) surface with STM and then collected its TERS spectrum in ultra high vacuum (UHV). The performance of the experiment in UHV maintained the stability of the analyte from photo-oxidation processes and avoided the carbon contaminations in the air. The TERS spectra were stable over a reasonably long period of time, and the single BCB molecule could be re-imaged after its TERS spectrum was collected, fig. 2.13.

Also in 2008, Bailo and Deckert reported TERS spectra of single RNA strands with single-base sensitivity (41). In their report, the signal to noise ratio (SNR) of approximately 200 was obtained from 30–60 nucleobases underneath the TERS tip. Assuming a homogeneous signal enhancement, every single nucleobase then contributed with a SNR of 3–7 to the spectrum, which meant that single-base sensitivity had been achieved.

Chapter 2

2.3.5 The high lateral resolution in TERS

The basic explanation of the high-resolution capabilities of TERS is based on the highly confined evanescent field at the apex of a tip (28). The resolution of TERS is mainly determined by the radius of the tip (fig 2.14 (b)) and also directly affected by the substrate material and the tip-substrate distance separation. In general, increasing the radius of the tip, increasing the tip-substrate distance, or changing the metallic substrate into a dielectric substrate will lower the spatial resolution (2). According to the reported theoretical and experimental results (2, 40, 42), normally with a tip radius of ~ 20 nm, tip-substrate distance of 1 nm, metallic or dielectric substrate, the spatial resolution of about 8 nm is acceptable. However, Kawata's group reported a lateral resolution of 3-4 nm (43, 44), which is realized by selectively applying an external pressure on a nanometric volume of the sample through the apex of a sharp nanotip, see fig. 2.14 (c). By applying the pressure, the tip contacted or even compressed the sample, therefore, the short-range chemical and mechanical interactions between the tip and sample became significant and resulted in super high lateral resolution (3-4 nm). They even predicted a molecular resolution by this technique (43) (45). Deckert and coworkers also reported a super high lateral resolution of < 2 nm, which is explained by a very small effective tip size, or an additional field confinement due to gap mode, or a direct interaction between tip and sample, or even a combination of all these effects (46).

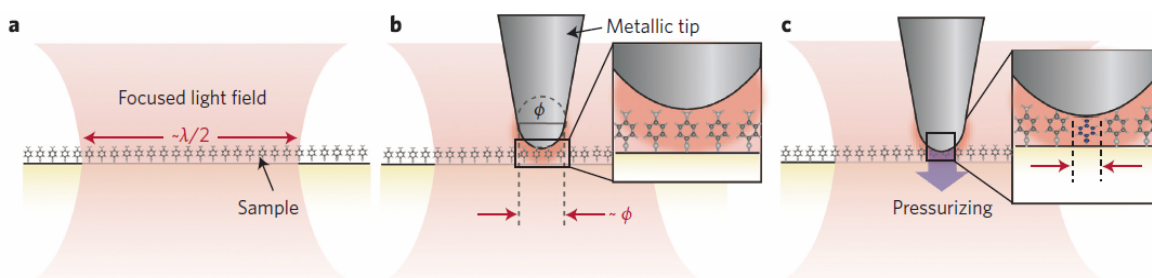


Fig. 2.14: Extremely high spatial resolution in optical microscopy is achieved by sensing the localized pressure applied by a nanosized tip. **(a)** Image resolution in optical microscopy is determined by the diffraction-limited focal spot, which is approximately a half of the probing wavelength; **(b)** Spatial resolution in normal TERS is determined by the localized light field, comparable to the diameter f of the tip apex; **(c)** When a sample is pressurized by the tip apex only a few sample molecules are mechanically deformed. By

Chapter 2

sensing the optical response of these molecules, a spatial resolution up to the molecular level can be achieved, adapted from (43).

2.3.6 The spectral fluctuation in TERS

The basic explanation of the fact that the SERS spectra often show shifts in band position, band intensities and sometimes even new bands compared to the normal Raman spectra of the same molecule is based on so called surface selection rules and chemical enhancement (12, 13). In TERS, the spectral fluctuation (band position and band intensity) is more significant compared to SERS and has been observed by many TERS groups (Kawata (47-49), Deckert (41), Raschke (35), and Zenobi (37)). Due to the high resolution of TERS, only a few or even sometimes a single molecule contributes to the TERS signal, therefore, the spectral fluctuation is attributed to not only the surface selection rule and chemical enhancement, but also to the “nano-scale effect” (41), the changes of molecular orientation under the tip and even the different atoms sites in molecule interacting with the different metal atoms on the tip (47-49). A good example is a serial of TERS measurements performed on nanocrystal adenine. The obtained near-field spectra showed fluctuations of spectral shapes, including fluctuations of peak frequencies and peak intensities and extraordinary enhancements of several peaks, which is different from the normal Raman and conventional SERS spectra. However, these bands can be identified to the normal modes of adenine using density-functional theory (DFT) vibrational calculations of adenine complexes involving a silver atom. In adenine there are four nitrogen atoms, N1, N3, N7, and N10 which can bind to the silver nanoparticles forming four Ag-N isomers. Depending on which isomers were formed, specific vibrational modes and spectral shifts were observed experimentally. This phenomenon was attributed to the changes of molecular orientation under the silver-coated tip as well. The obtained results showed a potential to achieve atomic site-selective detection sensitivity of TERS and demonstrated the importance of sample-tip interaction at molecular level in the interpretation of TERS spectra (47-49).

2.4 References

1. R. Liu, J. F. Liu, X. X. Zhou, G. B., Jiang, Applications of Raman-based techniques to on site and in-vivo analysis. *Trends in Analytical Chemistry* **30**, 1462 (2011).
2. Z. L. Yang, J. Aizpurua, H. X. Xu, Electromagnetic field enhancement in TERS configurations. *Journal of Raman Spectroscopy* **40**, 1343 (2009).
3. C. V. Raman, K. S. Krishnan, A new type of Secondary Radiation. *Nature* **121**, 501 (1928).
4. M. Fleischmann, P. J. Hendra, A. J., McQuillan, Raman-Spectra of Pyridine Adsorbed at a Silver Electrode. *Chemical Physics Letters* **26**, 163 (1974).
5. D. L. Jeanmaire, R. P. Vanduyne, Surface Raman Spectroelectrochemistry .1. Heterocyclic, Aromatic, and Aliphatic-Amines Adsorbed on Anodized Silver Electrode. *Journal of Electroanalytical Chemistry* **84**, 1 (1977).
6. M. G. Albrecht, J. A. Creighton, Anomalous Intense Raman-Spectra of Pyridine at a Silver Electrode. *Journal of the American Chemical Society* **99**, 5215 (1977).
7. R. M. Stöckle, Y. D. Suh, V. Deckert, R. Zenobi, Nanoscale chemical analysis by tip-enhanced Raman spectroscopy. *Chemical Physics Letters* **318**, 131 (2000).
8. M. S. Anderson, Locally enhanced Raman spectroscopy with an atomic force microscope. *Applied Physics Letters* **76**, 3130 (2000).
9. N. Hayazawa, Y. Inouye, Z. Sekkat, S. Kawata, Metallized tip amplification of near-field Raman scattering. *Optics Communications* **183**, 333 (2000).
10. A. Campion, P. Kambhampati, Surface-enhanced Raman scattering. *Chemical Society Reviews* **27**, 241 (1998).
11. M. Moskovits, Surface-Enhanced Spectroscopy. *Reviews of Modern Physics* **57**, 783 (1985).
12. M. Kerker, D. S. Wang, H. Chew, Surface Enhanced Raman-Scattering (SERS) by Molecules Adsorbed at Spherical-Particles. *Applied Optics* **19**, 4159 (1980).
13. A. Otto, I. Mrozek, H. Grabhorn, W. Akemann, Surface-Enhanced Raman-Scattering. *Journal of Physics-Condensed Matter* **4**, 1143 (1992).
14. M. Moskovits, J. S. Suh, Surface Selection-Rules for Surface-Enhanced Raman-Spectroscopy - Calculations and Application to the Surface-Enhanced Raman-Spectrum of Phthalazine on Silver. *Journal of Physical Chemistry* **88**, 5526 (1984).
15. K. A. Willets, R. P. Van Duyne, in *Annual Review of Physical Chemistry* **58**, 267 (2007).
16. G. C. Schatz, R. P. Van Duyne, Electromagnetic Mechanism of Surface-Enhanced Spectroscopy. *Handbook of Vibrational Spectroscopy*, J. M. Chalmers, and P. R. Griffiths, Ed., New York, Wiley, 759 (2002).
17. Z. Q. Tian, B. Ren, D. Y. Wu, Surface-enhanced Raman scattering: From noble to transition metals and from rough surfaces to ordered nanostructures. *Journal of Physical Chemistry B* **106**, 9463 (2002).
18. J. F. Arenas, I. Lopez-Tocon, S. P. Castro, M. R. Lopez-Ramirez, J. C. Otero, Resonant charge transfer on the nanoscale: studying doublet states of adsorbates by surface-enhanced Raman scattering. *Journal of Raman Spectroscopy* **36**, 515 (2005).
19. A. Otto, The 'chemical' (electronic) contribution to surface-enhanced Raman scattering. *Journal of Raman Spectroscopy* **36**, 497 (2005).
20. D. Cialla *et al.*, Surface-enhanced Raman spectroscopy (SERS): progress and trends. *Analytical and Bioanalytical Chemistry* **403**, 27 (2012).
21. X.-M. Lin, Y. Cui, Y.-H. Xu, B. Ren, Z.-Q. Tian, Surface-enhanced Raman spectroscopy: substrate-related issues. *Analytical and Bioanalytical Chemistry* **394**, 1729 (2009).
22. A. Wokaun, J. P. Gordon, P. F. Liao, Radiation damping in surface-enhanced Raman scattering, *Physical Review Letters* **48**, 957 (1982).
23. P. W. Barker, R. K. Chang, H. Massoudi, Surface-Enhanced Electric Intensities on Large Silver Spheroids, *Physical Review Letters* **50**, 997 (1983).

Chapter 2

24. J. Wessel, Surface-enhanced optical microscopy. *Journal of the Optical Society of America* **2**, 1538 (1985).
25. G. Binnig, H. Rohrer, C. Gerber, E. Weibel, Surface Studies by Scanning Tunneling Microscopy. *Physical Review Letters* **49**, 57 (1982).
26. G. Binnig, C. F. Quate, C. Gerber, Atomic Force Microscope. *Physical Review Letters* **56**, 930 (1986).
27. E. Bailoa, V. Deckert, Tip-enhanced Raman scattering. *Chemical Society Reviews* **37**, 921 (2008).
28. L. Novotny, S. J. Stranick, Near-field Optical Microscopy and Spectroscopy with Pointed Probes. *Annual Review of Physical Chemistry* **57**, 303 (2006).
29. A. Hartschuh, Tip-Enhanced Near-Field Optical Microscopy. *Angewandte Chemie-International Edition* **47**, 8178 (2008).
30. B. Pettinger, P. Schambach, C. J. Villagomez, N. Scott, Tip-Enhanced Raman Spectroscopy: Near-Fields Acting on a Few Molecules. *Annual Review of Physical Chemistry* **63**, 379 (2012).
31. X. Wang *et al.*, Tip-enhanced Raman spectroscopy for investigating adsorbed species on a single-crystal surface using electrochemically prepared Au tips. *Applied Physics Letters* **91**, (2007).
32. Y. C. Martin, H. F. Hamann, H. K. Wickramasinghe, Strength of the electric field in apertureless near-field optical microscopy. *Journal of Applied Physics* **89**, 5774 (2001).
33. J. T. Krug, E. J. Sanchez, X. S. Xie, Design of near-field optical probes with optimal field enhancement by finite difference time domain electromagnetic simulation. *Journal of Chemical Physics* **116**, 10895 (2002).
34. L. Novotny, Effective wavelength scaling for optical antennas. *Physical Review Letters* **98**, (2007).
35. C. C. Neacsu, J. Dreyer, N. Behr, M. B. Raschke, Scanning-probe Raman spectroscopy with single-molecule sensitivity. *Physical Review B* **73**, (2006).
36. K. F. Domke, D. Zhang, B. Pettinger, Toward Raman fingerprints of single dye molecules at atomically smooth Au(111). *Journal of the American Chemical Society* **128**, 14721 (2006).
37. W. Zhang, B. S. Yeo, T. Schmid, R. Zenobi, Single molecule tip-enhanced Raman spectroscopy with silver tips. *Journal of Physical Chemistry C* **111**, 1733 (2007).
38. K. F. Domke, D. Zhang, B. Pettinger, Enhanced Raman spectroscopy: Single molecules or carbon? *Journal of Physical Chemistry C* **111**, 8611 (2007).
39. B.-S. Yeo, J. Stadler, T. Schmid, R. Zenobi, W. Zhang, Tip-enhanced Raman Spectroscopy - Its status, challenges and future directions. *Chemical Physics Letters* **472**, 1 (2009).
40. J. Steidtner, B. Pettinger, Tip-enhanced Raman spectroscopy and microscopy on single dye molecules with 15 nm resolution. *Physical Review Letters* **100**, (2008).
41. E. Bailo, V. Deckert, Tip-enhanced Raman spectroscopy of single RNA strands: Towards a novel direct-sequencing method. *Angewandte Chemie-International Edition* **47**, 1658 (2008).
42. N. Anderson, A. Hartschuh, S. Cronin, L. Novotny, Nanoscale vibrational analysis of single-walled carbon nanotubes. *Journal of the American Chemical Society* **127**, 2533 (2005).
43. T.-a. Yano, P. Verma, Y. Saito, T. Ichimura, S. Kawata, Pressure-assisted tip-enhanced Raman imaging at a resolution of a few nanometres. *Nature Photonics* **3**, 473 (2009).
44. T. Ichimura *et al.*, Subnanometric Near-Field Raman Investigation in the Vicinity of a Metallic Nanostructure. *Physical Review Letters* **102**, (2009).
45. S. Kawata, Y. Inouye, P. Verma, Plasmonics for near-field nano-imaging and superlensing. *Nature Photonics* **3**, 388 (2009).

Chapter 2

46. T. Deckert-Gaudig, E. Kaemmer, V. Deckert, Tracking of nanoscale structural variations on a single amyloid fibril with tip-enhanced Raman scattering. *Journal of Biophotonics* **5**, 215 (2012).
47. H. Watanabe, Y. Ishida, N. Hayazawa, Y. Inouye, S. Kawata, Tip-enhanced near-field Raman analysis of tip-pressurized adenine molecule. *Physical Review B* **69**, (2004).
48. T. Ichimura *et al.*, Temporal fluctuation of tip-enhanced Raman spectra of adenine molecules. *Journal of Physical Chemistry C* **111**, 9460 (2007).
49. N. Hayazawa, H. Watanabe, Y. Saito, S. Kawata, Towards atomic site-selective sensitivity in tip-enhanced Raman spectroscopy. *The Journal of Chemical Physics* **125**, 244706 (2006).

Chapter 3 Experimental part

3.1 TERS setup in the present work

Two TERS setups, setup 1 and setup 2 were used in the present work. All the measurements on RNA, DNA and methylated DNA were performed on setup 2 and the measurements on invasomes and skin were performed on setup1.

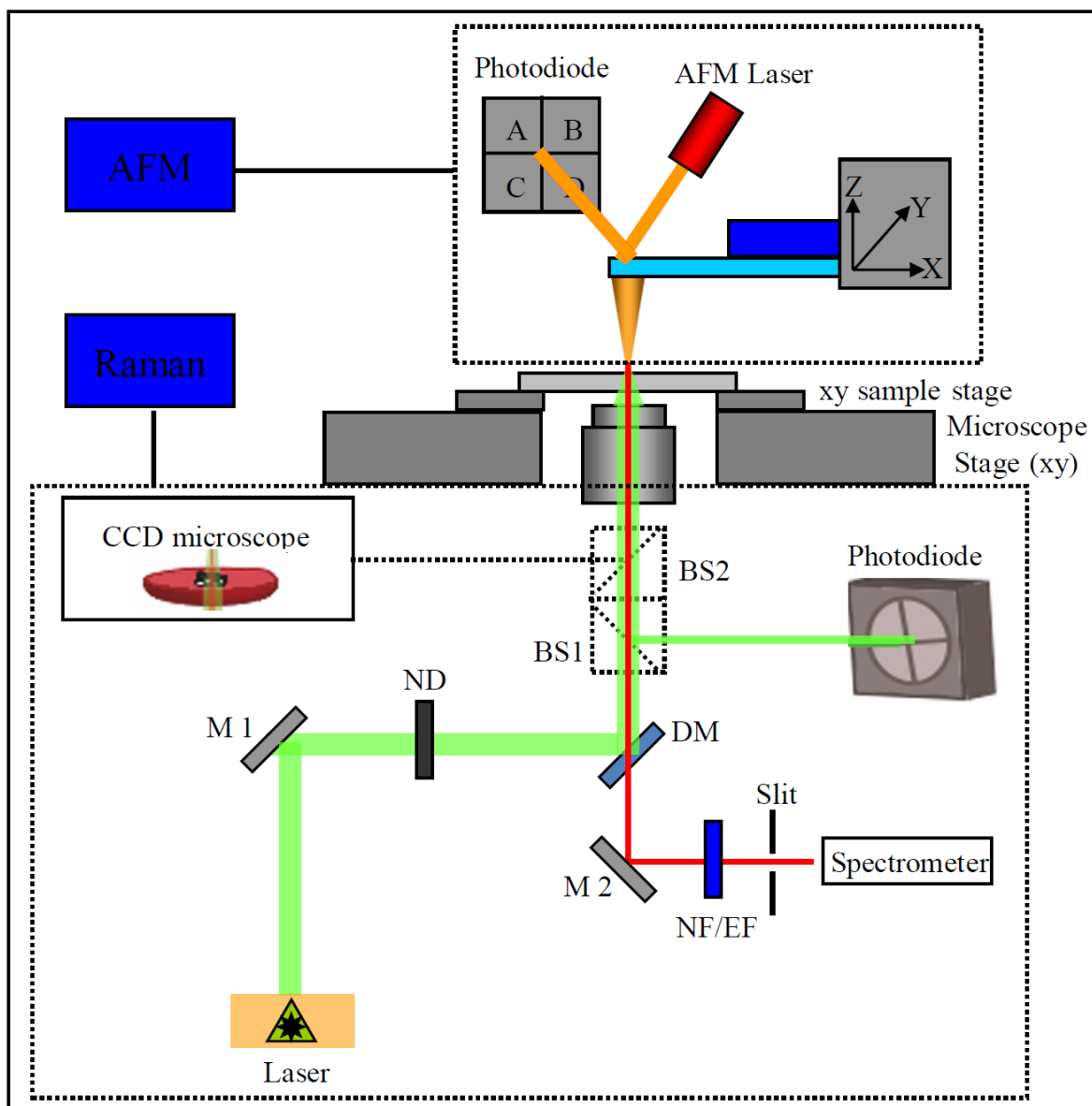


Fig. 3.1: Schematic illustration of the TERS setup 2. M: mirror; ND: neutral density filter; DM: dichroic mirror; BS: beam splitter; NF: notch filter; EF: edge filter.

Chapter 3

TERS setup 2 is schematically shown in fig. 3.1. The monochromatic laser beam (532 nm) is guided by an adjustable mirror (M1) to a neutral density filter (ND) to attenuate the intensity. After passing a dichroic mirror (DM) and two adjustable beam splitters (BS1, 2), the laser beam is focused through an oil immersion objective (60-fold Olympus PlanApo NA 1.45, or 40-fold Olympus UApo N340 NA1.35) onto the sample and the TERS tip. The backscattered light is collected through the same objective and guided by a mirror (M2) via a notch/edge filter (NF/EF) to the Raman spectrometer (Acton Advanced SP2750A, Princeton Instruments, Trenton, NJ, USA). The notch filter eliminates the Rayleigh scattering part of the beam. The edge filter could be longpass and shortpass. The longpass edge filters block off all wavelengths below a given wavelength and therefore it is only employed to measure Stokes-Raman scattering. Shortpass edge filters block off all wavelengths above a given wavelength and are suitable for Anti-Stokes Raman scattering studies. Images of the light microscope are obtained by placing BS1 into the optical path. The AFM head (xyz scanner, NanoWizard II, JPK Instrument AG, Germany) is mounted on a xy microscope stage on top of an inverted microscope (Olympus IX71). The sample is mounted on a xy-piezo sample stage (JPK Instrument AG, Germany) mounted above of the microscope stage.

The configuration of TERS setup 1 is very similar to setup 2. The differences are: the monochromatic laser beam (530.8 nm) first passes an interference filter (IF) to cut the sidebands of the laser beam; the AFM is NanoWizard I from JPK Instrument AG, Germany; and the Raman spectrometer is a LabRam Hr from HORIBA Jobin-Yvon, Edison, NJ, USA.

3.2 The preparation of TERS tips and SERS substrates

TERS tips were obtained from the IPHT. The tips were stored under argon atmosphere and were used within three days after the preparation. The average diameter of the apex of the coated tips is estimated to be approximately 20 nm (fig. 3.2 (a)) but becomes blunt (fig. 3.2 (b)) after measurements. Silver island film evaporated on glass cover slide surface was used as substrate in the present work for SERS measurements. They were obtained from the IPHT too. Prior to evaporation, the glass cover slips were cleaned in a digestion mixture of concentrated HNO_3 : 30% H_2O_2 (3:1) for 2 hours, subsequently rinsing with bidistilled

Chapter 3

water 3 times and dried under vacuum. The silver island film was then evaporated on the glass cover slide surface and annealed under an argon gas stream (1). The substrates were stored under argon atmosphere and were used within three days after the preparation.

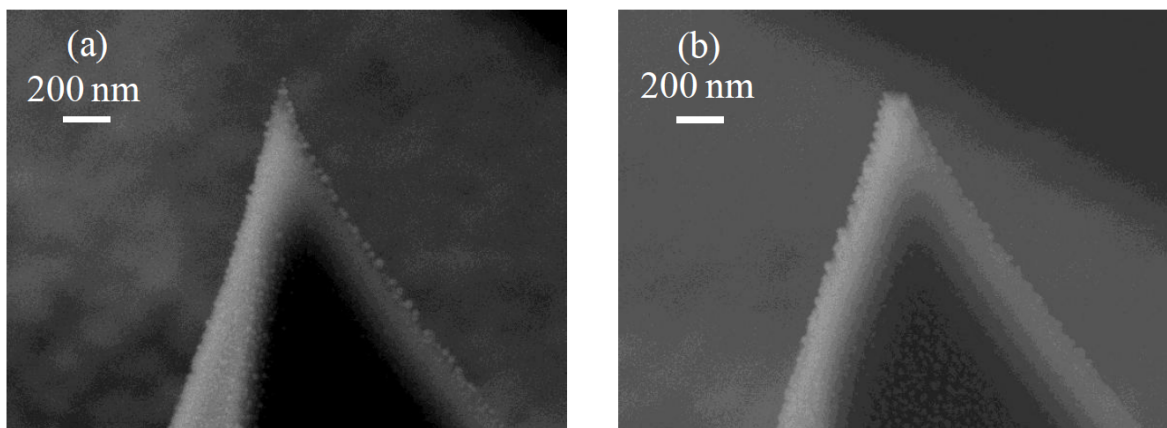


Fig. 3.2: SEM images of (a) a freshly coated TERS tip and (b) a used TERS tip.

3.3 Sample preparation

As has been mentioned, all the present TERS measurements were performed with a bottom illumination / collection mode using an oil immersion objective. To avoid losses of the excitation laser power and the Raman signal, the sample and the sample substrates should be transparent. The oil immersion objective has a low working distance (0.17 mm), for that reason the thickness of the sample substrate is limited. For all the measurements, mica substrates (<0.1 mm thickness, Bal-Tec GmbH, Liechtenstein), clean thin glass cover slides (0.15 mm thickness, Marienfeld GmbH, Germany), or gold nanoplates (spreaded on the surface of glass cover slides) were used as substrates. The mica substrates were freshly cleaved prior to use, by making a small cut between two layers with a razor blade and taking both apart; the glass cover slides were cleaned as mentioned; the gold nanoplates synthesis is described in detail in ref.(2). For each sample, any special sample preparation procedure will be described in the corresponding chapter.

3.4 How to do a TERS measurement

TERS measurements were performed in tapping mode, shown in fig. 3.3. Before every TERS measurement the TERS tip was set within the laser focus. In the coarse alignment the camera image was used to centre the TERS tip above the laser focus spot. Then BS1 was

Chapter 3

replaced by BS2 to guide the reflected laser beam to the photodiode. Thereafter a large region ($\sim 25 \times 25 \mu\text{m}$) was scanned in tip-scanner mode and the reflection and Raman signal of the tip were recorded parallel, the deflection of the tip was located and successively smaller regions around the spot were recorded ($\sim 3 \times 3 \mu\text{m}$). In sample-scanner mode the tip was set on the spot with the highest reflection and within an accuracy of $\sim 200 \times 200 \text{ nm}$. The sample was scanned in xy-direction by a piezo stage and in z-direction by the tip. Then the mode was changed to force spectroscopy and a grid was defined on the topographic image. Finally, TERS spectra at each point in the grid were measured. The laser power and exposure time were adapted individually for each sample.

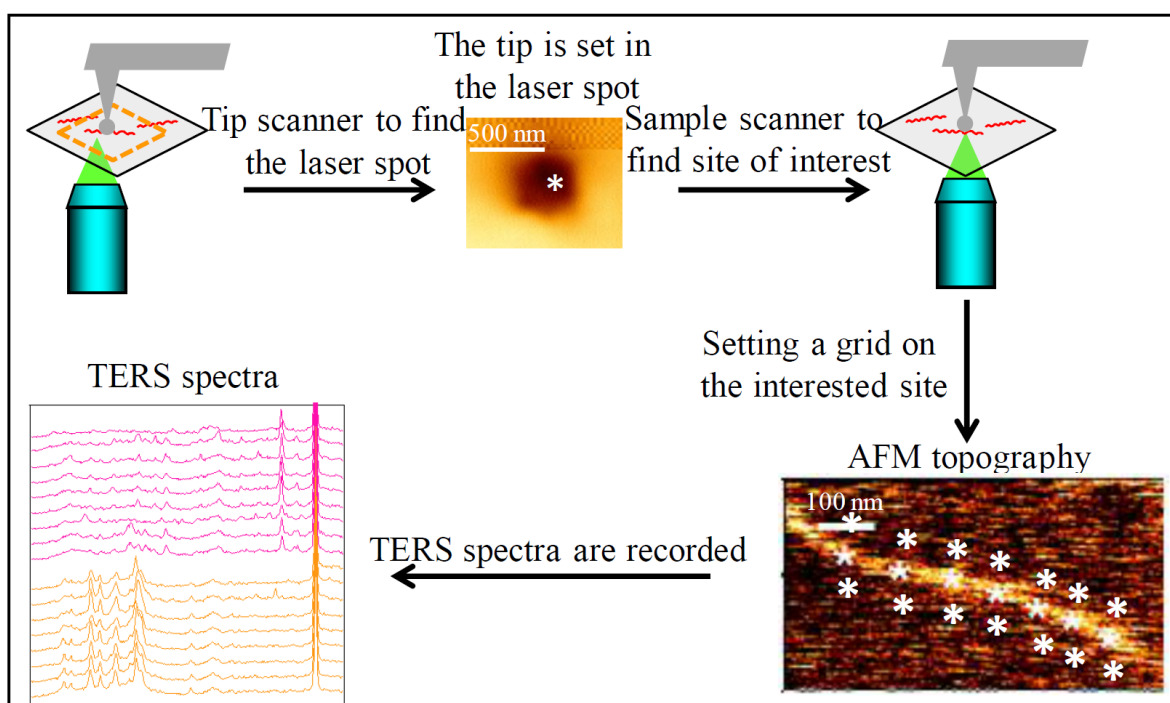


Fig. 3.3: A schematic representation of the TERS measurement procedure.

3.5 References

1. A. Rasmussen, V. Deckert, Surface- and tip-enhanced Raman scattering of DNA components. *Journal of Raman Spectroscopy* **37**, 311 (2006).
2. T. Deckert-Gaudig, E. Kaemmer, V. Deckert, Tracking of nanoscale structural variations on a single amyloid fibril with tip-enhanced Raman scattering. *Journal of Biophotonics* **5**, 215, (2012).

Chapter 4: TERS for label-free DNA sequencing

4.1 The aim of this chapter

The aim of work in this chapter is to evaluate and demonstrate the feasibility of TERS as a label-free DNA sequencing method theoretically and experimentally.

4.2 Introduction

The term “DNA sequencing” refers to the determination of the order of the nucleotide bases adenine (A), cytosine (C), guanine (G), and thymine (T) in DNA strands. It is central to modern molecular biology and molecular diagnostics, because the identification of specific diseases is based on nucleic acid sequence identification. The Sanger method (1) has been the dominant method of the DNA sequencing industry for some 30 years. It is very robust and was employed successfully in the Human Genome Project (2). However the Sanger method is based on the polymerase chain reaction (PCR) amplification and other modifications of the molecules, which is procedurally complex and needs large number of reagents. Furthermore, the Sanger method is still too costly for reading personal genetic codes. Hence numerous improvements are being developed, optimizing various aspects of the sequencing process and current advances show a tendency towards a label-free and direct sequencing with reasonable costs and expenditure of time. Recent approaches in this direction include: electrically read out the base sequence of a single strand when it is translocating through a nanopore (3-5); attempts were also made to directly partially sequence DNA using STM (6, 7); with the feature of providing the inherently distinguishable fingerprint information of different molecules without labeling, SERS and TERS are also used to study the DNA molecules (8-12).

In this chapter the structure of DNA and RNA will be introduced. Followed by the introduction of the different methods for DNA sequencing and detection, I will focus on the basic principles and challenges of these methods and compare them to TERS as a label-free direct DNA sequencing method. Last but not least, TERS measurements on uracil polymer, calf thymus DNA, and $(A_{10}C_{15})_8$ DNA single strands will be shown to demonstrate the feasibility of TERS as a direct DNA or other polymeric bio-macromolecules sequencing method.

Chapter 4

4.2.1 Structure of DNA and RNA

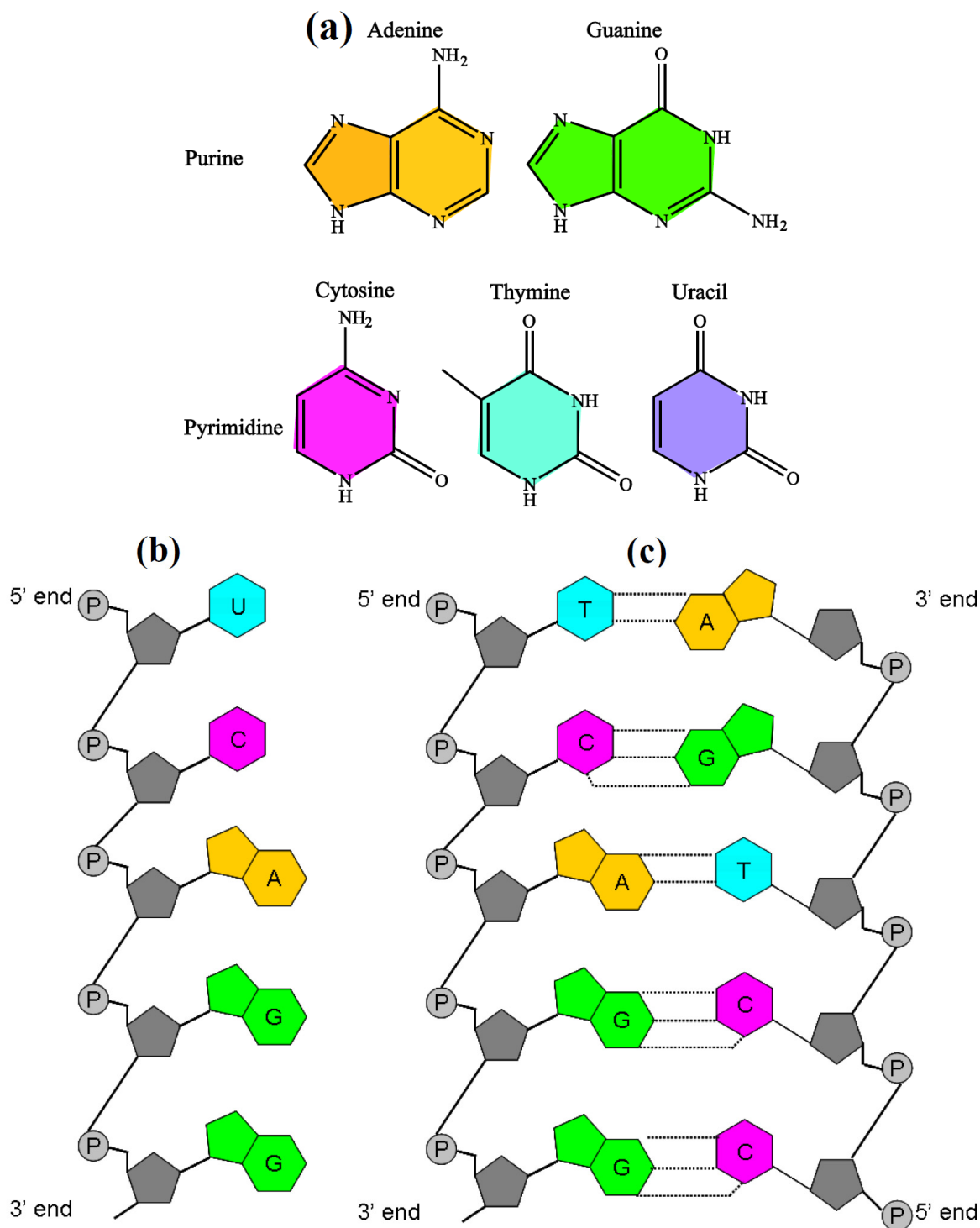


Fig. 4.1: (a) Molecular structure of the DNA and RNA nucleobases. The structure of DNA helix (b) and RNA single strand (c). A: adenine; C: cytosine; G: guanine; T: thymine; U: uracil.

Chapter 4

DNA and RNA are the two different nucleic acids found in the cells of living organisms. Both play significant roles in cell biology and are composed of three groups: phosphates, sugars and nucleobases. The backbone is built of phosphates and sugars, which in the case of DNA are deoxyriboses and in the case of RNA, riboses. Four nucleobases are found in DNA: adenine (A), guanine (G), cytosine (C), and thymine (T); in RNA, uracil (U) replaces thymine. These five bases can be classified into purine bases (adenine and guanine) and pyrimidine bases (cytosine, thymine and uracil), see fig. 4.1 (a). DNA naturally is a double helix strand with complementary chains: each adenine of one strand is paired with a thymine of the other strand (via two hydrogen bonds) and each guanine is paired with a cytosine (via three hydrogen bonds, fig. 4.1 (c)). In contrast to DNA, most RNA molecules are single-stranded, fig. 4.1 (b). The height, width, and base-to-base distance of DNA single and double strands are shown in table 4.1 (7, 13-15)

Table 4.1 The height, width (AFM measured) and base-to-base distance of DNA single and double strands (7, 13-15)

	DNA single strand	DNA double strands
Height	0.2-0.8 nm	0.6-1.2 nm
Width	10-15 nm	10-20 nm
Base-to-base distance	0.5-0.7 nm	0.34 nm

4.2.2 DNA sequencing and detection methods

Rising interest in genomic research and whole-genome sequencing with reasonable costs and expenditure of time resulted in recent developments of novel sequencing technologies. Those sequencing systems include a number of non-Sanger ultra-high-throughput methods, which have been reviewed for instance in ref. (16, 17). Here we put our emphasis on the direct and electronic sequencing by using nanopore and STM. They in principle do not require any amplification of DNA template, which is in contrast to the Sanger method. SERS and TERS as another two label-free spectroscopic methods for DNA study are introduced here as well.

Chapter 4

4.2.2.1 Nanopore method

Unlike the Sanger method, the ideal nanopore sequencing approach would not require fluorescent labels or element labels and would use unamplified genomic DNA, thus eliminating enzymes, cloning, and amplification steps and has therefore attracted a lot of interest. Fig. 4.2 schematically illustrates the principle of a nanopore sequencing system. A nanopore separates two compartments filled with salt buffer, both are connected to electrodes. A constant voltage bias is applied between the two electrodes inducing a steady-state ionic current through the pore, which is measured by the amplifier. Adding a single stranded DNA (ssDNA) to the negatively biased compartment leads to transient reductions of the ionic current. This reduced conductance is associated with the translocation of DNA through the pore, which partially blocks the ionic current. Theoretically, each nucleobase induces a specific change in the ionic current flow as a result the sequence can be deduced by measuring the ionic current during the translocation. Nanopore research uses either biological pores like protein α -hemolysine or solid-state nanopores, like silicon nitride. Biological pores exhibit a lower noise level than solid-state phases, whereas solid-state nanopores show superior chemical, thermal, and mechanical stability over the biological counterpart, and have the potential of integration into devices (16, 18-20).

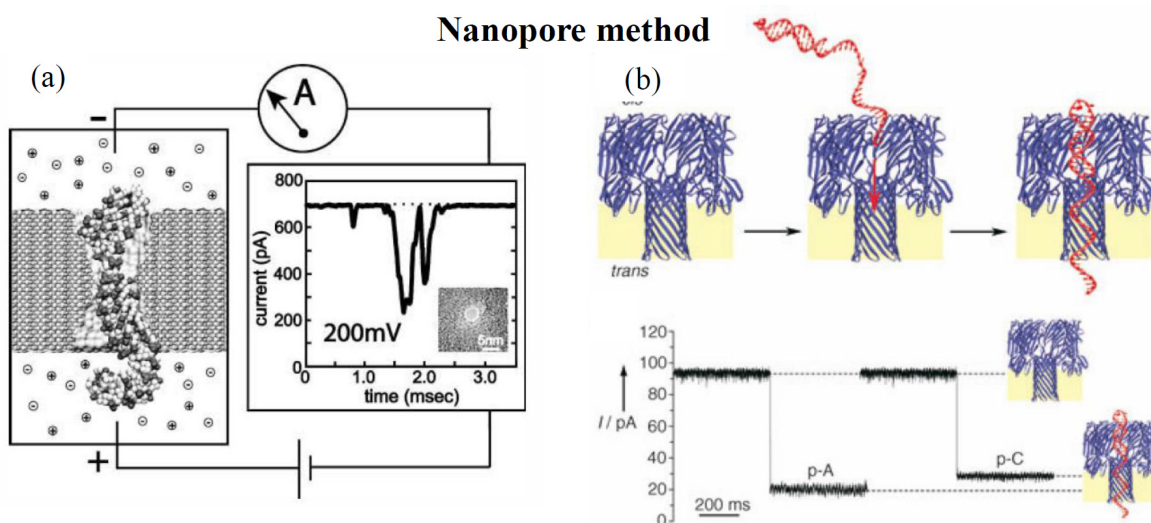


Fig. 4.2: Experimental setup for measuring characteristic ionic currents of a nanopore that conducts a DNA strand, (a) Solid-state pore; (b) Protein pores, adapted from (20, 21).

Chapter 4

For several reasons it is not so easy to realize the nanopore method in practice. Firstly, the bases have similar chemical structures resulting in only small differences of the electric signal. To detect small signals, approaches are needed to reduce interference from the measurement environment, and/or to amplify the signals by modifying nucleotides or employing an optical, electric, or magnetic stimulus. Secondly, noise in the ionic blockade, due to both intrinsically ionic fluctuations and structural fluctuations of the nucleotides, is likely to be too large to successfully distinguish the bases. Last but not least, a finite thickness or electric “read” region (~ 3 nm) of the channel of a nanopore might place a fundamental restriction on the single-base resolution because at least 4-6 nucleotides of ssDNA extend through a channel and thus all these nucleotides together contribute to the ionic current blockage. To detect the effect of individual nucleotides on the ionic conductance, a nanopore with channel length comparable to that of a single nucleotide (~ 0.5 - 0.7 nm) is required. Monolayer graphene sandwiched between two insulating layers may meet this requirement (16, 18, 19, 21).

If these challenges could be overcome, nanopore sequencing has the great potential for ultra-rapid sequencing DNA with drastically lower cost per genome, allowing for an extensive application in medical diagnostics (16, 19, 21).

4.2.2.2 STM method

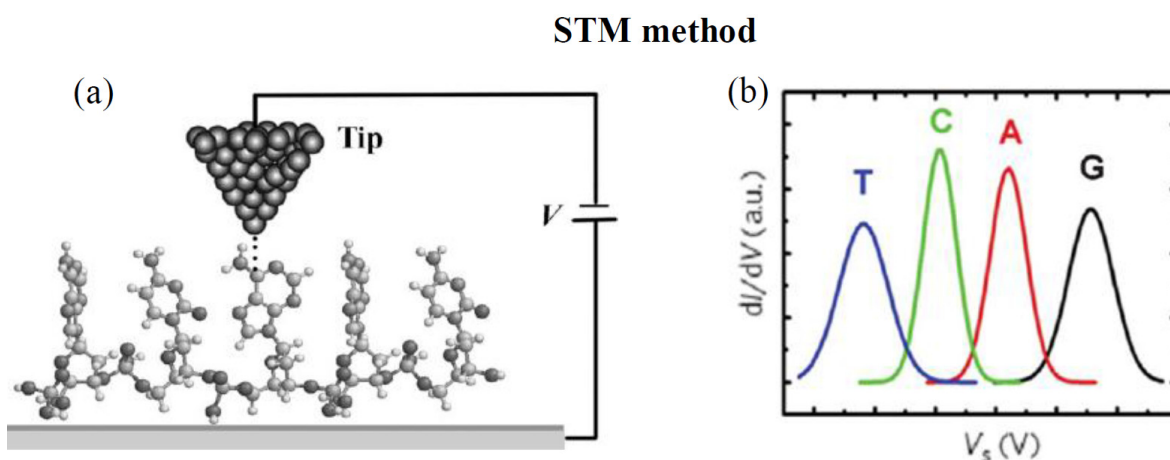


Fig. 4.3: Schematic images of STM-based DNA sequencing. **(a)** An ssDNA molecule with bases regularly aligned is prepared on an ultrathin insulating layer that is deposited on a

Chapter 4

conductive substrate. **(b)** Each base has distinct electronic state showing different electronic signal in the I-V curve, which used to sequence DNA strands, adapted from (16).

The principle of STM for DNA sequencing is that STM images represent images of the local density of states at the Fermi level projected to the tip apex above the sample surface. Thus, although STM lacks chemical sensitivity, it can, in principle, be used to detect DNA sequences if there is a difference in electronic characteristics among the four bases. The schematic images of STM-based DNA sequencing are shown in fig. 4.3 (16).

In 2009, Tanaka and Kawai reported partial sequencing of a DNA single strand with a STM by using an oblique pulse-injection method to deposit the molecules onto a copper surface. First, they show that some bases appear brighter in the conductance image (the derivative of the current–voltage (I–V)) curve obtained at a chosen bias voltage than the other nucleobases of the stretched single-stranded DNA (22) by using low-temperature ultra-high vacuum (UHV) STM. By comparing to the known sequence of the DNA strand, the brighter bases were identified as the guanine, which have a distinct electronic state that allows them to be distinguished from the other nucleobases. These results show that it is possible to sequence individual guanine bases in real long-chain DNA strands with high-resolution STM imaging and spectroscopy (7).

When DNA bases interacted with a single-walled carbon nanotube (SWCNT), Kaxiras et al (23) found theoretically 100% nucleobase identification based on the electronic characteristics among the four DNA bases. These reports indicate the possibility of sequencing DNA using the STM technique. However, the different electronic properties of carbon nanotubes (CNTs) depend on their chirality and diameter, and DNA wrapping around CNTs (orientation issue) makes it experimentally difficult to access individual bases along the DNA molecule. Thus it still has to be proved if the identification of all four bases is possible by STM. Furthermore, the success of single-molecule sequencing using STM relies heavily not only on the detection techniques but also on the preparation of DNA samples. How to prepare a linear ssDNA with base resolution sample on a solid-state surface is a great challenge STM-based sequencing has to face. The STM-based method

Chapter 4

does not require imaging of the internal atomic structure of bases, but it requires single-base resolution, so that the STM tip can be located on top of each base individually.

Similar to the sample preparation for nanopore sequencing, the genomic DNA needs only to be isolated and separated into ssDNA, and modifications such as cloning of DNA fragments with subsequent amplification and fluorescent labeling are not required in STM sequencing. An STM-based approach may support ultrafast sequencing, considering its fast scan speed. (16).

4.2.2.3 SERS method

The Raman spectra of the four bases present in DNA are different. Especially the ring breathing modes of the bases show characteristic and well distinguishable bands in the region from 600 to 810 cm^{-1} . Combining the distinction in Raman spectra of the four DNA bases with the huge enhancement effect of the rough metal substrates, SERS is used for DNA studies. The vast majority of current DNA detection using SERS involves the use of dyes labeling as part of the signal transduction for stronger and more distinguishable Raman signal, requiring costly chemicals and complex chemistry (24, 25), which are not going to be discussed here. We only introduce SERS for label-free direct DNA detection.

Although numerous SERS studies of DNA have been performed to date, sensitive and reliable acquisition of SERS spectra from DNA samples remains a significant challenge. For example, in one study, it was reported that the quality of the SERS spectrum of single-stranded calf thymus DNA was much better than that of the double-stranded DNA (dsDNA) (26). Another study reported that although all dsDNA samples yielded SERS spectra with good signal-to-noise ratios (SNR), none of the ssDNA oligomers studied yielded detectable SERS signals (27). More recently, SERS detection of both single- and double-stranded DNA was reported, where the observed SERS features appeared to be sequence- and/or composition-dependent (28).

Differences in these reports may be attributed to the different structures of the SERS substrates leading to large variations in molecular conformation and/or packing density of

Chapter 4

the DNA adsorbate molecules on the substrates. For early DNA studies, Au or Ag aggregated colloids are the most commonly used SERS substrates, which are negatively charged, on the other hand, DNA strands are negatively charged too because of the phosphate backbone, which resulted in the random and unstable absorption of the strands to the substrate surface.

To improve the reproducibility of SERS measurements and the SNR of the DNA spectra, the Halas group used Au nanoshells as highly reproducible SERS substrates for direct thiolated ssDNA and dsDNA detection (11). Their results show that a gentle thermal cycling pretreatment of the ssDNA and dsDNA prior to adsorption onto the nanoshell substrate results in extended DNA chains with a significantly greater uniformity of molecular conformation than that of untreated, randomly coiled DNA chains. Adsorption of the thermally pretreated, relaxed DNA strands onto the nanoshell substrate surface is quite likely to also result in a more ordered and densely packed monolayer on the nanoparticle surfaces relative to DNA strands adsorbed in randomly coiled conformations. This protocol results in a dramatic increase in reproducibility of the SERS spectra with good SNR because thiolated ssDNA and dsDNA oligomers specifically and strongly bind to Au nanoshell-based novel SERS substrates. However, it is also found that spectra obtained using this preparation method show an overwhelming dominance of adenine vibration modes in the SERS spectra. The features from guanine (G), cytosine (C), and thymine (T) are not detectable, regardless of the position or percentage of adenine in the sequence. The dominance of adenine is attributed to its higher SERS cross section than other three DNA bases, which is in the order of $A > C \gg G \geq T$ (11).

In contrast to Halas's results, Papadopolou and Bell show in their report that it is possible to obtain distinctive SERS spectra of unthiolated DNA sequences, which can be used to detect a single-nucleotide mismatch (12). They use aggregated Ag colloids as SERS substrates and instead of the commonly used NaCl, $MgSO_4$ is used as electrolyte for aggregation, which does not bind as strongly to the silver surface and therefore allows the DNA sequence to nonspecifically bind with its bases. It is reported that even without thiol group for binding and thermal treatment for strand extension, the spectra of DNA strands

Chapter 4

are not dominated by the adenine modes, but show bands from all bases with high reproducibility and good SNR. This approach can be used to detect a single-nucleotide mismatch by digitally subtract SERS spectrum of two DNA single strands with only one base in sequence differences (12). Furthermore, the results of Halas and Bell et al point out the importance of colloids treatment for SERS experiment in general.

4.2.2.4 TERS method

TERS investigation on DNA was firstly performed on single nanocrystal of adenine (29-31), which has been introduced in chapter 2, section 2.3.5.

Further TERS experiments on DNA bases were thymine and cytosine (32). TERS spectra of nanometre-sized crystals of the DNA pyrimidine bases cytosine and thymine were collected and compared to SERS and Raman spectra, which clearly demonstrated the feasibility of TERS for DNA sample detection. In further experiments TERS spectra were recorded on (sub) monolayers of all four DNA bases, adenine, cytosine guanine and thymine adsorbed on Au (111) single crystal surface (33). The results show the extraordinary spectral sensitivity or even single molecule detection feasibility of the gap-mode TERS and the distinction of all four DNA bases. Gap-mode TERS was also used to study the hydrogen bonds formed between complementary DNA bases in DNA double helix, demonstrating the feasibility of TERS in estimating the interaction geometry of the molecules with respect to the metal surface as well as the respective strength of the bonds (34).

TERS experiments were carried out on single-stranded RNA after the analysis of the isolated DNA bases (35). TERS spectra were collected on seven adjacent positions along a strand. Spectra obtained at different positions were highly similarity, which demonstrated the stability of the setup and the reproducibility of TERS spectra. Slight fluctuations of peak frequency and peak intensity can be observed by a closer look at the spectra, which were found in the previously mentioned TERS spectra of adenine crystals as well and can be attributed to the specific interactions of the molecule with the silver coated tip surface and probe positioning variations (29-31). Furthermore, considering the SNR and the

Chapter 4

illuminated area in the TERS spectra, single-base sensitivity was achieved hence label-free DNA sequencing using TERS was proposed (35).

4.3 Materials and methods

4.3.1 Materials

The single-stranded uracil homopolymer and calf thymus DNA were purchased at Sigma-Aldrich; the single-stranded (A₁₀C₁₅)₈ were purchased at Integrated DNA technologies; all other chemicals used for buffer solutions and gold nanoplates syntheses were purchased either at Sigma-Aldrich or VWR international.

4.3.2 Sample preparation

The uracil homopolymer was dissolved in water and immobilized on gold nanoplates surface (36, 37). The gold nanoparticle synthesis is described in detail in ref. (38). Prior to the immobilization, the uracil homopolymer solution was heated to 90 °C for 10 min, followed by rapid cooling in an ice bath for 10 min to stretch the RNA single strands (thermal pretreatment (11)). 10 µL 10 ng/µL of the pretreated polyuracil solution was dropped on the gold substrate and incubated under an argon atmosphere for 2 hours. Excess RNA strands were removed by rinsing with bidistilled water and subsequent drying under argon.

Calf thymus DNA was dissolved in 10 mM 4-(2-hydroxyethyl)-1-piperazineethanesulfonic acid (HEPES) to maintain a physiological pH value. 10 mM magnesium chloride (MgCl₂) was used to fix the strands through the negatively charged phosphate backbone by means of divalent cations (Mg²⁺) on negatively charged mica. The concentration of calf thymus DNA was 10 ng/µL. The above mentioned thermal pretreatment is used for the strands immobilization as well. 1-2 µL of the calf thymus DNA solution was dropped on a freshly cleaved mica sheet and incubated under an argon atmosphere until dry. Residues from the buffer were removed prior to the TERS measurements by rinsing with bidistilled water and subsequent drying under argon (35, 39).

Chapter 4

The immobilization of $(A_{10}C_{15})_8$ DNA single strands on mica surface was analogous to the calf thymus DNA.

4.3.3 TERS measurements

TERS measurements on all the RNA/DNA samples were performed on setup 2, which has been introduced in the experimental chapter. For TERS measurements on uracil polymer, calf thymus DNA, and $(A_{10}C_{15})_8$, the laser intensity at the sample were set to 860 μ W, 700 μ W and 750 μ W respectively with an acquisition time of 5s for all measurements.

4.4 Results and discussion

4.4.1 Proposal of DNA sequencing using TERS (35)

The proposal of DNA sequencing using TERS is based on the distinctive features of the TERS technique:

- (1) The Raman signal of each nucleobase is unique and distinguishable with respect to the ring breathing modes. As the molecular structures of the four DNA nucleobases are similar, their spectra show similarity except for the ring breathing mode positions in the region from 600 to 810 cm^{-1} (10).
- (2) The high spectral sensitivity (single molecule) (35, 40-42) and high lateral resolution of TERS (2-3 nm) (43-45).

Therefore, in the proposed method, theoretically, due to the high spectral sensitivity and high lateral resolution of TERS, ~ 5 nucleobases can be detected in each spectrum, thus the sequence information of a DNA single strand can be reconstructed by laterally shifting the tip in intervals of one base-to-base distance (fig. 4.4) and then deduce the spectra (fig. 4.5, table 4.2).

To manually deduce and reconstruct the sequence of a DNA single strand in principle, a simplified model is established:

1. The lateral resolution of the enhanced electromagnetic field is only ~ 2.0 nm (5 nucleobases), assuming a base-to-base distance within a DNA single strand of approximately 0.5 nm, fig. 4.4 (a), (b))

Chapter 4

2. The Raman enhancement curve of the electromagnetic field produced by exciting the plasmons of the TERS tip is assigned to show a triangular distribution (fig. 4.4 (b)).
3. Only the ring breathing mode of the nucleobases is used (fig. 4.5, adenine: 742 cm^{-1} ; cytosine: 790 cm^{-1} ; guanine: 674 cm^{-1} ; thymine: 809 cm^{-1}) to represent the TERS spectra.

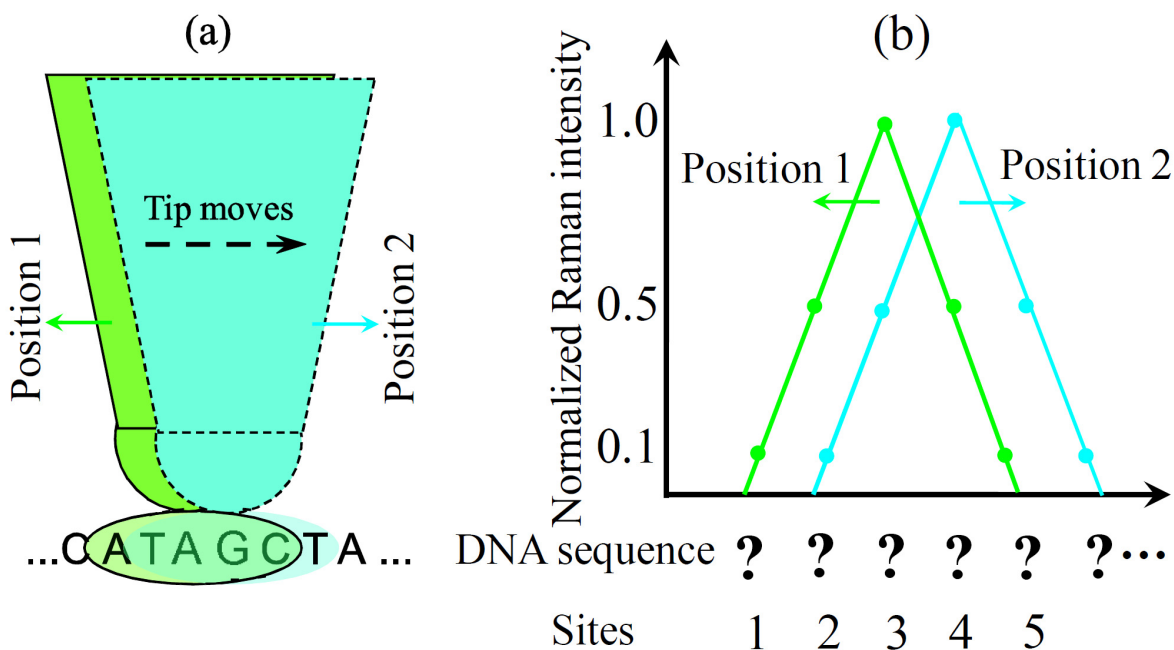


Fig. 4.4 Schematic diagram of a direct DNA sequencing procedure using TERS, (a) TERS tip is laterally shifted in intervals of one base-to-base distance from position 1 (green) to position 2 (light blue). The colored sites underneath the tip refer to the enhanced regions. (b) The corresponding normalized Raman enhancement is in a triangular distribution curve. To simplify the sequence deduction procedure, it is assumed that the lateral resolution of the tip is only $\sim 2.0\text{ nm}$, which means 5 nucleobases are located in the enhanced region (a) and 5 sites (one site located in one nucleobase) in the curve (b).

In fig. 4.4 (a) the TERS tip is laterally shifted along a DNA single strand from position 1 (green) to position 2 (light blue) in one nucleobase interval. The colored sites underneath the tip refer to enhanced regions, which are assumed to be only $\sim 2.0\text{ nm}$ (5 nucleobases) to simplify the DNA sequence deduction and reconstruction procedure. In fig. 4.4 (b) their corresponding normalized Raman enhancement curves are in a triangular distribution, in

Chapter 4

each of which there are five sites. Every site is located with a nucleobase and their corresponding normalized Raman enhancement factors are 0.1, 0.5, 1.0, 0.5 and 0.1, respectively (from left to right). In the curve of position 1 every nucleobase exhibits a specific Raman signal intensity in the spectrum (fig. 4.5, position 1), while in the curve of position 2 every nucleobase exhibits a different Raman signal intensity (fig. 4.5, position 2). Regarding adenine for instance, the measured normalized Raman intensity in position 1 and 2 are 1.1 and 0.5 respectively. The normalized 1.1 Raman intensity corresponds to four kinds possible positioning. When the TERS tip is laterally moved to the left for one-base distance, only one of the four possible positionings fits the 0.5 normalized Raman intensity in position 2. Therefore it can be deduced that site 1 and site 3 are located with adenine. By this method the nucleobases located in the left sites underneath the tip can be all deduced and the sequence information of a small segment (in the enhanced region of the TERS tip) in the DNA single strand is finally reconstructed, which is ATAGC as shown in table 4.2. By continuously shifting the TERS tip along a DNA single strand in a base-to-base interval and deducing the spectra in the described method, the sequence of the whole DNA single strand can be reconstructed.

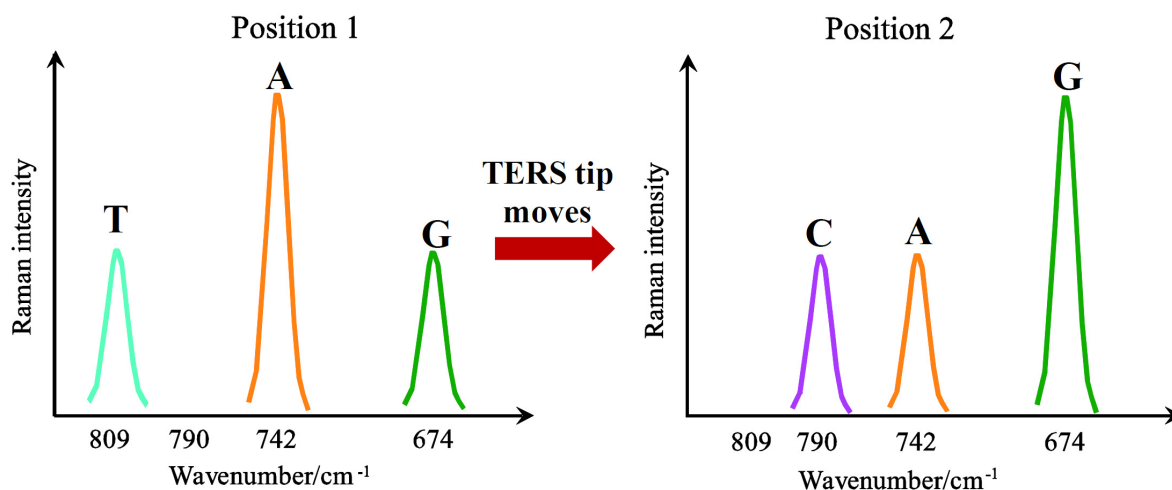


Fig. 4.5 Simulated TERS spectra obtained in position 1 and position 2. The spectra show the Raman signal intensities of every nucleobase adenine (A, orange, 742 cm⁻¹), cytosine (C, purple, 790 cm⁻¹), guanine (G, green, 674 cm⁻¹), thymine (T, light blue, 809 cm⁻¹)) and their changes when the tip moves.

Chapter 4

Table 4.2 The positioning of every nucleobase in the triangular distribution curve and the sequence reconstruction of a small segment (in the enhanced region of the TERS tip) in the DNA single strand. A=Adenine, C=Cytosine, G=Guanine, T=Thymine. The subscripts “1” and “2” represent position 1 and 2 respectively.

Normalized Raman intensity	The possible positioning					Normalized Raman intensity when the tip is laterally moved to the left for one-base distance
	Site 1	Site 2	Site 3	Site 4	Site 5	
$A_1=1.1$ $A_2=0.5$	A		A			$A_2'=0.5$, fits $A_2=0.5$
			A		A	$A_2'=1.0$, does not fit $A_2=0.5$
	A	A		A		$A_2'=1.1$, does not fit $A_2=0.5$
		A		A	A	$A_2'=1.6$, does not fit $A_2=0.5$
$C_1=0.1$	C					$C_2'=0$, does not fit $C_2=0.5$
$C_2=0.5$					C	$C_2'=0.5$, fits $C_2=0.5$
$G_1=0.5$		G				$G_2'=0.1$, does not fit $G_2=1.0$
$G_2=1.0$				G		$G_2'=1.0$, fits $G_2=1.0$
$T_1=0.5$		T				$T_2'=0.1$, fits $T_2=0.2$ if site 6 is T
$T_2=0.2$				T		$T_2'=1.0$, does not fit $T_2=0.2$

4.4.2 Important experimental prerequisites required for the realization of DNA sequencing using TERS

Now the procedure of DNA sequencing using TERS has been discussed theoretically. However, to experimentally realize it, several prerequisites should be considered, as for instance the reproducibility of TERS spectra, detection and distinction of all the four nucleobases in DNA single strands, SNR of the TERS spectra and the resolution of the tip.

The reproducibility of TERS spectra is essential for the DNA sequence deduction and reconstruction. Here the “reproducibility” means the main features of a component as for instance cytosine homopolymer are shown in its spectra, although the spectra are obtained on

Chapter 4

the different positions along the single strand. The TERS spectra of cytosine and adenine homopolymer immobilized on a mica surface from different positions are similar and slight changes in band intensity and position can be attributed to the “nano-scale effect” of TERS (35, 46). TERS spectra measured on a uracil homopolymer strand immobilized on an atomic-flat gold nanoplate surface will further confirm the reproducibility.

Although the molecular structures of the four DNA nucleobases are similar and their Raman (and TERS) spectra are distinguishable (10, 32, 33), it was found that SERS spectra of DNA strands are overwhelmingly dominated by the SERS features of their adenine constituents, which prevents the detection of the features from other nucleobases. This was explained with the much higher Raman scattering cross section of adenine compared to the other nucleobases (11). A detailed discussion of this phenomenon is given in the previous section. However, for DNA sequence, all the four nucleobases must be detectable and distinguishable, which is a challenge TERS must overcome.

To sequence a DNA single strand, a high SNR reaching single-base sensitivity is necessary, which already been achieved in several TERS measurements (35, 40-42).

Consequently, the sequencing is experimentally possible if the above mentioned prerequisites are met. However, when it comes to spectra deduction for reconstructing the DNA sequence as mentioned in section 4.4.1, obviously the higher the lateral resolution is, the easier the procedure will be. If the resolution is as high as a single base (0.5 -0.7 nm) then the construction procedure is even not necessary. It is difficult to accomplish the deduction and reconstruction manually when the number of nucleobases exceeds 9. In that case, a computational method should be considered.

4.4.3 TERS spectra of uracil homopolymer – reproducibility of TERS spectra

The dependency of the electromagnetic field enhancement of TERS on the metallic and dielectric substrates was shown in three-dimensional finite-difference time domain (3D-FDTD) simulations (47). A metal substrate (e.g. gold), where the molecules of interest are adsorbed, provides an additional field enhancement as it produces a large electromagnetic

Chapter 4

(EM) coupling with the tip, which is called “gap mode”. In contrast, dielectric materials can not couple, hence, in this case the effect relies on the isolated tip, resulting in a smaller enhancement (47, 48). Here, TERS measurement was performed on uracil homopolymer on gap-mode with the purpose of getting the theoretically predicted strong Raman signal.

Prerequisites for a metal substrate suitable for TERS experiments on single stranded DNA or RNA are: 1) an almost atomic flatness of the surface to avoid the SERS effect resulting from the substrate itself. 2) As the used TERS setup is operated in back-reflection mode (i.e., through the substrate and back), transparency, i.e., the substrate has to be sufficiently thin. A suitable approach is the usage of triangular and hexagonal flat and transparent gold (38) or silver (49) nanoparticles that are large enough to be easily localized with an optical microscope and to avoid localized enhancement regions .

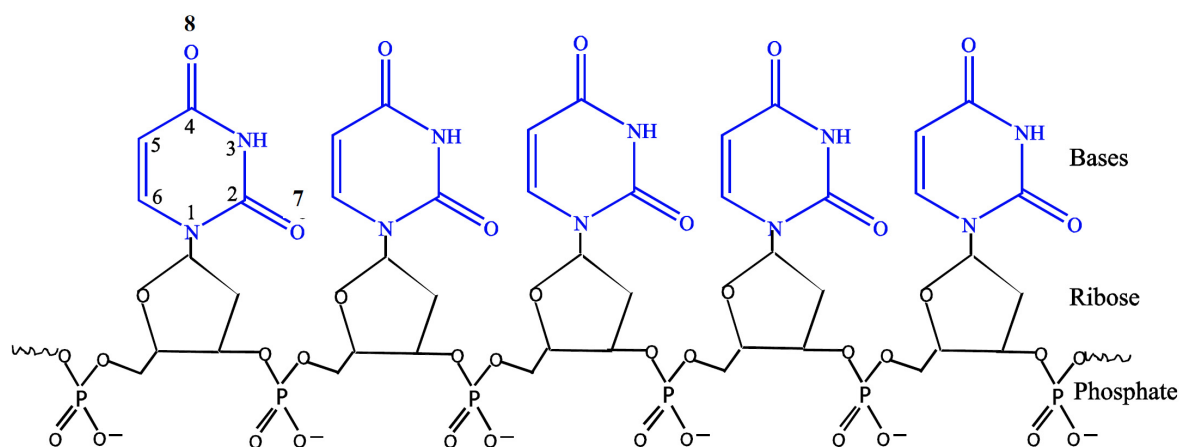


Fig. 4.6: Chemical structure of the uracil homopolymer single strand and the numbering of the purine ring used for expressing the normal modes of vibrations.

In the experiment described here, TERS spectra were collected on a single strand uracil homopolymer (chemical structure is shown in fig. 4.6) immobilized on a gold nanoplate. Fig. 4.7 shows the AFM topography of the uracil strand immobilized on a typical gold nanoplate substrate. TERS spectra were obtained at five different positions on the strand and shown in fig. 4.8. In addition a reference spectrum was recorded on pure gold to exclude signals due to tip contamination (position 0).

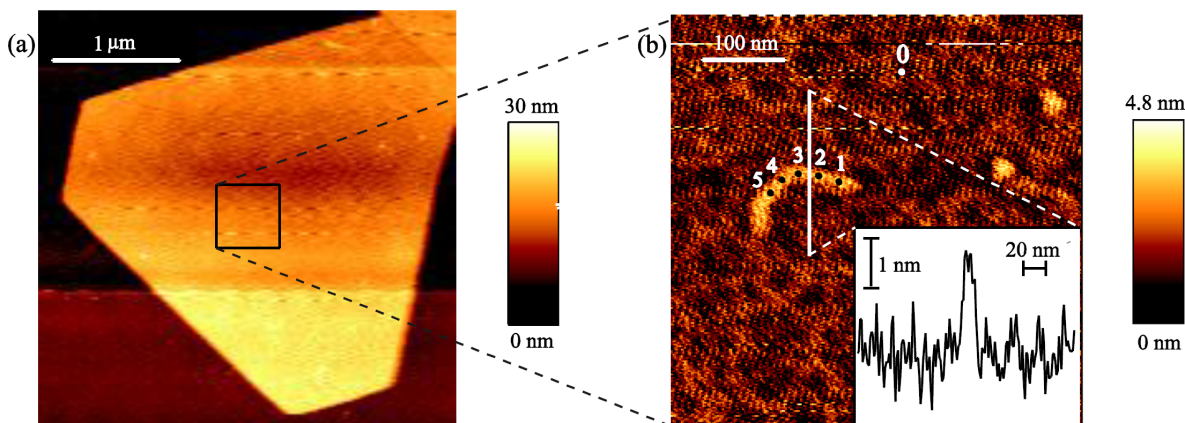


Fig. 4.7: (a) AFM topography image of a gold nanoplate with immobilized uracil homopolymer strands, (b) single strand of uracil homopolymer in the magnified area indicated in (a). Inset in (b) is the topographic cross section corresponding to the line indicated in (b), adapt from (46).

The uracil homopolymer spectra look remarkably uniform and all main spectral features of the base can be assigned, see table 4.3. Minor variations in band intensity ratios and positions can be easily attributed to the previously discussed effects related to the high lateral resolution (50). Surprisingly, the usually intense ring breathing mode of uracil at 800 cm^{-1} is not visible in the spectra. As those vibrations that involve polarizability changes parallel to the TERS tip main (z-) axis are expected to be more enhanced than perpendicular vibrations, the lack of the ring breathing mode may be due to a flat orientation of the ring on the gold surface, which corresponds to the literatures that the pyrimidine ring nonspecific adsorbs on the gold nanoplate surface (36, 37). Similar effects were found to influence the ring breathing mode of aromatic amino acids (51). Apart from this difference the spectral features can be attributed solely to uracil and no signals of the sugar and phosphate backbone were found. This suggests a strong immobilization of the homopolymer on the gold surface through the phosphate backbone. This finding, however, somewhat contradicts the idea of a flat orientation of the ring with respect to the gold substrate, and no explanation can be given at the moment.

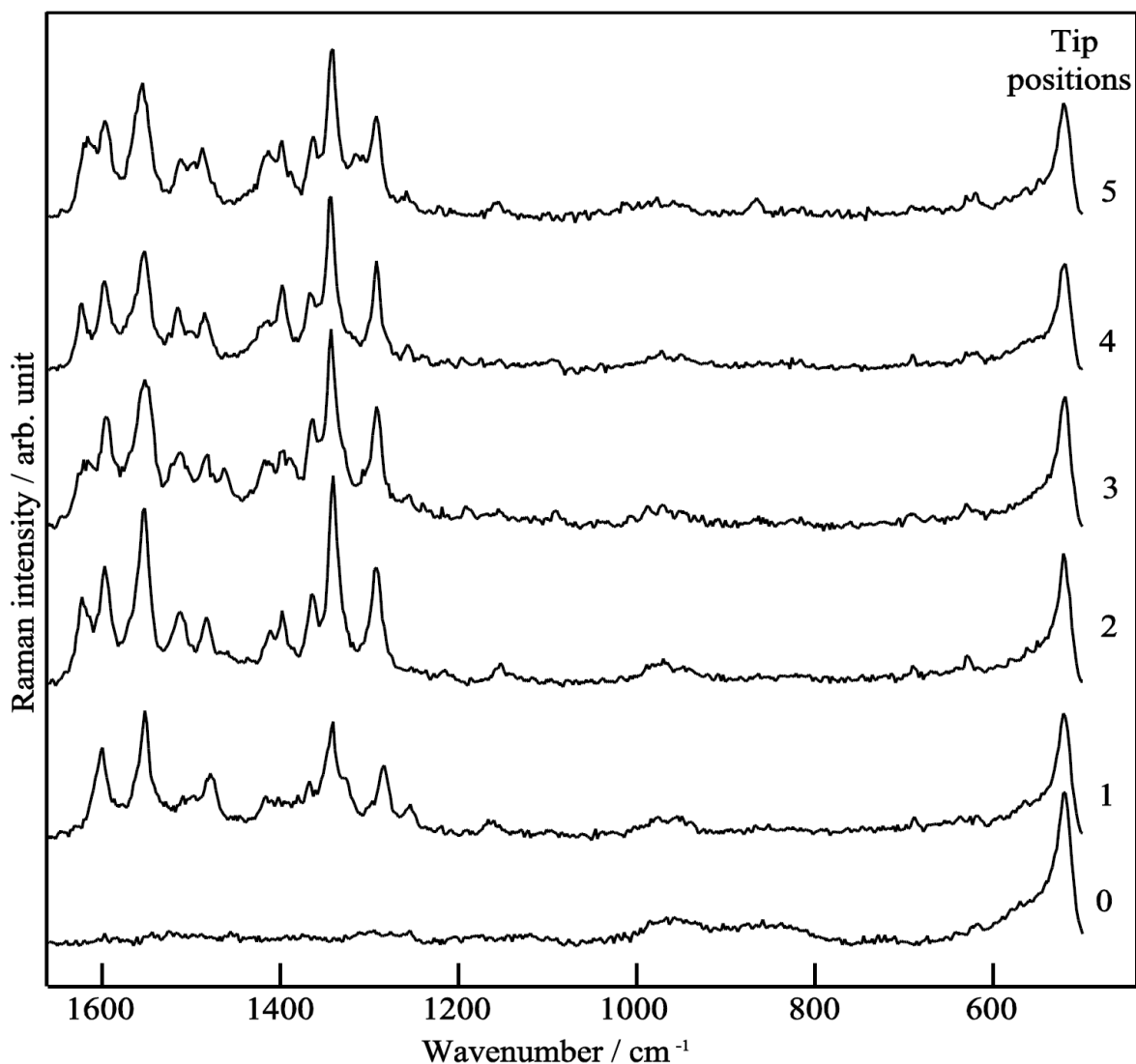


Fig. 4.8: TERS spectra of the uracil homopolymer, measured at the positions indicated in fig. 4.7 (b). An assignment of the signal is provided in table 4.3.

As has been mentioned before, the band positions of the ring breathing modes of four DNA bases are different and are the most prominent bands used to distinguish between them. But when gold nanoplates were used as substrate, it is quite often that the bases flatly adsorbed on the surface resulting in the non-detectable of the ring breathing modes (like uracil homopolymer). Therefore, for the rest TERS measurements on DNA strands we preferred mica but not gold nanoplates as a substrate.

Chapter 4

Table 4.3: Band assignment of the TERS spectra of the uracil homopolymer (cm^{-1})

1	2	3	4	5	Tentative assignment
521	521	521	521	521	Silicon-AFM tip
1254	1252	1257	1257	1259	str N_3C_4 , bend N_1H , C_5H , C_6H (52)
1283	1292	1292	1292	1292	str N_3C_4 ($-\text{C}_4\text{C}_5-\text{C}_6\text{N}_1$), bend N_1H , C_5H , C_6H (53)
1341	1341	1343	1343	1343	bend N_3H , C_5H , C_6H , str C_2N_3 (53, 54)
1367	1365	1363	1367	1363	str $\text{N}_1\text{C}_2-\text{C}_2\text{N}_3+\text{C}_4\text{C}_5$ ($-\text{C}_2\text{O}_7$), bend C_5H (52)
	1398	1396	1398	1398	bend N_1H , C_5H , (52)/str NC-CN+CC-CN (55)
1418	1411	1413	1413	1413	bend N_3H , N_1H , str N_1C_2 , N_3C_4 (54)
		1463			bend C_6H , N_1H , N_2H , C_5H , str C_4C_5 (54)
1479	1483	1483	1485	1487	str $\text{C}_6\text{N}_1-\text{C}_4\text{C}_5-\text{C}_2\text{O}_7$, bend N_1H , C_5H , C_6H (52)
1509	1513	1513	1513	1511	bend N_1H , str C_6N_1 (54)/ in-plane ring str (55)
1552	1552	1552	1552	1554	str $\text{C}_4\text{O}_8-\text{C}_5\text{C}_6-\text{C}_2\text{O}_7$, bend N_1H , C_6H , (53)
1599	1597	1595	1597	1597	str C_4O_8 , bend N_1H , C_6H (52)
	1623	1621	1623	1621	str $\text{C}_2\text{O}_7+\text{C}_5\text{C}_6$, bend N_1H , (52)

Abbreviations: str: stretching; bend: bending; def: deformation.

4.4.4 TERS spectra of calf thymus DNA – detection of all four DNA nucleobases and observation of a sequence change

To detect all four DNA nucleobases in an isolated strand, a single-stranded calf thymus DNA with all the four DNA nucleobases randomly distributed is used as sample for TERS measurement. Fig. 4.9 schematic shows the schematic chemical structure of a calf thymus DNA single strand and its immobilization on atomically flat mica surface. The mica surface is naturally negatively charged, the strands are also negatively charged because of the phosphate groups. Hence, multivalent cations (Mg^{2+} , Zn^{2+}) are used to change the mica charge and to fix the strands on the surface by electrostatic adsorption.

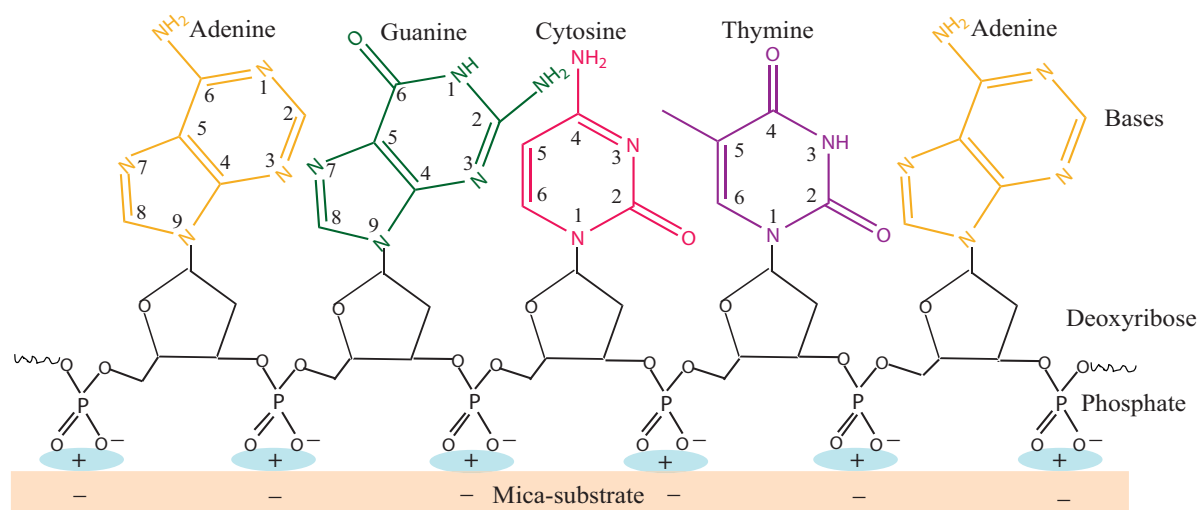


Fig. 4.9: Schematic chemical structure of the calf thymus DNA single strand and its immobilization on mica substrate. The numbering of the purine and pyrimidine rings is used for expressing the normal modes of vibrations.

TERS experiment is shown in fig. 4.10 and fig. 4.11. The AFM topography image shows a calf thymus DNA strand and the cross section in the inset indicates a height of approximately 1 nm. TERS spectra have been measured at 9 positions and an additional one for reference to exclude tip contamination. The TERS spectra were collected in three columns of three spectra each, while the distance in the strand extension direction between those in one column (1, 2, 3; 4, 5, 6; 7, 8, 9) is 0.3 nm. The distance between adjacent measurement positions in the respective columns (3, 6, 9; 2, 5, 8; 1, 4, 7) is 5.5 nm.

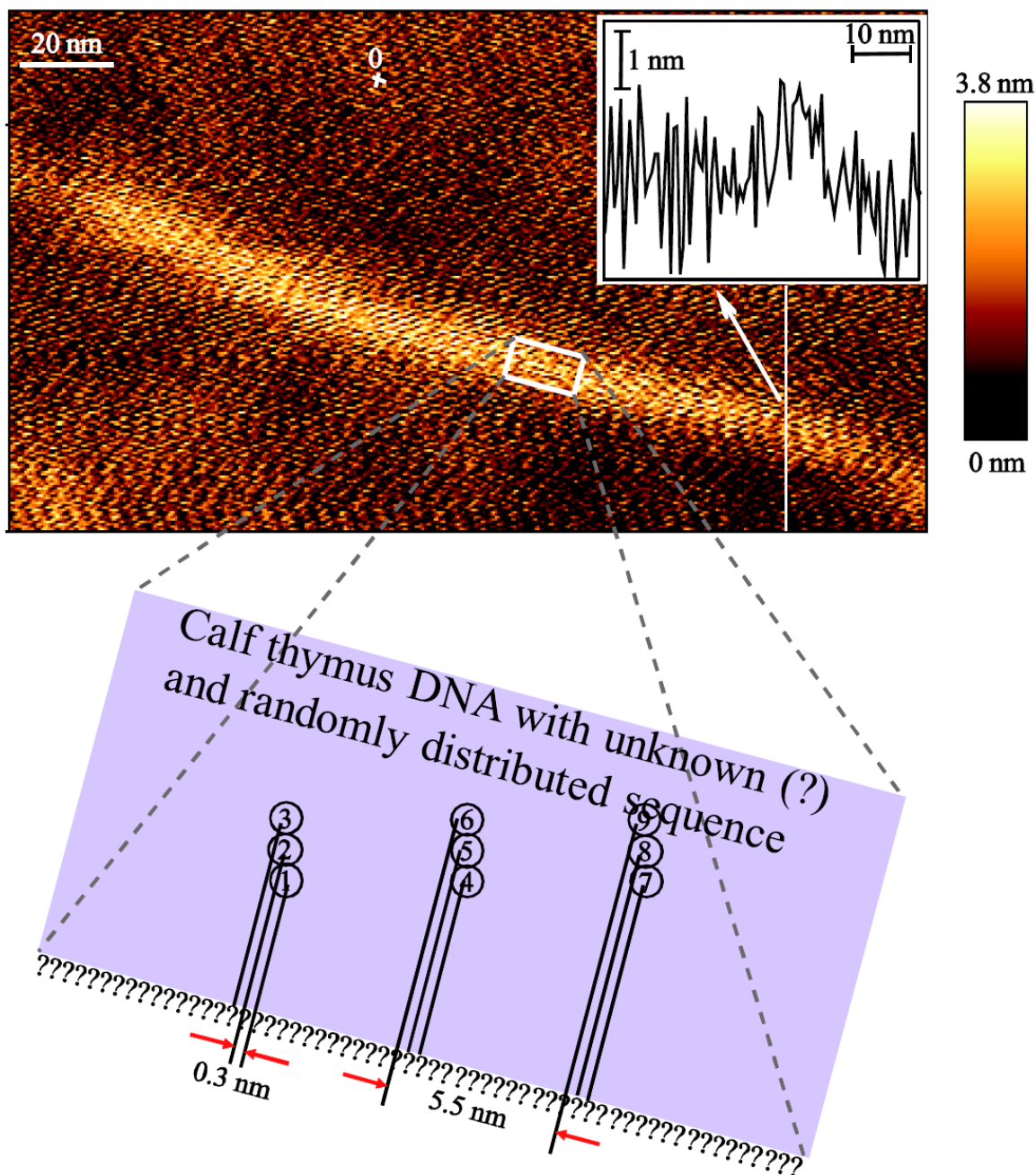


Fig. 4.10: AFM topography image of a calf thymus DNA single strand with a schematic depiction of the positions on which TERS spectra were collected, including one point next to the strand for reference. Inset shows a cross section over the strand.

Fig. 4.11 shows nine TERS spectra collected on the DNA single strand. A tentative assignment for most of the vibrational bands is given in table 4.4. While the spectra of the respective columns are similar, only one of each was selected for the respective band

Chapter 4

assignment. In the spectra the bands originating from the ring breathing modes of the different nucleobases are marked with different colors (adenine: 742 cm^{-1} , yellow; cytosine: 790 cm^{-1} , pink; guanine: 674 cm^{-1} , green; thymine: 809 cm^{-1} , purple). The characteristic vibrational bands from all four nucleobases can be identified in the single TERS spectra and no nucleobase prevails, which is different from the SERS results and predictions (11, 56) (see discussion in section 4.1.2.3). These results demonstrate again the possibility to detect all nucleobases in TERS spectra.

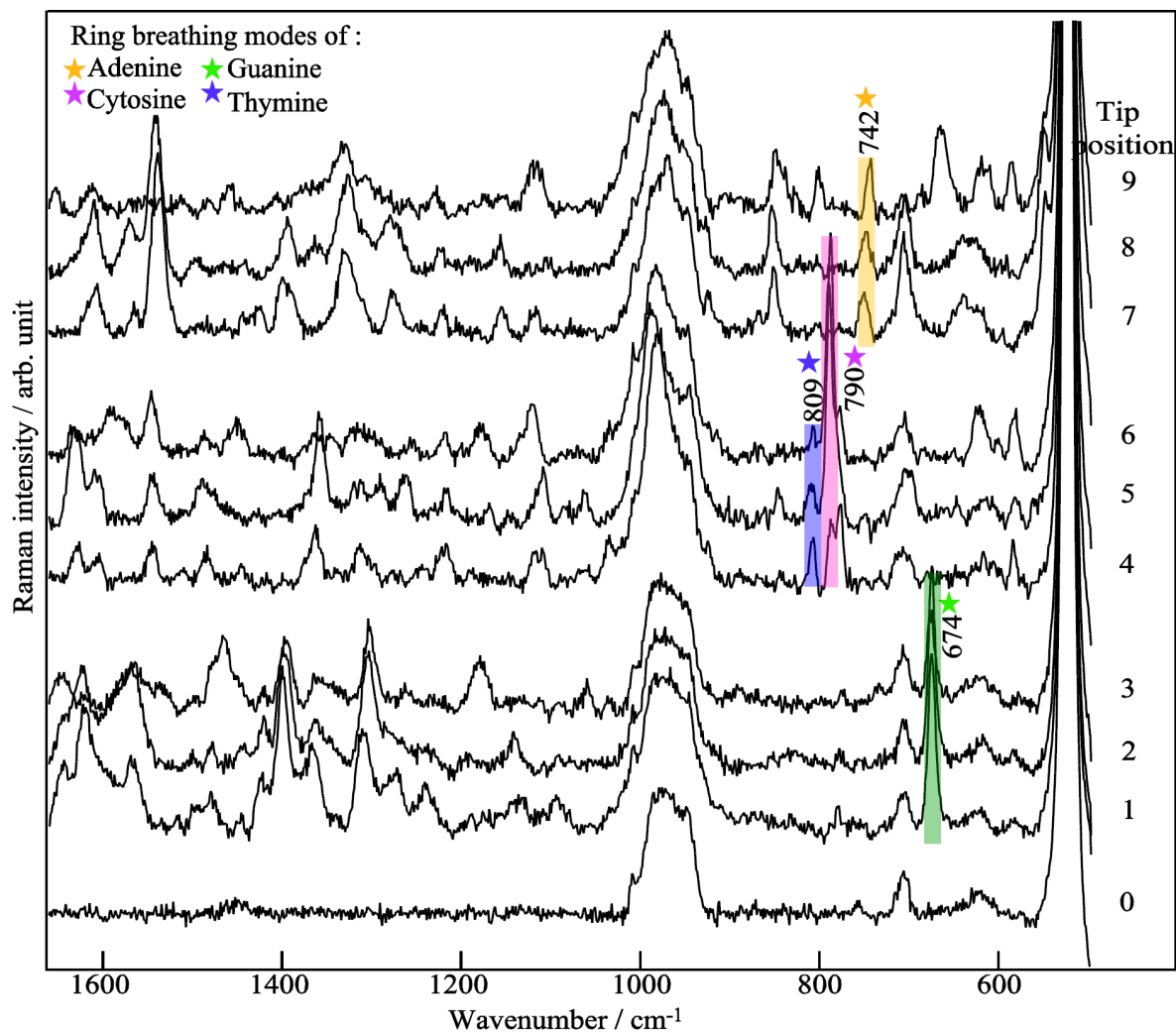


Fig. 4.11: TERS spectra. The spectra were measured on the 9 positions on a calf thymus DNA single strand indicated in fig. 4.10 and an additional position for reference (0). Bands marked with different colors represent the ring breathing modes from the different nucleobases.

Chapter 4

Comparing the spectra from different columns it is noticeable that they are strikingly different. This is not surprising, as the sequence of nucleobases underneath the TERS tip can be assumed to be different. With regard to a possible sequencing the spectra of the respective columns with a distance of 0.3 nm are of particular interest, because they were measured with even less than one base-to-base distance. As expected, within one column the changes between the spectra are small, because the content of nucleobases under the TERS tip almost remains alike. In the first column (spectra 1, 2, 3) the ring breathing mode of guanine is decreasing from position 1 to position 3, indicating guanine moving out of the enhancing region underneath the tip. In the second column (spectra 4, 5, 6) the ring breathing mode of thymine is decreasing from position 4 to position 6 while the ring breathing mode of cytosine is increasing from position 4 to position 6, which indicates the thymine moving out of the enhancing region underneath the tip while the cytosine move in. In the third column (7, 8, 9) the ring breathing mode of adenine increases when moving from position 7 to position 9, indicating a higher adenine content underneath the TERS tip. These spectra demonstrate the visibility of the sequence change in the TERS spectra when tip moved along the DNA stand, which can be attributed to the high lateral resolution of the TERS technique. This demonstrates one important prerequisite for the sequencing. However, the proposed reconstruction method in section 4.4.1 cannot be applied to deduce the partial sequence of the calf thymus DNA strand, because the number of acquired spectra was too small. Furthermore, the sequence of the used calf thymus DNA is random and unknown, hence it is impossible to compare the extracted sequence with the existed sequence even if the sequence could be deduced and reconstructed. As has been mentioned, the purpose of the measurement on calf thymus DNA is to demonstrate the feasibility of TERS on detection of all four DNA nucleobases in a strand and we have achieved it. In section 4.4.5, a single stranded DNA with known sequence will be used for further measurements.

Chapter 4

Table 4.4 Band assignment of the TERS spectra of a calf thymus DNA strand (cm^{-1}).

0	2	5	8	Tentative assignment
521	521	521	521	silicon (AFM tip)
		582		C (in-plane ring def) (55)
618	618	618	618	mica-substrate
	674			G (ring breathing (Im)) (8)
705	705	705	705	mica-substrate
		742	742	A (ring breathing (Py)) (8, 55)
	777	790		C (ring breathing (Py)) (8, 55)
		809		T (ring breathing (Py)) (8, 55)
		846	851	C, G (N-C-N str) (8)
		1061		A, N-sugar str (8, 46)
		1109		PO_2^- sym str (58) (46)
	1140	1145		A ($\text{C}_8\text{-N}_9$ str, $\text{N}_9\text{-H}$, $\text{C}_8\text{-H}$ def) (46, 55)
		1167	1156	A, G ($\text{C}_5\text{-C}_6$ str) (8, 46)
		1215	1224	C, T (In-plane ring- CH_3 str) (8, 46, 57)
		1262		A, C, G ($\text{C}_8\text{-N}_9$ str) T (ring str) (8, 46, 55, 58)
			1279	C(C-NH_2 str + ring str) (47, 55, 59)
		1291		C ($\text{C}_2\text{-N}_3$ str) (8, 28, 46)
	1303			A, G (C-N str (Im)) (8, 46)
			1325	A, G (ring mode) (60) (46)
	1360	1359	1363	A, C, G, T (C-N str (Py)) (8, 46)
	1396		1393	T (N-H def/ CH_3 def) (8, 46, 55)
	1419	1426		C ($\text{C}_4\text{-C}_5$ str)/A/T (8, 46, 55)
	1477			A (C=N str (Py)) (8, 46)
	1500	1489	1493	C, G (C=N str (Im)) (8, 46)
		1543	1540	A, T (in-plane ring str) (8, 46)

Chapter 4

	1564		1571	A, C, G, T (Ring str (Py)) (8, 46)
		1610	1610	A, C, G (NH ₂ def) (8, 46, 58)
	1621	1631		C, G, T (C=O str, C=C str) (8, 46, 61)

Abbreviations: Py: pyrimidine; Im: imidazole; str: stretching; def: deformation

4.4.5. TERS spectra of a (A₁₀C₁₅)₈ DNA single strand – distinction of adenine and cytosine nucleobases at sub-nanometer resolution and sequence reading information in the TERS spectra

To demonstrate the feasibility of TERS to distinguish different DNA nucleobases and to direct sequence DNA strands, a synthetic single-stranded DNA with a known repeating sequence unit of A₁₀C₁₅, that is (A₁₀C₁₅)₈, was used. The schematic chemical structure is shown in fig. 4.12. As has been mentioned in section 4.4.2, a homogeneous orientation of the strand on the substrate surface is crucial for successful TERS experiments. Firstly, the DNA strands must be single-stranded and fully stretched, which is a major challenge because single-stranded DNA preferably entangle or build secondary structures (62, 63). In the chosen compound this could be circumvented by the combination of adenine and cytosine, where no hydrogen bonds between complementary nucleobases can be formed. Secondly, a gentle thermal pretreatment of the strands (11) prior to their adsorption onto the surface was applied, yielding nearly completely stretched (A₁₀C₁₅)₈ single strands as shown in the AFM topography image in fig. 4.13 (a).

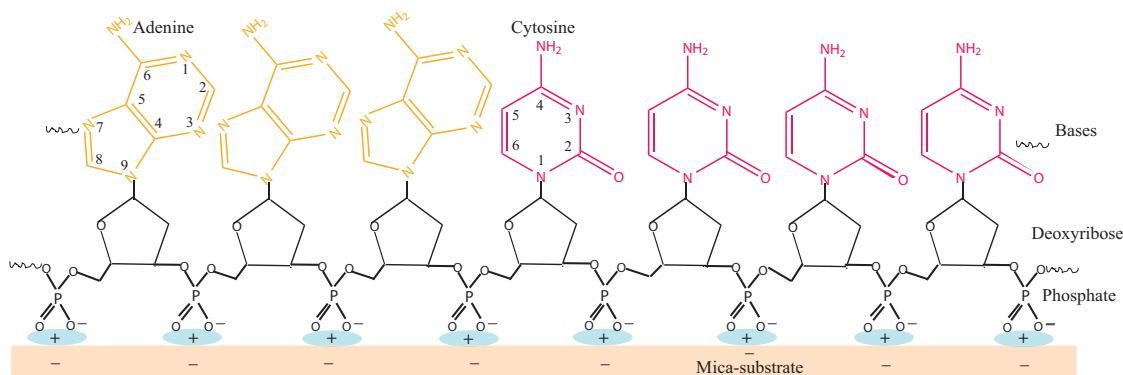


Fig. 4.12: Schematic chemical structure of the (A₁₀C₁₅)₈ DNA single strand and the numbering of the purine and pyrimidine rings.

Chapter 4

The topography of the DNA strand is shown with a height of about 0.45 nm in the profile image in fig. 4.13 (b) corresponds well with the known diameter of DNA single strands (13). In the present experiment the effective area probed by the TERS tip is a convolution of tip and sample features. Hence, the measured strand width of approximately 10 nm is due to the broadness of the silver-coated AFM tip and corresponds well with the tip diameter of <20 nm determined by SEM (see chapter 3 fig. 3.2 (a)). The length of the DNA chain is longer than expected and some small knot-like features in the strand indicate the joining of strands. However, these features had no impact on our further experiments as the actual experiments were limited to a short section (<10 nm, fig. 4.13 (a) and (c)) far away from these knots.

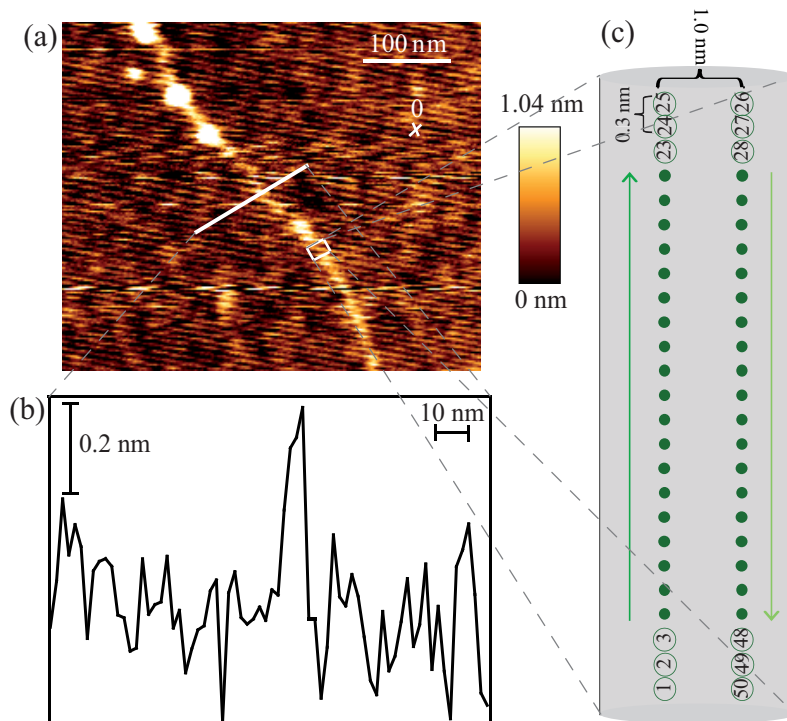


Fig. 4.13: TERS experiment on a $(A_{10}C_{15})_8$ DNA single strand. **(a)** AFM topography image of the investigated DNA single strand immobilized on atomic flat mica surface. **(b)** Height profile of the strand along the line indicated in (a). **(c)** Zoom in the region indicated in (a) where TERS spectra were measured along the DNA single strand trace and retrace (25 points separated by 0.3 nm on each of the two parallel lines, with a line-to-line distance of 1.0 nm).

Chapter 4

The actual TERS spectra were recorded on two parallel lines (trace and retrace were spaced by 1 nm) along the $(A_{10}C_{15})_8$ DNA single strand. Fig. 4.14 (a) shows 25 TERS spectra obtained along the trace on positions separated by 0.3 nm. At first glance the spectra show two types of significantly different spectral patterns with respect to the experimental position. Spectra at positions 1, 17-25 correspond to one pattern while spectra at positions 2-16 correspond to a second pattern. Spectra at positions 9-12 show no features, which is probably due to lost AFM feedback. This result already indicates by a mere pattern comparison and the a priori knowledge of the base spacing of 0.5-0.7 nm (7, 13), that spectra 2 – 16 correspond very likely to adenine. Strikingly the same grouping of patterns was found in the retrace spectra and even the onset of spectral changes coincides with the ones in the trace, hence, confirming the previous result and also indicating that no photo induced changes took place. The latter is a major concern due to the high field enhancement at the tip.

A detailed analysis of the spectra enabled the assignment of cytosine (red, with marker bands C1-C4) and adenine (orange, with marker bands A1-A4). For marker bands, it should be emphasized here that due to structural similarities of adenine and cytosine many bands can be detected in the same spectral area, but those bands were taken as marker bands, which were present exclusively in cytosine or adenine spectra. The molecular structure of adenine and cytosine are shown in fig. 4.12 and the complete spectral assignment is provided in table 4.5.

Regarding fig. 4.14 (a) it is surprising that no smooth transitions (spectra containing both adenine and cytosine modes to a similar extend) are detected while stepping from the adenine to the cytosine section but rather direct changes. This clearly demonstrates the capability of TERS to distinguish adenine and cytosine in the primary structure of a single molecule with sub-nanometre spatial resolution.

The estimation of the spatial resolution results was accomplished as follows. From fig. 4.14 (a) it is obvious that one cytosine spectrum (position 1) is followed by 15 subsequent

Chapter 4

adenine spectra (position 2 to 16), followed once more by eight cytosine spectra (position 17 to 25). It is exactly the sharp transition from cytosine to adenine and again to cytosine (C→ A→ C) underneath the TERS tip that leads to the estimation of the extremely high lateral resolution. Even if the second transition between position 16→17 is considered where one weak residual peak of cytosine or adenine, respectively, persist for two further positions (A2 is shown in cytosine spectra at position 17 and 18 while C4 is shown in adenine spectra at position 16 and 15) this relates to a change in definitely less than one nanometer. From the present experiment we estimated the resolution to be between 0.6 – 0.9 nm, which fits well with the recently reported atomic-scale confinement of resonant optical fields (atomic resolution) produced by two sub-nanometer neighbouring nanoparticles (64, 65), but is more noteworthy than most theoretical models of the field enhancement indicating a lateral resolution of 3-10 nm (47, 66) and even exceeding the recently reported experimental value of 2-3 nm (43-45). This result strongly indicates that additional enhancement effects based on interactions between tip and sample must be considered.

The 15 subsequent adenine spectra (position 2 to 16 in fig. 4.14 (a)) correspond to a length of about 4.5 nm on the strand. Assuming a base-to-base distance of between 0.5 nm to 0.7 nm (7, 13), 4.5 nm matches well the sequence of the investigated strand that contains 10 adenine nucleobases in a row. In case of cytosine only 10 spectra have been observed because the grid covered only a part (~ 6 bases) of the 15 cytosine bases.

The 25 spectra measured on the 1 nm separated parallel retrace (fig. 4.14 (b), position 26 to 50) show the same pattern as the trace spectra. Spectra at position 26-34, 50 in the retrace experiment show the same vibration modes as spectra at position 25-17, 1 and were assigned to cytosine while spectra at position 35-49 correspond to the spectra at position 16-2 and were assigned to adenine. Comparing the cytosine spectra of trace and retrace slight differences, mainly variations in the intensity ratios, were evident. These variations are related to the high lateral resolution of TERS and did not affect the data evaluation (29-31, 35). The most important issue was the fact that all four marker bands shown in the trace spectra of cytosine also appeared in the retrace spectra confirming the assignment. The

same observation was made for adenine and demonstrated the reproducibility of the experiment. Moreover, the retrace measurement proved the stability of the instrument (no drift of the strand).

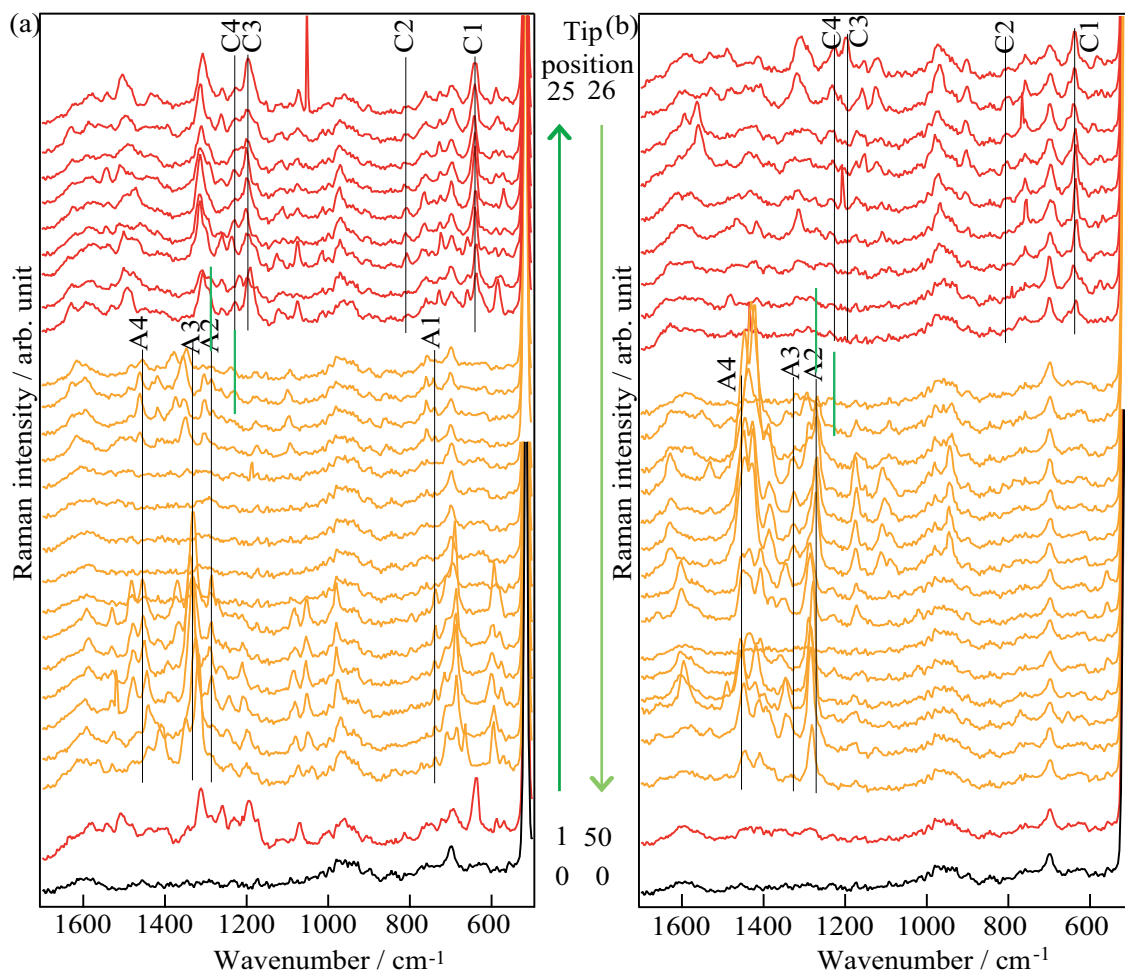
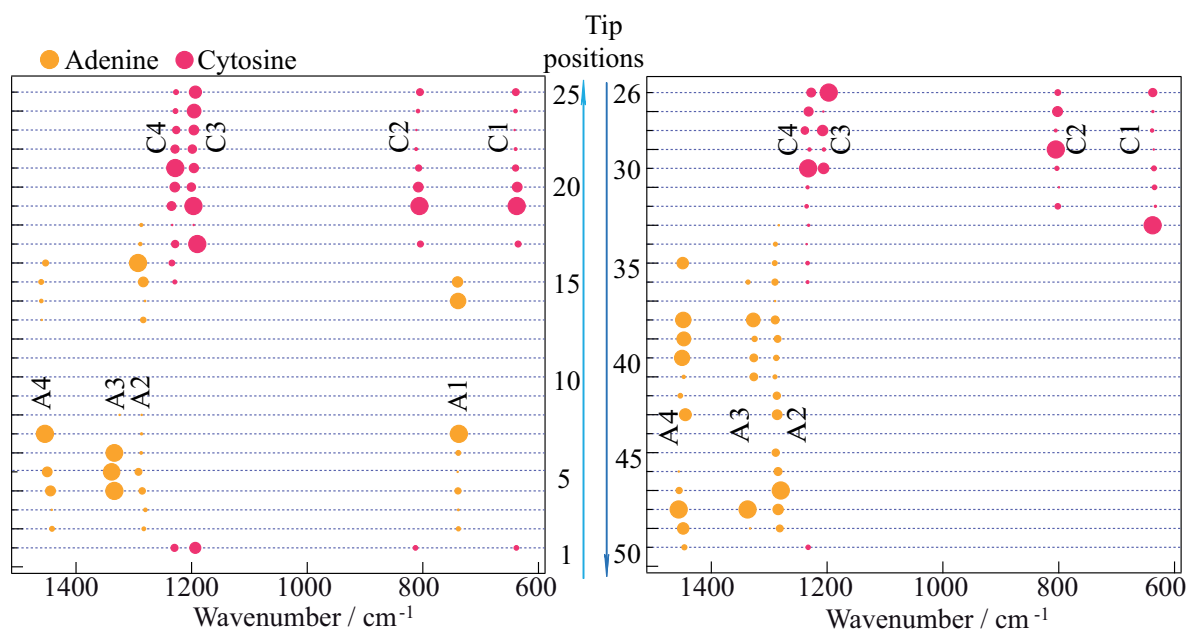


Fig. 4.14: TERS spectra measured at 50 positions along the $(A_{10}C_{15})_8$ DNA single strand trace and retrace as indicated in fig. 4.13 (c) and on an additional spot for reference (position 0 indicated in fig. 4.13 (a)).

To visualize the spectral changes in fig. 4.14 more clearly a different data presentation is provided in fig. 4.15. Here the marker bands of adenine (orange) and cytosine (red) versus the tip positions are shown as circles. The center of the circle corresponds to the spectral position and the size to the relative intensity. Both parameters were obtained by nonlinear curve fitting of the original spectra. This plot of the marker bands of adenine and cytosine vs. the tip positions illustrates again the sequence changing tendency of

Chapter 4

(C→A→C).



FigFig. 4.15: TERS signal intensity tracking of adenine and cytosine signals from the DNA single strand shown in fig. 4.14, orange (adenine), red (cytosine). The spot size is proportional to the signal intensity and normalized to each specific band.

Although the differences between adenine and cytosine in the spectra are striking, the spectra assigned to adenine or cytosine possesses similarities. Minor variations in band intensity ratios and positions could be found by careful observation, which were attributed to changes of the molecular orientation under the metal-coated tip or atomic site-selective interaction between the TERS tip and the DNA molecules and have been discussed in the literatures (29-31, 35). In adenine, for instance, any of the four nitrogen atoms: N1, N3, N7 and N10 could interact with the silver tip. On the other hand, N9 is the binding site to ribose and therefore cannot bind to the metal nanoparticle. Density functional theory (DFT) calculations show changes in Raman band intensities and positions for the four respective complexes of adenine and a silver atom. These variations were attributed to a deformation of the adenine molecules to an energetically optimized conformation. For the TERS experiments, although the backbone of the DNA single strand was immobilized and could not move freely, the molecules in the strand are not rigid. Furthermore, the molecules can interact with different metallic atoms located in the apex of the TERS tip, resulting in the

Chapter 4

electronic structural change of the molecules, which affects the internal vibrational modes of the molecules, especially if chemical interactions between the tip and the TERS probe take place.

From the presented results it could be concluded that the measurements on the trace and the parallel retrace along a DNA strand provided reproducibly sub-nanometer distinction of the two bases and furthermore sequence the DNA single strand, which opens the door of TERS for sequencing chain-like bio-macromolecules.

Table 4.5: Assignment of TERS spectra on a the (A₁₀C₁₅)₈ DNA single strand

Tip position	Tip position	Tip position	Tip position	Tentative assignment
2-16 Adenine	35-49 Adenine	1, 17-25 Cytosine	26-34, 50 Cytosine	
520	520	520	520	Si-tip
572				wag (C-H, N-H)(55)
		569	569	def C=O(67)
591		587	587	Ring def(68, 69)
		635	635	wag (N-H)(68)
650	650	650	650	Mica
680				Ring def(46, 70)
703	703	703	703	Mica
712				ring breath whole molecule (distorted)(69)
		720		? (32, 71)
737				Ring breathing(8, 55)
760	760	760	760	Mica
		806	806	Ring breathing (Py)(55, 8)
	945			(NH ₂ + C-H + ring) def(55)

Chapter 4

980	980	970	970	Deoxyribose(58)
		1012		Ring str + C-H def(55)
1051				N-sugar str(8) + sugar (CO str)(70)
1082	1082	1072		N-sugar str(8), bk (PO_2^- str)(70)
	1110	1110	1110	Deoxyribose(57)
1152	1152	1152	1152	Background
1172	1172	1172	1172	Background
		1196	1196	C-N str(67, 68)
1210				(C-N) str, (C-H, N-H) def(69)
		1231	1231	(C-N) str(67), all H def(68)
1244				(C-N) str, (N-H, C-H) def(55)
		1258		In-plane ring str,(C-H) def(55)
1282	1272, 1292			Ring(46, 70)
1302				Ring(70)
		1312	1312	(C-N, C=N) str(67)
1330	1330			(C-N) str(8)
1346	1346			$\text{N}_7\text{C}_5 + \text{C}_8\text{N}_7$ (72)
1370, 1383	1383			(C=N) str (Py)(8)
1407	1407			(C-N) str, C-H def(69)
1427	1427			(C-H, N-H) def + (C-N) str(55)
1450	1450			$\text{C}_2\text{H-N}_1\text{C}_2+\text{N}_3\text{C}_2$ (72)
				C=N str(46) (8)
1480	1480	1487	1487	Deoxyribose, Bk(58)
		1507		(NH_2) def(8)
1527	1527			Ring str(71)

Chapter 4

		1540	1559	Ring str (Py)(8, 46)
1596	1596	1596	1596	Ring str(70), NH ₂ def(8, 70)
1628	1628			NH ₂ sci(8, 46)
		1632	1632	(C=O) str(73)

Abbreviations: Py: pyrimidine; Im: imidazole; str: stretching; def: deformation; Wag: wagging

4.5 Conclusion and outlook

We have theoretically proposed label-free DNA sequencing using TERS and the necessary prerequisites. Furthermore, experimentally demonstrated the realization of these prerequisites therefore shows the potential of TERS for label-free DNA and other chain-like bio-macromolecules sequencing. Using this proof of concept procedure, further measurements will be performed on DNA strands containing all four nucleobases. The ultimate goal is the examination of strands with an unknown nucleobase order.

4.6 References

1. F. Sanger, S. Nicklen, A. R. Coulson, DNA Sequencing with Chain-Terminating Inhibitors. *Proc. Natl. Acad. Sci. U. S. A.* **74**, 5463 (1977).
2. E. S. Lander *et al.*, Initial sequencing and analysis of the human genome. *Nature* **409**, 860 (2001).
3. A. Meller, L. Nivon, E. Brandin, J. Golovchenko, D. Branton, Rapid nanopore discrimination between single polynucleotide molecules. *Proc. Natl. Acad. Sci. U. S. A.* **97**, 1079 (2000).
4. N. Ashkenasy, J. Sanchez-Quesada, H. Bayley, M. R. Ghadiri, Recognizing a single base in an individual DNA strand: A step toward DNA sequencing in nanopores. *Angewandte Chemie-International Edition* **44**, 1401 (2005).
5. D. Fologea *et al.*, Detecting single stranded DNA with a solid state nanopore. *Nano Letters* **5**, 1905 (2005).
6. T. Ohshiro, Y. Umezawa, Complementary base-pair-facilitated electron tunneling for electrically pinpointing complementary nucleobases. *Proc. Natl. Acad. Sci. U. S. A.* **103**, 10 (2006).
7. H. Tanaka, T. Kawai, Partial sequencing of a single DNA molecule with a scanning tunnelling microscope. *Nature Nanotechnology* **4**, 518 (2009).
8. N. H. Jang, The coordination chemistry of DNA nucleosides on gold nanoparticles as a probe by SERS. *Bulletin of the Korean Chemical Society* **23**, 1790 (2002).
9. D. Graham, B. J. Mallinder, D. Whitcombe, N. D. Watson, W. E. Smith, Simple multiplex genotyping by surface-enhanced resonance Raman scattering. *Analytical Chemistry* **74**, 1069 (2002).

Chapter 4

10. J. De Gelder, K. De Gussem, P. Vandenabeele, L. Moens, Reference database of Raman spectra of biological molecules. *Journal of Raman Spectroscopy* **38**, 1133 (2007).
11. A. Barhoumi, D. Zhang, F. Tam, N. J. Halas, Surface-enhanced Raman spectroscopy of DNA. *Journal of the American Chemical Society* **130**, 5523 (2008).
12. E. Papadopoulou, S. E. J. Bell, Label-Free Detection of Single-Base Mismatches in DNA by Surface-Enhanced Raman Spectroscopy. *Angewandte Chemie-International Edition* **50**, 9058 (2011).
13. Y. Maeda, T. Matsumoto, T. Kawai, Observation of single- and double-stranded DNA using non-contact atomic force microscopy. *Applied Surface Science* **140**, 400 (1999).
14. C. Hamai, H. Tanaka, T. Kawai, Extended structure of DNA oligomer and nucleotide imaging studied by scanning tunneling microscopy. *Journal of Physical Chemistry B* **104**, 9894 (2000).
15. M. Taniguchi, T. Kawai, DNA electronics. *Physica E-Low-Dimensional Systems & Nanostructures* **33**, 1 (2006).
16. M. Xu, D. Fujita, N. Hanagata, Perspectives and Challenges of Emerging Single-Molecule DNA Sequencing Technologies. *Small* **5**, 2638 (2009).
17. R. Treffer, V. Deckert, Recent advances in single-molecule sequencing. *Current Opinion in Biotechnology* **21**, 4 (2010).
18. N. Blow, DNA sequencing: generation next-next. *Nature Methods* **5**, 267 (Mar, 2008).
19. S. Howorka, Z. Siwy, Nanopore analytics: sensing of single molecules. *Chemical Society Reviews* **38**, 2360 (2009).
20. A. Aksimentiev, J. B. Heng, G. Timp, K. Schulten, Microscopic kinetics of DNA translocation through synthetic nanopores. *Biophysical Journal* **87**, 2086 (2004).
21. D. Branton *et al.*, The potential and challenges of nanopore sequencing. *Nature Biotechnology* **26**, 1146 (2008).
22. R. Ebright, Q. P. Dong, J. Messing, Corrected Nucleotide-Sequence of M13mp18 Gene Iii. *Gene* **114**, 81 (1992).
23. S. Meng, P. Maragakis, C. Papaloukas, E. Kaxiras, DNA nucleoside interaction and identification with carbon nanotubes. *Nano Letters* **7**, 45 (2007).
24. K. Faulds, W. E. Smith, D. Graham, Evaluation of surface-enhanced resonance Raman scattering for quantitative DNA analysis. *Analytical Chemistry* **76**, 412 (2004).
25. M. B. Wabuyele, T. Vo-Dinh, Detection of human immunodeficiency virus type 1 DNA sequence using plasmonics nanopores. *Analytical Chemistry* **77**, 7810 (2005).
26. V. Brabec, K. Niki, Raman-Scattering from Nucleic-Acids Adsorbed at a Silver Electrode. *Biophysical Chemistry* **23**, 63 (1985).
27. L. A. Gearheart, H. J. Ploehn, C. J. Murphy, Oligonucleotide adsorption to gold nanoparticles: A surface-enhanced raman spectroscopy study of intrinsically bent DNA. *Journal of Physical Chemistry B* **105**, 12609 (2001).
28. M. Green, F. M. Liu, L. Cohen, P. Kollensperger, T. Cass, SERS platforms for high density DNA arrays. *Faraday Discussions* **132**, 269 (2006).
29. H. Watanabe, Y. Ishida, N. Hayazawa, Y. Inouye, S. Kawata, Tip-enhanced near-field Raman analysis of tip-pressurized adenine molecule. *Physical Review B* **69**, (2004).
30. N. Hayazawa, H. Watanabe, Y. Saito, S. Kawata, Towards atomic site-selective sensitivity in tip-enhanced Raman spectroscopy. *Journal of Chemical Physics* **125**, (2006).
31. T. Ichimura *et al.*, Temporal fluctuation of tip-enhanced Raman spectra of adenine molecules. *Journal of Physical Chemistry C* **111**, 9460 (2007).
32. A. Rasmussen, V. Deckert, Surface- and tip-enhanced Raman scattering of DNA components. *Journal of Raman Spectroscopy* **37**, 311 (2006).
33. K. F. Domke, D. Zhang, B. Pettinger, Tip-enhanced Raman spectra of picomole quantities of DNA nucleobases at Au(111). *Journal of the American Chemical Society* **129**, 6708 (2007).

Chapter 4

34. D. Zhang, K. F. Domke, B. Pettinger, Tip-Enhanced Raman Spectroscopic Studies of the Hydrogen Bonding between Adenine and Thymine Adsorbed on Au (111). *Chemphyschem* **11**, 1662 (2010).
35. E. Bailo, V. Deckert, Tip-enhanced Raman spectroscopy of single RNA strands: Towards a novel direct-sequencing method. *Angewandte Chemie-International Edition* **47**, 1658 (2008).
36. R. Levicky, T. M. Herne, M. J. Tarlov, S. K. Satija, Using self-assembly to control the structure of DNA monolayers on gold: A neutron reflectivity study. *Journal of the American Chemical Society* **120**, 9787 (1998).
37. L. K. Wolf, Y. Gao, R. M. Georgiadis, Sequence-dependent DNA immobilization: Specific versus nonspecific contributions. *Langmuir* **20**, 3357 (2004).
38. T. Deckert-Gaudig, V. Deckert, Ultraflat Transparent Gold Nanoplates - Ideal Substrates for Tip-enhanced Raman Scattering Experiments. *Small* **5**, 432 (2009).
39. H. G. Hansma, I. Revenko, K. Kim, D. E. Laney, Atomic force microscopy of long and short double-stranded, single-stranded and triple-stranded nucleic acids. *Nucleic Acids Research* **24**, 713 (1996).
40. C. C. Neacsu, J. Dreyer, N. Behr, M. B. Raschke, Scanning-probe Raman spectroscopy with single-molecule sensitivity. *Physical Review B* **73**, (2006).
41. J. Steidtner, B. Pettinger, Tip-enhanced Raman spectroscopy and microscopy on single dye molecules with 15 nm resolution. *Physical Review Letters* **100**, (2008).
42. W. Zhang, B. S. Yeo, T. Schmid, R. Zenobi, Single molecule tip-enhanced Raman spectroscopy with silver tips. *Journal of Physical Chemistry C* **111**, 1733 (2007).
43. T. Deckert-Gaudig, E. Kaemmer, V. Deckert, Tracking of nanoscale structural variations on a single amyloid fibril with tip-enhanced Raman scattering. *Journal of Biophotonics* **5**, 215 (2012).
44. T. Ichimura *et al.*, Subnanometric Near-Field Raman Investigation in the Vicinity of a Metallic Nanostructure. *Physical Review Letters* **102**, (2009).
45. T. Yano, P. Verma, Y. Saito, T. Ichimura, S. Kawata, Pressure-assisted tip-enhanced Raman imaging at a resolution of a few nanometres. *Nature Photonics* **3**, 473 (2009).
46. R. Treffer, X. M. Lin, E. Bailo, T. Deckert-Gaudig, V. Deckert, Distinction of nucleobases – a tip-enhanced Raman approach. *Beilstein Journal of Nanotechnology* **2**, 628 (2011).
47. Z. Yang, J. Aizpurua, H. Xu, Electromagnetic field enhancement in TERS configurations. *Journal of Raman Spectroscopy* **40**, 1343 (2009).
48. M. Futamata, Y. Maruyama, M. Ishikawa, Local electric field and scattering cross section of Ag nanoparticles under surface plasmon resonance by finite difference time domain method. *Journal of Physical Chemistry B* **107**, 7607 (2003).
49. T. Deckert-Gaudig, F. Erver, V. Deckert, Transparent Silver Microcrystals: Synthesis and Application for Nanoscale Analysis. *Langmuir* **25**, 6032 (2009).
50. T. Deckert-Gaudig, E. Bailo, V. Deckert, Perspectives for spatially resolved molecular spectroscopy - Raman on the nanometer scale. *Journal of Biophotonics* **1**, 377 (2008).
51. T. Deckert-Gaudig, E. Rauls, V. Deckert, Aromatic Amino Acid Monolayers Sandwiched between Gold and Silver: A Combined Tip-Enhanced Raman and Theoretical Approach. *Journal of Physical Chemistry C* **114**, 7412 (2009).
52. K. H. Cho, J. Choo, S. W. Joo, Surface-enhanced Raman scattering and density functional theory calculation of uracil on gold and silver nanoparticle surfaces. *Spectrochimica Acta Part a-Molecular and Biomolecular Spectroscopy* **61**, 1141 (2005).
53. Z.-B. Lin *et al.*, Potential-dependent adsorption of uracil on a silver electrode in alkaline solutions. *Journal of Electroanalytical Chemistry* **636**, 74 (2009).
54. B. Giese, D. McNaughton, Surface-enhanced Raman spectroscopic study of uracil. The influence of the surface substrate, surface potential, and pH. *Journal of Physical Chemistry B* **106**, 1461 (2002).

Chapter 4

55. Y. Badr, M. A. Mahmoud, Effect of silver nanowires on the surface-enhanced Raman spectra (SERS) of the RNA bases. *Spectrochimica Acta Part a-Molecular and Biomolecular Spectroscopy* **63**, 639 (2006).
56. B.-S. Yeo, J. Stadler, T. Schmid, R. Zenobi, W. Zhang, Tip-enhanced Raman Spectroscopy - Its status, challenges and future directions. *Chemical Physics Letters* **472**, 1 (2009).
57. R. Y. Zhang *et al.*, Investigation of ordered ds-DNA monolayers on gold electrodes. *Journal of Physical Chemistry B* **106**, 11233 (2002).
58. W. H. Ke, D. F. Zhou, J. Z. Wu, K. Ji, Surface-enhanced Raman spectra of calf thymus DNA adsorbed on concentrated silver colloid. *Applied Spectroscopy* **59**, 418 (2005).
59. L. E. Hennemann, A. J. Meixner, D. Zhang, Surface- and tip-enhanced Raman spectroscopy of DNA. *Spectroscopy* **24**, 119 (2010).
60. G. J. Thomas Jr *et al.*, Polarized Raman spectra of oriented fibers of A DNA and B DNA: anisotropic and isotropic local Raman tensors of base and backbone vibrations. *Biophysical Journal* **68**, 1073 (1995).
61. R. Escobar, P. Carmona, M. Molina, Raman spectroscopic determination of thymidine nucleoside structures in nucleotides. *Analyst* **121**, 105 (1996).
62. X. Michalet, Stretching single-stranded DNA on a surface. *Nano Letters* **1**, 341 (Jul, 2001).
63. J. Adamcik, D. V. Klinov, G. Witz, S. K. Sekatskii, G. Dietler, Observation of single-stranded DNA on mica and highly oriented pyrolytic graphite by atomic force microscopy. *Febs Letters* **580**, 5671 (2006).
64. R. Esteban, A. G. Borisov, P. Nordlander, J. Aizpurua, Bridging quantum and classical plasmonics with a quantum-corrected model. *Nature Communications* **3**, 825 (2012).
65. J. Kern *et al.*, Atomic-Scale Confinement of Resonant Optical Fields. *Nano Letters* **12**, 5504 (2012).
66. A. Downes, D. Salter, A. Elfick, Finite element simulations of tip-enhanced Raman and fluorescence spectroscopy. *Journal of Physical Chemistry B* **110**, 6692 (2006).
67. L. E. Camafeita, S. Sanchezcortes, J. V. Garciamoros, Sers of Cytosine and Its Methylated Derivatives on Gold Sols. *Journal of Raman Spectroscopy* **26**, 149 (1995).
68. K. H. Cho, and Joo. S. W., Tautomerism of Cytosine on Silver, Gold, and Copper: Raman Spectroscopy and Density Functional Theory Calculation Study. *Bull. Korean Chem. Soc.* **29**, 69 (2008).
69. B. Giese, D. McNaughton, Surface-enhanced Raman spectroscopic and density functional theory study of adenine adsorption to silver surfaces. *Journal of Physical Chemistry B* **106**, 101 (2002).
70. L. Movileanu, J. M. Benevides, G. J. Thomas, Temperature dependence of the Raman spectrum of DNA. Part I - Raman signatures of premelting and melting transitions of poly(dA-dT)center dot poly(dA-dT). *Journal of Raman Spectroscopy* **30**, 637 (1999).
71. L. Lafleur, J. Rice, G. J. Thomas, Raman Studies of Nucleic-Acids .7. Poly Poly-a-Poly-U U and Poly Poly-G-Poly-C C. *Biopolymers* **11**, 2423 (1972).
72. C. Otto, T. J. J. Vandentweel, F. F. M. Demul, J. Greve, Surface-Enhanced Raman-Spectroscopy of DNA Bases. *Journal of Raman Spectroscopy* **17**, 289 (1986).
73. J. Florian, V. Baumruk, J. Leszczynski, IR and Raman spectra, tautomeric stabilities, and scaled quantum mechanical force fields of protonated cytosine. *Journal of Physical Chemistry* **100**, 5578 (1996).

Chapter 5: TERS for the direct detection of 5-methylcytosine sites on DNA strands

5.1 The aim of this chapter

DNA methylation is known to alter gene expression and is believed to result in deleterious phenotypic changes, such as cancer. The detection of DNA methylation sites on DNA strands is therefore important for clinical diagnostics and therapy. Typical biological methods for DNA methylation detection require pre-treatment or conversion of the sample with chemical which may induce additional chemical modifications in the DNA. For SERS, a special pre-treatment and conversion of the sample is not required, but because of the limited spatial resolution, the obtained spectra only show an average methylation level across many DNA molecules on the strands. Therefore, it is impossible to detect the specific methylation sites on the DNA strands. Taking advantage of the high spatial resolution, high spectral specificity and sensitivity of TERS, the aim of work in this chapter is to directly detect the 5-methylcytosine sites on DNA single strands.

5.2 Introduction: epigenetics and DNA methylation

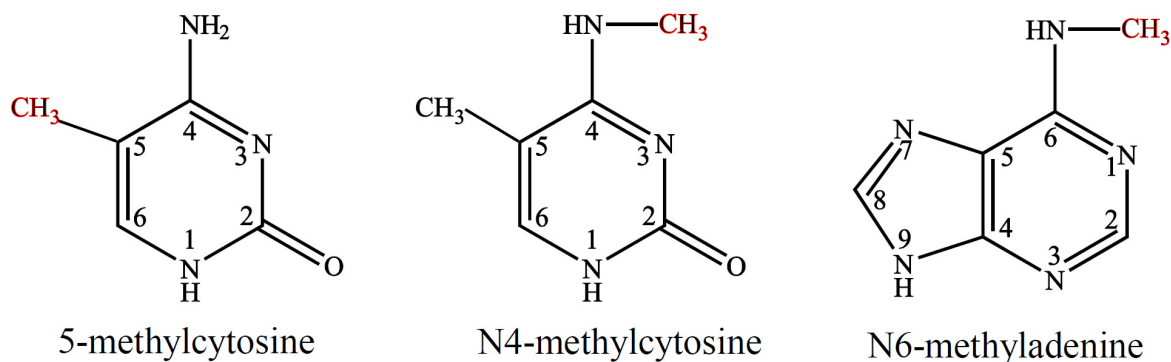


Fig. 5.1: Methylation of DNA cytosine and adenine residues.

The phenotype of a cell is determined by its inherited genotype, transmitted epigenetic factors, and non-hereditary environmental variation. Epigenetics is the study of changes in gene activity that do not involve alterations to the genetic code but still get passed down to at least one successive generation. Epigenetics provides stability and diversity to the cellular phenotype through chromatin marks that affect local transcriptional potential and that are preserved or regenerated during cell division (1). One example of epigenetics is

Chapter 5

DNA methylation, which involves the addition of a methyl group to the adenine or cytosine nucleobases, as shown in fig. 5.1. In mammals and plants, the methyl group is only added to the 5th position of the cytosine (5-methylcytosine, 5meC). Bacteria and archaea also have 5meC, along with N-4-methylcytosine and N-6-methyladenine (*1*).

5-methylcytosine in cytosine–phosphate–guanosine dinucleotides (CpGs) (fig. 5.2) is the most abundant and most intensively studied epigenetic marker in many eukaryotes. CpGs are also called CpG islands, which are short sections including 200 to 500 base-pairs of DNA with a higher frequency of CpG dinucleotides relative to the bulk genome. CpG islands are typically found in or near promoter regions of genes, where transcription is initiated. Cytosine in CpG islands are generally unmethylated in promoter regions to express the gene (fig. 5.2 (a)), in contrast, the gene expression is inhibited if the cytosine in CpGs are methylated. DNA methylation has been shown to correlate strongly with cancer in humans. In cancer cells, hypermethylation (fig. 5.2 (b)) within promoters serves to turn off critical tumor-suppress genes, results in their expression silence (*2, 3*).

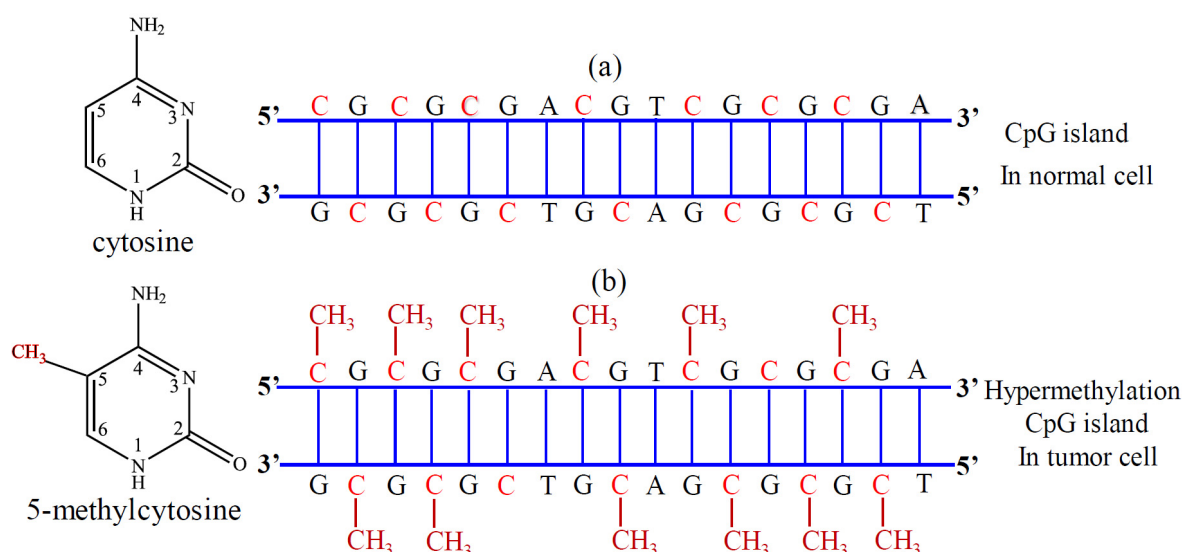


Fig. 5.2: CpG islands in or near promoter regions of genes (a) in a normal cell; (b) in a tumor cell, where the cytosine nucleobases are hypermethylated.

Typical biological methods for detecting DNA methylation sites include bisulphate conversion, endonuclease digestion, and affinity enrichment. Their principles and challenges are thoroughly discussed in the reference (*4*). All these methods require

Chapter 5

multiple-step sample preparation with chemicals that may induce additional chemical modifications in the DNA or interfere with the detection of modified DNA.

SERS has been used for methylated DNA studies as well because no chemical treatments of samples are needed, which eliminates the interaction of DNA with other chemicals, minimizing unwanted chemical modification due to sample preparation. Sanchez-Cortes and Garcia-Ramos (5, 6) reported the SERS study of cytosine and its methylated derivatives on metal colloids. SERS spectra of cytosine, 1-methylcytosine, 5-methylcytosine and 1, 5-dimethylcytosine on gold, silver and copper colloids were reported. They observed that the methyl groups induced some changes in the π -electron system of the pyrimidine ring that affected the orientation and the adsorbate-metal interaction. These interactions also depended on the metal and on the pH of the solution and resulted in the differences of spectra of cytosine vs its methylated derivatives.

Barhoumi et al. (7) also reported the detection of methylated DNA bases using SERS. In their results, depending on the sample was normal DNA, cytosine methylated (5meC) DNA, or the mixture of normal and cytosine methylated DNA, the intensity of band at 786 cm^{-1} (cytosine ring breathing mode) slightly changed and were detectable. This was considered to be a marker for cytosine methylation. However, the slight intensity change of the ring breathing mode of cytosine could also be caused by the inhomogeneous enhancement of the substrate or different adsorption orientation of the DNA to the substrate. The results and explanation would be more convincing if some bands directly related to the CH_3 group could be detected in the SERS spectra.

Hobro, A. J., et al. also used SERS to study normal and methylated ribonucleosides. But their experiments concentrated more on the effect of different aggregating agents (8).

Chapter 5

5.3 Materials and method

5.3.1 Materials

Single-stranded methylated DNA $(A_{10}5meC_{10})_4$ was purchased at Eurogentec Deutschland GmbH. All the other chemicals used for buffer solutions and DNA immobilization on mica were purchased either at Sigma-Aldrich or VWR international.

5.3.2 Sample preparation and TERS measurements

The immobilization procedure of $(A_{10}5meC_{10})_4$ methylated DNA single strands on mica surface followed the procedure of $(A_{10}C_{15})_8$ as described in chapter 4. The TERS measurements on methylated DNA sample were performed on setup 2, using 320 μW laser power on the sample and an acquisition time of 2s.

5.4 Results and discussion

Fig. 5.3 schematically shows the chemical structure of the $(A_{10}5meC_{10})_4$ methylated DNA single strand. Similar to TERS measurements on normal DNA strands, TERS measurements on the methylated sample were performed by immobilizing the $(A_{10}5meC_{10})_4$ DNA single strands on a mica surface and then positioning an Ag-coated tip along the strand to detect the 5-methylcytosine sites and investigate the sequence information.

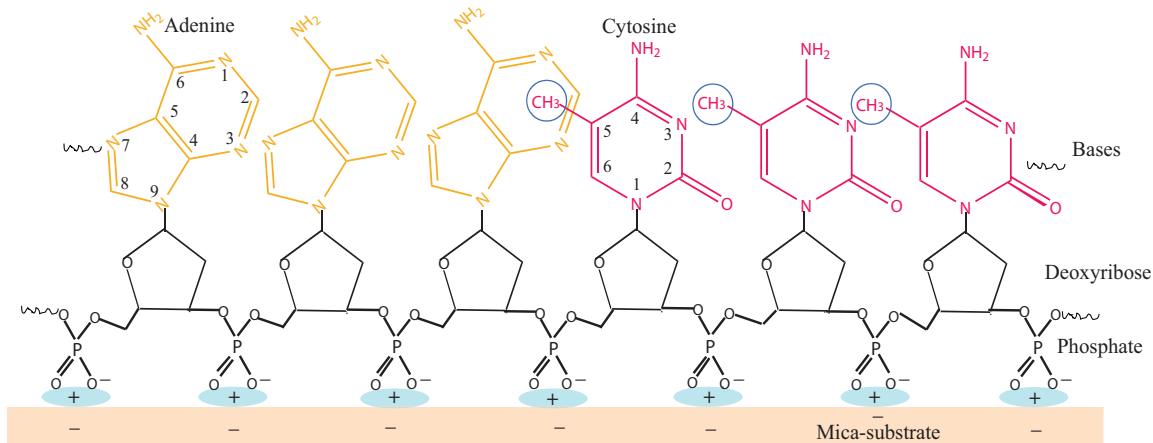


Fig. 5.3: Chemical structure of the $(A_{10}5meC_{10})_4$ methylated DNA single strand and the numbering of the purine and pyrimidine rings used for expressing the normal modes of vibrations.

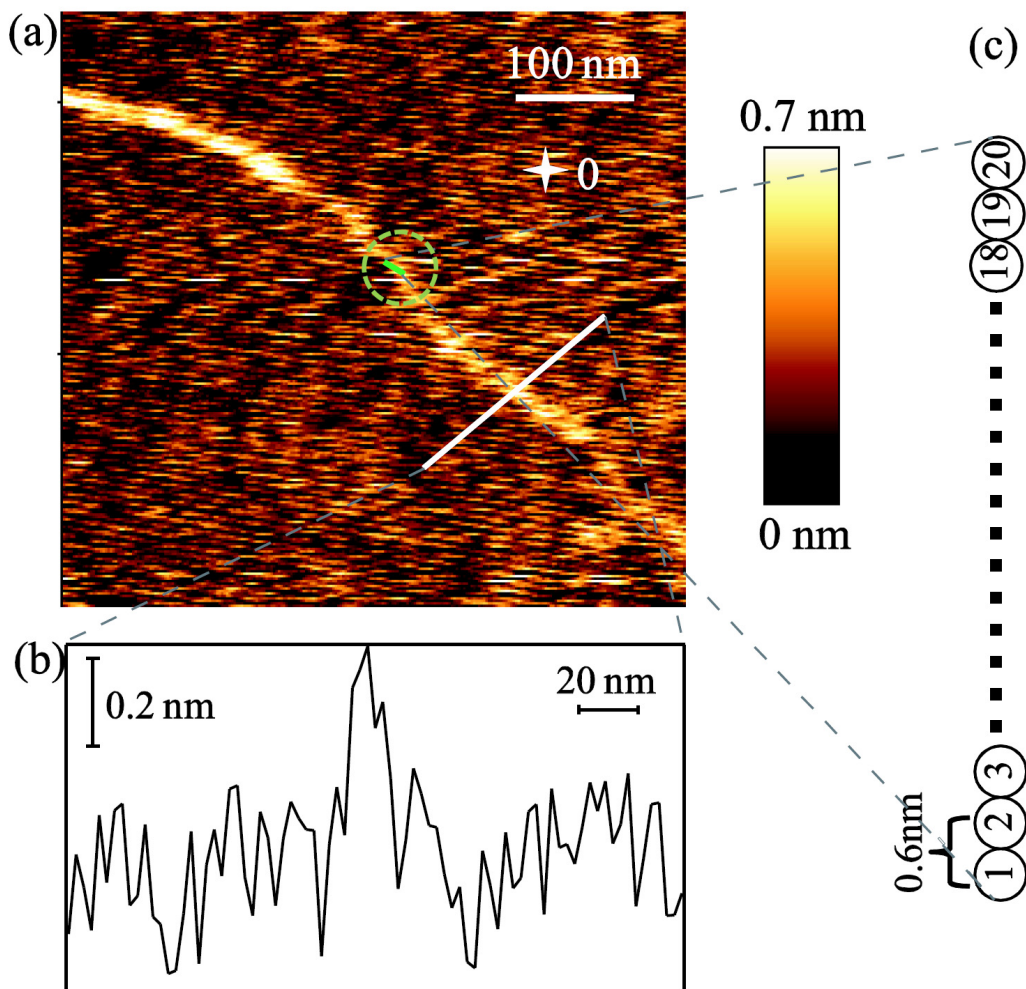


Fig. 5.4: TERS experiment on a $(A_{10}5meC_{10})_4$ DNA single strand. **(a)** AFM topography image of the investigated methylated DNA strand immobilized on a mica surface. **(b)** Height profile of the strand along the line indicated in (a). **(c)** The zoom in region indicated in (a) (green line in the green circle) where TERS spectra were measured along the DNA single strand on 20 positions with a step-size of 0.6 nm

Fig. 5.4 (a) shows the AFM topography of the measured DNA strand with the length of ~ 500 nm, again is longer than expected (80 bases, 0.5-0.7 nm of base-to-base distance, means ~ 40 nm – 56 nm in length) and some small knot-like features in the strand indicate the joining of strands. However, the TERS spectra were recorded on a short section (~ 12 nm) on the strand, which are not affected by those features. The height profile (fig. 5.4 (b)) through the strand along the line indicated in (a) supports the identification of a single strand. By comparing the morphology of normal DNA (chapter 4) and methylated DNA

Chapter 5

(this chapter) strands, no differences could be observed. Therefore, it is impossible to distinct them by morphology.

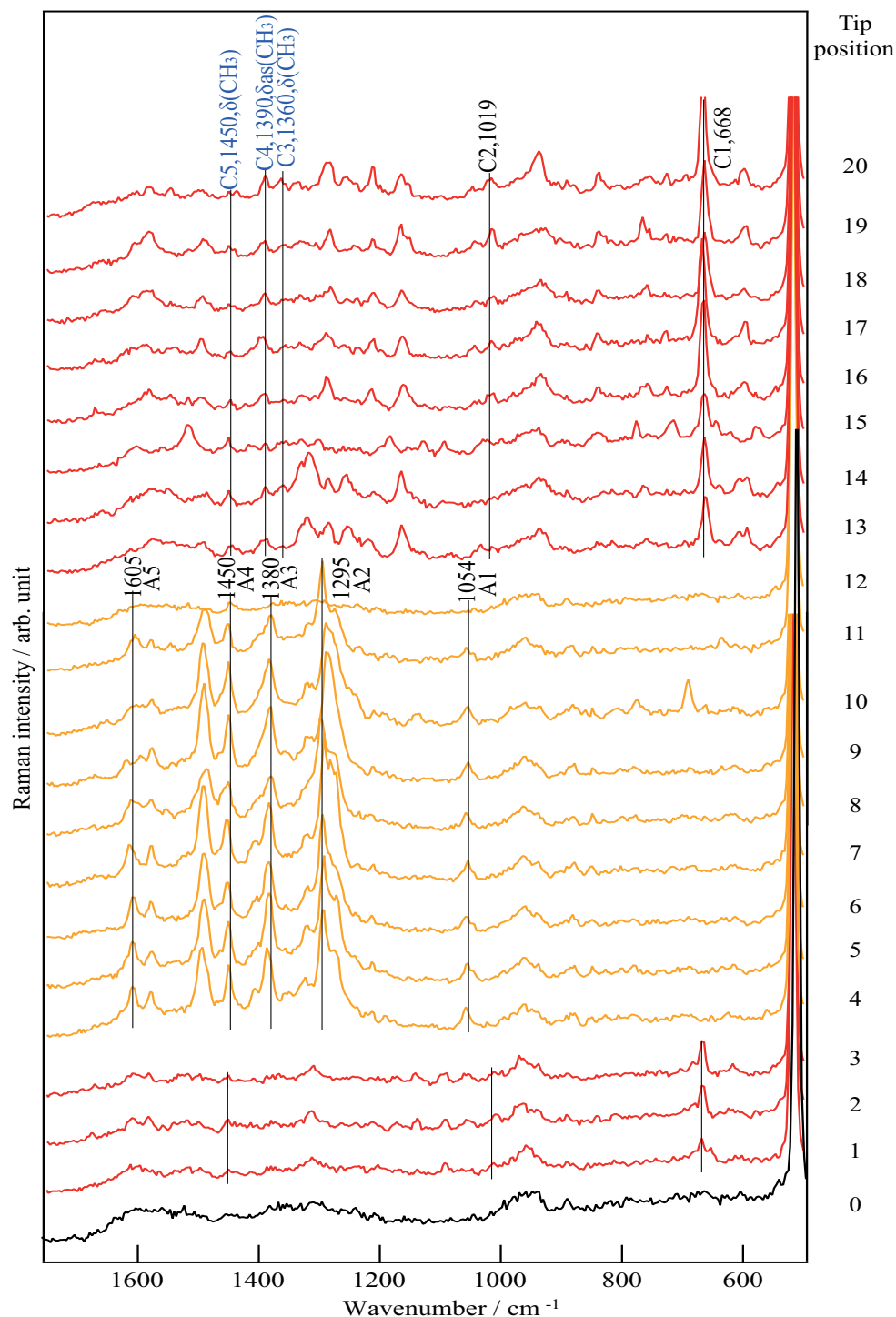


Fig. 5.5: TERS spectra recorded along a $(A_{10}5meC_{10})_4$ methylated DNA single strand with a step-size of 0.6 nm (position 1 to 20 indicated in fig. 5.4 (c)), and a reference

Chapter 5

measurement (position 0 indicated in fig. 5.4 (a)). Orange: adenine, red: 5-methylcytosine, the bands marked with blue color related to the methylation.

TERS spectra were recorded along the single strand on 20 positions with a distance of 0.6 nm (close to the base-to-base distance, fig. 5.4 (c)) and one additional spot away from the strand for the reference measurement (position 0) indicated in fig. 5.4(a), which are shown in fig. 5.5. From the 20 raw spectra, important information can be extracted: 1). Similar to TERS spectra of $(A_{10}C_{15})_8$, the TERS spectra of $(A_{10}5meC_{10})_4$ show two strikingly different types of vibrational modes. These patterns can be assigned to adenine (orange, position 4-12) with distinct marker bands of A1-A5 (A1: 1054 cm^{-1} , N-sugar str+sugar (CO str); A2: 1295 cm^{-1} , ring; A3: 1380 cm^{-1} , C=N str; A4: 1450 cm^{-1} , $C_2H-N_1C_2+N_3C_2$; A5: 1605 cm^{-1} , Ring str, NH_2 def) (6, 9-16) and 5-methylcytosine (red, position 1-3, 13-20) with distinct marker bands of C1-C5 (C1: 668 cm^{-1} , wag N-H; C2: 1019 cm^{-1} , Ring str+C-H def; C3: 1360 cm^{-1} , CH_3 , def, symmetric; C4: 1390 cm^{-1} , CH_3 , def, asymmetric; C5: 1450 cm^{-1} , CH_3 def) (6, 9-16). The 20 spectra show the sequence changing tendency of:

(5meC \rightarrow A \rightarrow 5meC). The sharp transition between the two different vibrational modes leads to the estimation of the lateral resolution again of less than one nanometer. 2). The base-to-base distance extracted from the adenine spectra is 0.54 nm, which is close to the distance extracted from the $(A_{10}C_{15})_8$ TERS spectra ($\sim 0.50\text{ nm}$) and still in the range of reported DNA base-to-base distance (17-19). 3). The spectra show a specific methylation signal namely the CH_3 symmetric deformation band at 1360 cm^{-1} , asymmetric deformation band at 1390 cm^{-1} , and CH_3 deformation band at 1450 cm^{-1} (C3-C5, marked with blue color on the spectra).

Table 5.1 shows the assignment of the $(A_{10}5meC_{10})_4$ TERS spectra and the comparison to the previously measured $(A_{10}C_{15})_8$. It can be easily seen from the assignment table that the TERS spectra of adenine are similar. All the bands found in the methylated strand can be also found in the normal strand. However, TERS spectra of cytosine and 5-methylcytosine are different because of the methylation at the 5th position, especially for the bands resulting from the CH_3 group. Fig.5.6 is the comparison of averaged TERS spectra between cytosine (20 spectra, from $(A_{10}C_{15})_8$ strand) and 5-methylcytosine (11 spectra, from $(A_{10}5meC_{10})_4$

Chapter 5

strand), which clearly shows the distinct bands at 1360 cm^{-1} , 1390 cm^{-1} and 1450 cm^{-1} resulting from the methylation and indicate the direct detection a of 5-methylcytosine sites on DNA strands by TERS.

Similar to the TERS spectra of normal DNA strands, spectral fluctuations are observed in the spectra, which are inherent with this technology because of its extreme sensitivity and the subtle molecular changes that occur at nanometer resolution (20, 21) and have been discussed in chapter 4.

Table 5.1: Assignment of TERS spectra on the $(A_{10}5meC_{10})_4$ methylated DNA single strand and the comparison of TERS spectra of normal DNA stand and methylated DNA strand.

$A_{10}C_{15}$ adenine	$A_{10}5meC_{10}$ adenine	$A_{10}C_{15}$ cytosine	$A_{10}5meC_{10}$ 5me-cytosine	Tentative assignment
520	520	520	520	Si-tip
572				wag (C-H, N-H) (9)
		569		def C=O (6)
591		587	598	Ring def (10) (11)
		635	668	wag (N-H) (6, 8, 10)
683	690			Ring def (12) (13)
712				ring breath whole molecule (distorted) (11)
		720	720	? (14, 15)
737				Ring breathing (12) (13) (16)
		806		Ring breathing (Py) (10)
			838	NH ₂ , rocking (6)
980		970	938	Deoxyribose (22)
		1012	1019	Ring str + C-H def (9)
1051	1054			N-sugar str (16) + sugar (CO str) (12, 13)
1082		1072	1093	N-sugar str (16), bk (PO ₂ ⁻ str) (12) (13) (22)

Chapter 5

1110		1110		Deoxyribose (23)
			1165	Deoxyribose-phosphate (22)
		1196		C-N str (6, 10)
1210			1213	(C-N) str (6), (C-H, N-H) def (11)
		1231		(C-N) st (6), all H def (10)
1244				(C-N) str, (C-H, N-H) def (9)
		1258	1255	in-plane ring str, (C-H) def (9)
1282	1275 1295			ring (12, 13)
1302				ring (13)
		1312	1319	(C-N, C=N) str (6)
1330	1320			(C-N) str (16)
1346				$N_7C_5 + C_8N_7$ (24)
			1360	CH ₃ , def, symmetric (6)
			1390	CH ₃ , def, asymmetric (6)
1370 1383	1380			(C=N) str (Py) (16)
1407				(C-N) str, C-H def (11)
1427				(C-H, N-H) def + (C-N) str (9)
1450	1450			$C_2H-N_1C_2+N_3C_2$ (24)
			1450	CH ₃ def (6)
1480	1490	1487	1487	Deoxyribose, bk (22)
		1507	1517	(NH ₂) def (16)
1527				Ring str (14)
		1559	1579	Ring str (Py) (16, 12)
1596	1605	1596		Ring str(13), NH ₂ def (13, 16)
1628				NH ₂ sci (12) (16)
		1632		(C=O) str (25)

Chapter 5

Abbreviations: Py: pyrimidine; Im: imidazole; str: stretching; def: deformation; Wag: wagging

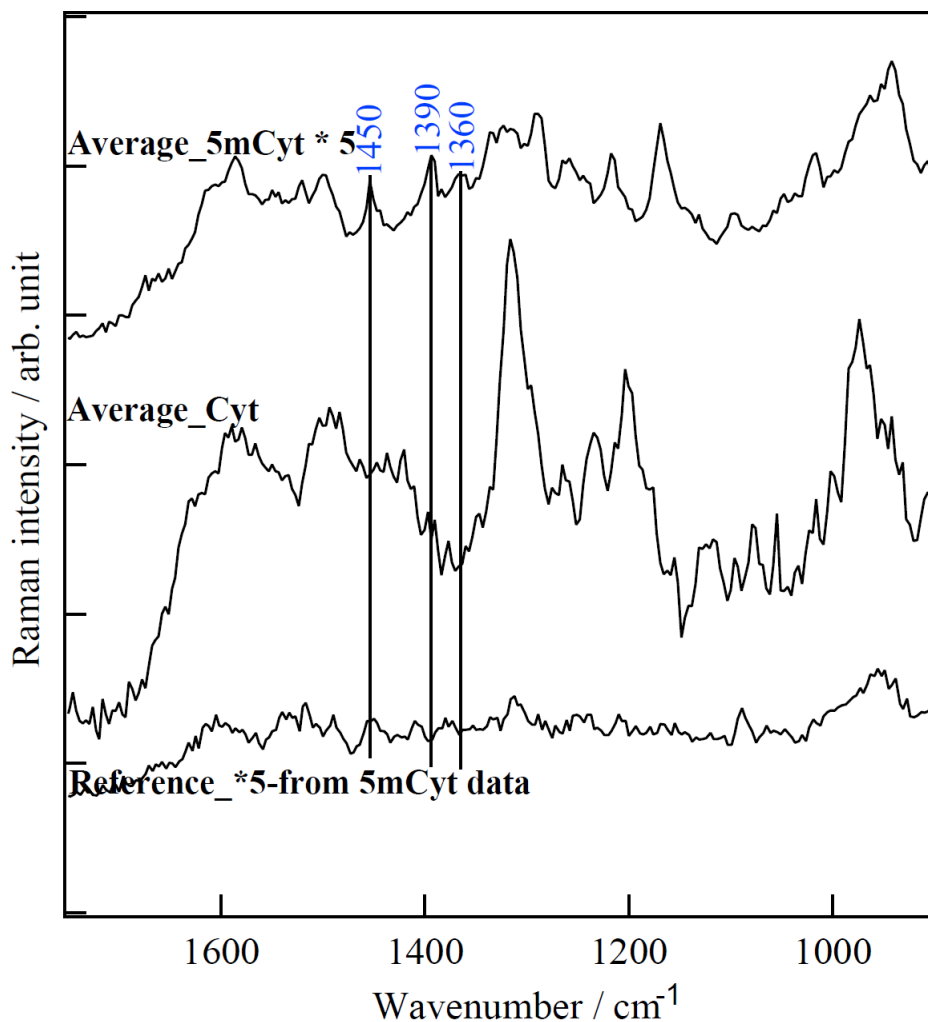


Fig. 5.6: The comparison of averaged TERS spectra between cytosine (20 spectra, from (A₁₀C₁₅)₈ strand) and 5-metnylcytosine (11 spectra, from (A₁₀5meC₁₀)₄ strand). The bands at 1360 cm⁻¹ (CH₃ symmetric deformation), 1390 cm⁻¹ (CH₃ asymmetric deformation) and 1450 cm⁻¹ (CH₃ deformation) resulting from the methylation demonstrate the direct detection of methylation sites on DNA stands.

5.5 Conclusion and outlook

In conclusion, the measured TERS spectra from (A₁₀5meC₁₀)₄ on one hand demonstrates the direct detection of 5-metnylcytosine sites on methylated DNA single strands; on the other hand, further demonstrates that TERS can be used for biopolymer direct sequencing

Chapter 5

at sub-nanometer resolution. Using this proof of concept procedure, more measurements will be performed to identify other types of methylation (N-4-methylcytosine and N-6-methyladenine) and to localize their specific positions on the strands, providing a possible step forward to clinical diagnostic and therapy.

5.6 References

1. A. C. Ferguson-Smith, J. M. Greally, R. A. Martienssen, Epigenomics. *Springer* (2008).
2. S. B. Baylin, DNA methylation and gene silencing in cancer. *Nature clinical practice. Oncology* **2** Suppl 1, S4 (2005).
3. K. D. Robertson, A. P. Wolffe, DNA methylation in health and disease. *Nature Reviews Genetics* **1**, 11 (2000).
4. P. W. Laird, Principles and challenges of genome-wide DNA methylation analysis. *Nature Reviews Genetics* **11**, 191 (2010).
5. S. Sanchez-Cortes, J. V. Garcia-Ramos, SERS of cytosine and its methylated derivatives on metal colloids. *Journal of Raman Spectroscopy* **23**, 61 (1992).
6. L. E. Camafeita, S. Sanchez-Cortes, J. V. Garcia-Ramos, SERS of cytosine and its methylated derivatives on gold sols. *Journal of Raman Spectroscopy* **26**, 149 (1995).
7. A. Barhoumi, N. J. Halas, Detecting chemically modified DNA bases using Surface-enhanced Raman spectroscopy. *Journal of Physical Chemistry Letters* **2**, 3118 (2011).
8. A. J. Hobro, S. Abdali, E. W. Blanch, SERS study of methylated and nonmethylated ribonucleosides and the effect of aggregating agents. *Journal of Raman Spectroscopy* **43**, 187 (2012).
9. Y. Badr, M. A. Mahmoud, Effect of silver nanowires on the Surface-enhanced Raman spectra (SERS) of the RNA bases. *Spectrochimica Acta Part a-Molecular and Biomolecular Spectroscopy* **63**, 639 (2006).
10. K.-H. Cho, S.-W. Joo, Tautomerism of cytosine on silver, gold, and copper: Raman spectroscopy and density functional theory calculation study. *Bulletin of the Korean Chemical Society* **29**, 69 (2008).
11. B. Giese, D. McNaughton, Surface-enhanced Raman spectroscopic and density functional theory study of adenine adsorption to silver surfaces. *Journal of Physical Chemistry B* **106**, 101 (2002).
12. R. Treffer, X. Lin, E. Bailo, T. Deckert-Gaudig, V. Deckert, Distinction of nucleobases - a tip-enhanced Raman approach. *Beilstein Journal of Nanotechnology* **2**, 628 (2011).
13. L. Movileanu, J. M. Benevides, G. J. Thomas, Temperature dependence of the Raman spectrum of DNA. Part I - Raman signatures of premelting and melting transitions of poly(dA-dT)center dot poly(dA-dT). *Journal of Raman Spectroscopy* **30**, 637 (1999).
14. L. Lafleur, J. Rice, G. J. Thomas, Raman Studies of Nucleic-Acids VII . Poly A . PolyU . Poly G . Poly C. *Biopolymers* **11**, 2423 (1972).
15. A. Rasmussen, V. Deckert, Surface- and tip-enhanced Raman scattering of DNA components. *Journal of Raman Spectroscopy* **37**, 311 (2006).
16. N. H. Jang, The coordination chemistry of DNA nucleosides on gold nanoparticles as a probe by SERS. *Bulletin of the Korean Chemical Society* **23**, 1790 (2002).
17. Y. Maeda, T. Matsumoto, T. Kawai, Observation of single- and double-stranded DNA using non-contact atomic force microscopy. *Applied Surface Science* **140**, 400 (1999).
18. C. Hamai, H. Tanaka, T. Kawai, Extended structure of DNA oligomer and nucleotide imaging studied by scanning tunneling microscopy. *Journal of Physical Chemistry B* **104**, 9894 (2000).

Chapter 5

19. M. Taniguchi, T. Kawai, DNA electronics. *Physica E-Low-Dimensional Systems & Nanostructures* **33**, 1 (2006).
20. T. Ichimura *et al.*, Temporal fluctuation of tip-enhanced Raman spectra of adenine molecules. *Journal of Physical Chemistry C* **111**, 9460 (2007).
21. H. Watanabe, Y. Ishida, N. Hayazawa, Y. Inouye, S. Kawata, Tip-enhanced near-field Raman analysis of tip-pressurized adenine molecule. *Physical Review B* **69**, 155418 (2004).
22. W. H. Ke, D. F. Zhou, J. Z. Wu, K. Ji, Surface-enhanced Raman spectra of calf thymus DNA adsorbed on concentrated silver colloid. *Applied Spectroscopy* **59**, 418 (2005).
23. R. Y. Zhang *et al.*, Investigation of ordered ds-DNA monolayers on gold electrodes. *Journal of Physical Chemistry B* **106**, 11233 (2002).
24. C. Otto, T. J. J. Vandenweel, F. F. M. Demul, J. Greve, Surface-enhanced Raman-spectroscopy of DNA bases. *Journal of Raman Spectroscopy* **17**, 289 (1986).
25. J. Florian, V. Baumruk, J. Leszczynski, IR and Raman spectra, tautomeric stabilities, and scaled quantum mechanical force fields of protonated cytosine. *Journal of Physical Chemistry* **100**, 5578 (1996).

Chapter 6: AFM-TERS investigations on skin penetration of invasomes

6.1 The aim of this chapter

Raman and IR have been used in the study of interactions of liposome vesicles with skin and have provided important information at the spatial resolution of a few hundred nanometers (1-3). However the size of the liposome vesicles is usually about 50 to 200 nm in diameter, which is smaller than the spatial resolution Raman and IR can achieve. This disadvantage can be overcome by TERS. The topography imaging capability of AFM provides the morphology of control and liposomes treated skin sample with nanometer spatial resolution, which shows the physical state changes in both the exogenous (liposomes) and endogenous (stratum corneum, SC) components. The spectroscopic capability of TERS can be used to identify the changes at molecular level. Furthermore, combining TERS with the “tape-stripping” skin sample preparation method (technique which removes sequential layers of SC), the depth and maybe kinetics of liposomal penetration through the SC could be monitored. Therefore, the aim of this study is to investigate and visualize the interaction between flexible liposomal systems (invasomes) and human skin (main SC) by AFM and TERS. Outcome of this study could help to understand the underlying mechanism of skin penetration of invasomes systems.

6.2 Introduction

6.2.1 Skin barrier and penetration pathway

Skin is the largest organ of the human body, which forms a barrier between the body and environment and has a surface area between 1.5 and 2.0 m². Skin is anatomically divided into three principal and distinct layers, stratum corneum (SC), viable epidermis, and dermis respectively, see fig. 6.1. A fatty subcutaneous layer resides beneath the dermis.

The stratum corneum is the top layer of the skin and varies in thickness from approximately ten to several hundred micrometres, depending on the region of the body (4). The most simplistic organizational model of SC is the classic “brick-and-mortar” assembly (5). This structure is analogous to a wall where corneocytes (brick, because of the cornified envelope around each corneocyte) are embedded in a complex lamellar lipid domain or matrix (mortar) formed of complex mixtures of cholesterol, free fatty acids, and ceramides

Chapter 6

(fig.6.2). Corneocytes are typically 200-300 nm thick, 30-50 μm in diameter and polygonal in shape. The barrier nature of the SC is governed by its constituents: 75%-80% are proteins, 5%-15% lipids, and so far 5%-10% unidentified components. (6).

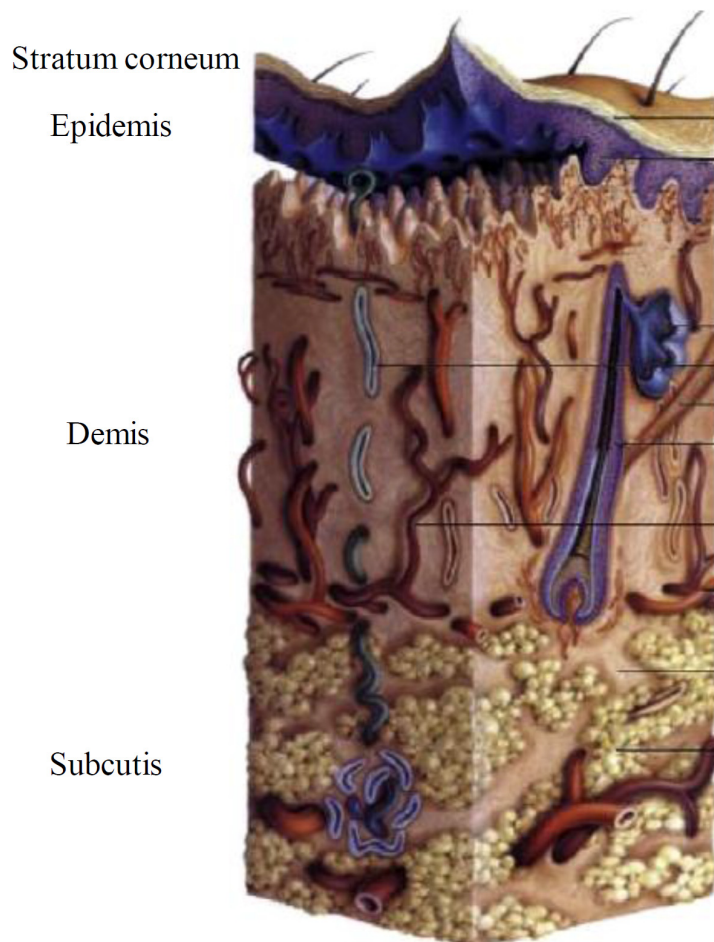


Fig. 6.1: Schematic image of skin structure with different layers: stratum corneum (SC), epidermis, and dermis. The subcutis layer is beneath the skin, adapted from (7).

The stratum corneum provides the most significant barrier to diffusion. In fact, the stratum corneum is the barrier to approximately 90% of transdermal drug applications. However, nearly all molecules penetrate it to some minimal degree (8). Below the stratum corneum lies the viable epidermis. This layer is about ten times as thick as the stratum corneum; however, diffusion is much faster here due to the greater degree of hydration in the living cells of the viable epidermis. Below the epidermis lies the dermis, which is approximately one millimeter thick, 100 times the thickness of the stratum corneum. The dermis contains

Chapter 6

small vessels that distribute drugs into the systemic circulation and to regulate temperature, a system known as the skin's microcirculation (8, 9).

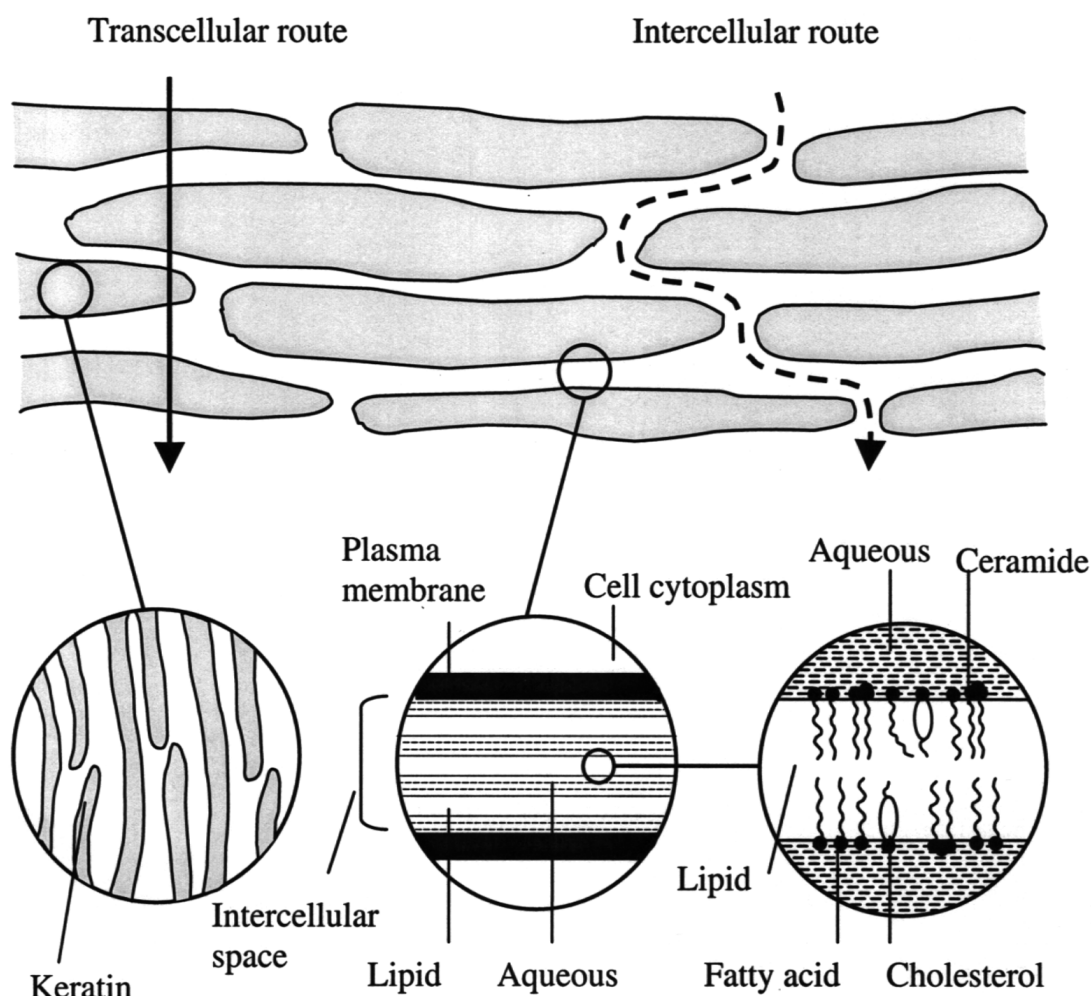


Fig. 6.2: “Brick-and-Mortar” model of stratum corneum (SC) and two main penetration pathways (transcellular route and intercellular route) for drugs crossing the skin and reach the systemic circulation, adapted from (10).

There are two main pathways by which drugs can cross the skin and reach the systemic circulation, see fig. 6.2. The more direct route is known as the transcellular pathway. By this route, drugs cross the skin by directly passing through both the phospholipids membranes and the cytoplasm of the dead keratinocytes that constitute the stratum corneum. Although this is the path of shortest distance, the drugs encounter significant resistance to permeation. This is because the drugs must cross the lipophilic membrane of each cell, then

Chapter 6

the hydrophilic cellular contents containing keratin, and then the phospholipid bilayer of the cell one more time. This series of steps is repeated numerous times to traverse the full thickness of the stratum corneum (4, 8).

The other pathway through the skin is via the intercellular route. Drugs crossing the skin by this route must pass through the small spaces between the cells of the skin, making the route more tortuous. Although the thickness of the stratum corneum is only about 20 μm , the actual diffusional path of most molecules crossing the skin is on the order of 400 μm (11). The 20-fold increase in the actual path of permeating molecules greatly reduces the rate of drug penetration (9).

6.2.2 Liposomes as tools for the skin drug delivery

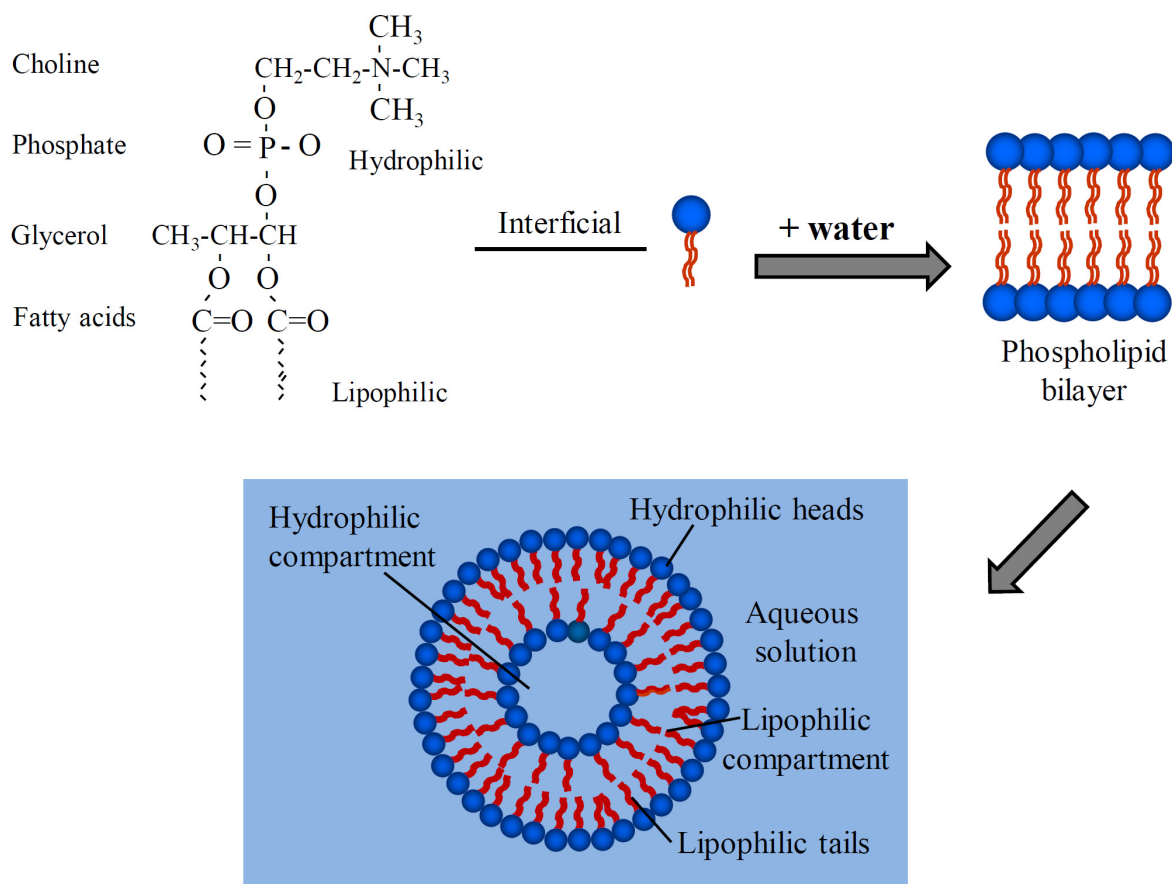


Fig. 6.3: Top left structural formula of the phosphatidylcholine molecule. In the presence of water phospholipid bilayers are formed, which create vesicles, enclosing an aqueous core.

Chapter 6

Lipid soluble substances can be stored in the outer lipid phase (red ring) and water soluble substances in the inner aqueous phase (blue centre) adapted from(12).

From a pharmaceutical point of view, skin offers a promising route for delivering drugs because skin drug delivery brings forth many attractive advantages over other routes of administration: avoidance of first-pass metabolism, lower fluctuations in plasma drug levels, good patient compliance and so on (13). On the other hand, the skin is also a tough barrier for delivering drugs, which is 10^2 - 10^4 times less permeable than a blood capillary wall (14) and imposes physicochemical limitations to the type of permeants which can traverse it.

Over the past decades, numerous studies have been performed to overcome the problems associated with skin delivery and also a number of novel skin delivery systems and approaches have been developed, including the use of chemical penetration enhancers (15, 16), optimization of physic-chemical properties of the drug (17), the application of liposomes and other colloidal drug carrier systems, and others (18). Among these novel techniques, lipid vesicular systems such as liposomes, offer a promising strategy for successfully improving skin drug delivery.

Liposomal vesicles are colloidal vesicles in which one or more lipid bilayers entrap an aqueous volume. Their major components are usually phospholipids, with or without some additives. There are a wide variety of lipids and additives that can be used to prepare these vesicles. Phospholipids have the ability to spontaneously rearrange and form bilayer sheets after addition of water. These bilayer sheets then further aggregate into vesicular structure, which results from their amphipathic character due to the presence of a polar or hydrophilic (water-attracting) head-group region and a non-polar, lipophilic (water-repellent) tail. The hydrophilic head groups orientate toward the aqueous phase and the lipophilic tails orientate to each other in the presence of water (fig. 6.3) (18, 19). Therefore, liposomes contain a lipophilic environment within the bi-layer membranes and hydrophilic environment between the membranes. Correspondingly, lipophilic drugs could be incorporated into the bilayers; while the hydrophilic one could be loaded within the water

Chapter 6

phase inside the vesicles and could be also found outside the liposomes in high amounts (20).

Liposomes can be classified according to their particle size. Small unilamellar vesicles (SUV) have dimensions of 20 up to about 50 nm. Large unilamellar vesicles (LUV) are between 50 and 500 nm, and multilamellar vesicles (MLV) have dimensions exceeding 500 nm but below 10,000 nm in diameter. SUVs are less suitable for drug delivery because they lack stability and their volume is too small for entrapping drugs. And generally, the penetration of liposomes through the stratum corneum decreases with increasing diameters. Therefore, the preferred structures for drug delivery are liposomes that are 50–500 nm in diameter (12).

Liposomes also can be classified according to their components, which could be conventional liposomes and flexible liposomes. Conventional liposomes are mostly composed of phospholipids, with or without cholesterol. Flexible liposomal systems include invasomes, ethosomes, transferosomes etc. Invasomes are composed of phosphatidylcholine, ethanol, a mixture of terpenes as penetration enhancers, and additional edge activators such as surfactants and lysophosphatidylcholine (LPC) to modify the bilayer elasticity and to increase deformability (21).

Because of their elasticity and deformability, invasomes show better penetration capabilities compared with conventional liposomal systems. There are two possible mechanisms responsible for its enhanced skin drug delivery. First, invasomes may act as drug carrier systems by which intact vesicles can enter the SC carrying vesicle-bound drug into or across the skin. Second, invasomes may act as penetration enhancers, whereby the vesicle lipid bilayers interact with the SC and subsequently modify the intercellular lipid lamellae and finally adsorb to and/or fuse with the SC. It may also be possible that one of the two mechanisms might predominate according to the physicochemical properties of the drug considered (22).

Chapter 6

6.3 Materials and methods

6.3.1 Materials:

1-palmitoyl-2-oleoyl-sn-glycero-3-phosphocholine (POPC, 16:0-18:1 PC)

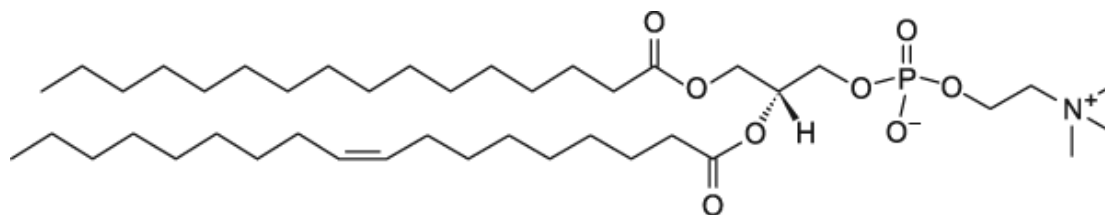


Fig. 6.4: Structure of POPC

1-oleoyl-2-hydroxy-sn-glycero-3-phosphocholine (LPC, 18:1 Lyso-PC)

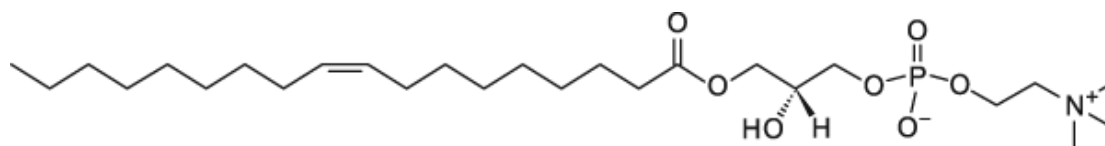


Fig. 6.5: Structure of 18:1 Lyso-PC

6.3.2 Preparation of invasomes

POPC-invasomes (composition as table 6.1) were prepared by the conventional mechanical dispersion method. Briefly, lipids were dissolved in a chloroform and methanol (2:1) mixture. Organic solvent was then removed by rotary evaporation (Rotavapor R - 114, BÜCHI) above the lipid transition temperature (-2°C). The deposited lipid film was hydrated with buffer at the room temperature. Resulting vesicles were allowed to swell for half an hour at room temperature. Then the suspensions was sonicated for 5 min and extruded through a 100 nm membrane (21 times) at room temperature.

Table 6.1: The composition of POPC-Invasomes

Component	POPC (mg/ml)	LPC (mg/ml)	Buffer pH 7.4
Invasomes	100	7	Up to 1gm

Terpene mixture - 1% (terpene mix contains citral:cineole:d-limonene in the ratio 45:45:10)

Ethanol – 10%

Invasomes used for SERS measurements replaced POPC with POPC-d31.

Chapter 6

6.3.3 Skin preparation

Female human abdominal skin obtained from plastic surgery was used. After the plastic surgery the subcutaneous fatty tissue was removed from the skin by using a scalpel and surgical scissors and then frozen at -20 °C with aluminum foil packed for later use. Skin from only one patient will be used for all the experiment to avoid variability. Before the skin experiment the skin disks of 36 mm were punched out, cleaned with PBS (pH 7.4, 50 mM) and allowed to thaw with the SC side up open to the atmosphere and the dermal side bathed with receptor medium overnight at 4°C. After that the integrity of skin disks was checked with transepidermal water loss (TEWL) measurement (VapoMeter, Delfin Technology Ltd., Kuopio, Finland) to ensure that samples were free from any surface irregularities such as tiny holes or crevices.

6.3.4 Franz diffusion cell preparation

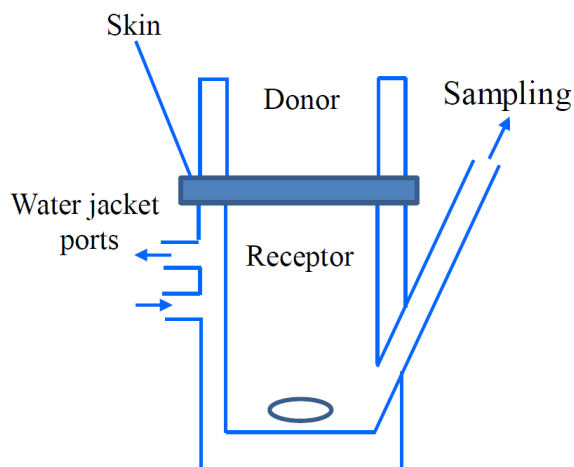


Fig. 6.6: Schematic representation of a Franz diffusion cell

In vitro skin penetration study was done using Franz diffusion cells (fig 6.6). For the skin experiments the formulation was applied non-occlusively and the cell was maintained at $37 \pm 1^\circ\text{C}$ throughout experiments by circulating warm water through the jacket of the Franz cell, in order to maintain the skin surface at 32°C . The effective penetration area and receptor cell volume were 3.14 cm^2 and 15.0 ml , respectively. The acceptor compartment will be filled with PBS buffer (pH 7.4) as the receptor medium. Skin is mounted, with the SC side up and the donor compartment left dry and open to atmosphere for half an hour

Chapter 6

before application of test formulation. Caution is taken to remove all air bubbles between the underside of the skin (dermis) and the acceptor solution. Also the skin will be stretched in all directions to avoid the presence of furrows. In the case of finite dosage application, 10 $\mu\text{L}/\text{cm}^2$ of the test formulation were applied to the skin surface by a pipette and homogenously distributed by an inoculating loop (1 μL , VWR[®] International, GmbH, Darmstadt, Germany). The incubation time of the skin with different test formulations will be 12 h. Then the formulations will be removed from the skin by washing five times with warm (45°C) receptor medium. After cleaning, the skin will be transferred for tape-stripping the SC.

6.3.5 Tape Stripping of the SC

The SC was removed by tape stripping, fig. 6.7. Tape stripping is a technique which can be used to progressively remove layers of stratum corneum which are then used for monitoring the penetration of the formulation within the SC.

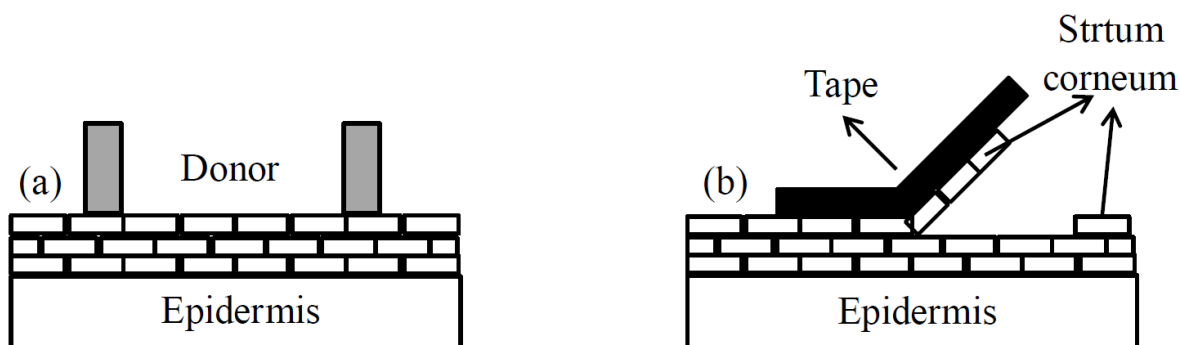


Fig. 6.7: Schematic representation of the method of tape stripping. After application of formulation at the donor site (a) and removal of the formulation, the SC is progressively removed by tape stripping (b).

6.3.6 AFM, SERS and TERS measurements

All the AFM, SERS and TERS measurements were performed in setup 1. The setup has introduced in chapter 3. The wavelength of the laser used in this setup is 530.8 nm. Control SC were removed from the surface of skin layer by layer by double side sticky tape (tape stripping) and then pasted to the cover slide surface (see fig. 6.8) for AFM and TERS measurements. Invasomes treated sample was prepared firstly by franz diffusion cell for the penetration of the invasomes into the SC and then by tape stripping for AFM and TERS

Chapter 6

measurements. For TERS measurement on control SC, the power of the laser was 900 μW , and the acquisition time was 10 s, while for TERS measurement on invasomes treated SC, the power was 1100 μW , and the acquisition time was 3 s.

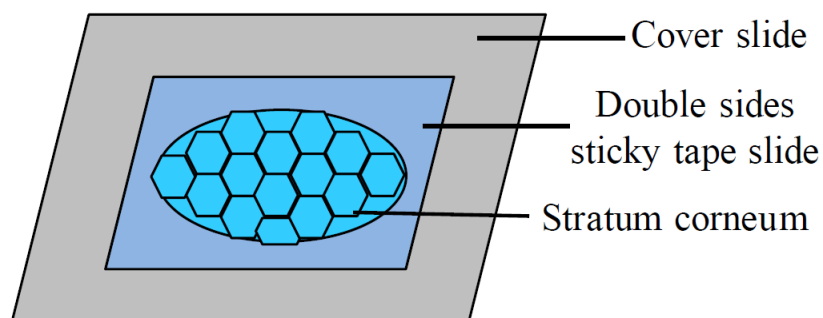


Fig. 6.8: The preparation of SC for AFM and TERS measurement.

For SERS measurements on invasomes, a silver island film evaporated on glass cover slide surface was used as substrate (the substrate preparation method has been mentioned in chapter 3). 40 μL of 10 $\mu\text{g}/\mu\text{L}$ invasomes aqueous dispersion was dropped on the substrate surface, incubated for 30 min and then washed using bidistilled water three times and dried in argon. The laser power for the SERS measurement was 300 μW and the acquisition time 5s.

6.4 Results and discussion

6.4.1 AFM measurements on control and invasomes treated SC

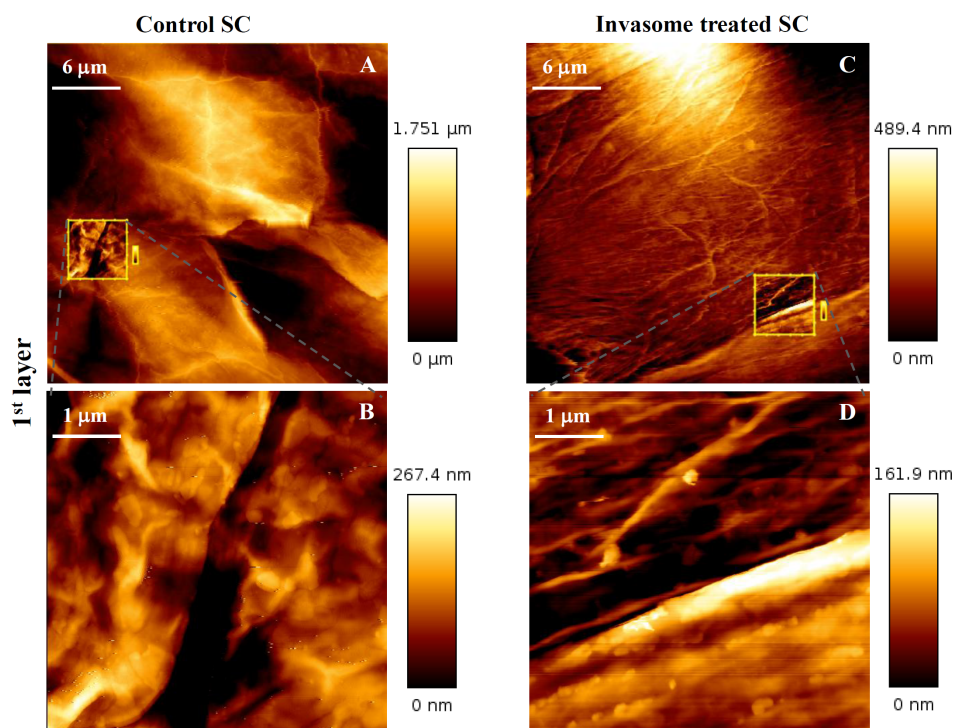


Fig. 6.9.1: AFM topography images of the control (left column, A, B) and invasomes treated (right column, C, D) stratum corneum (SC) from 1st strip layer. The figures on bottom (B, D) are the zoom-in regions in their corresponding on top figures (A, C).

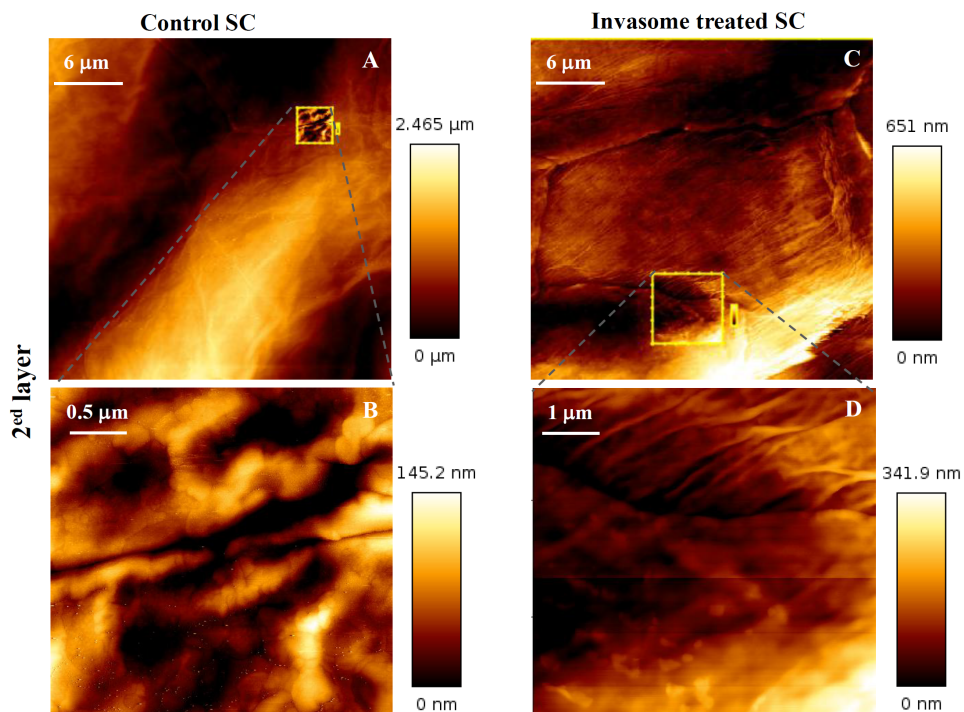


Fig. 6.9.2: AFM topography images of the control (left column, A, B) and invasomes treated (right column, C, D) SC from 2nd strip layer.

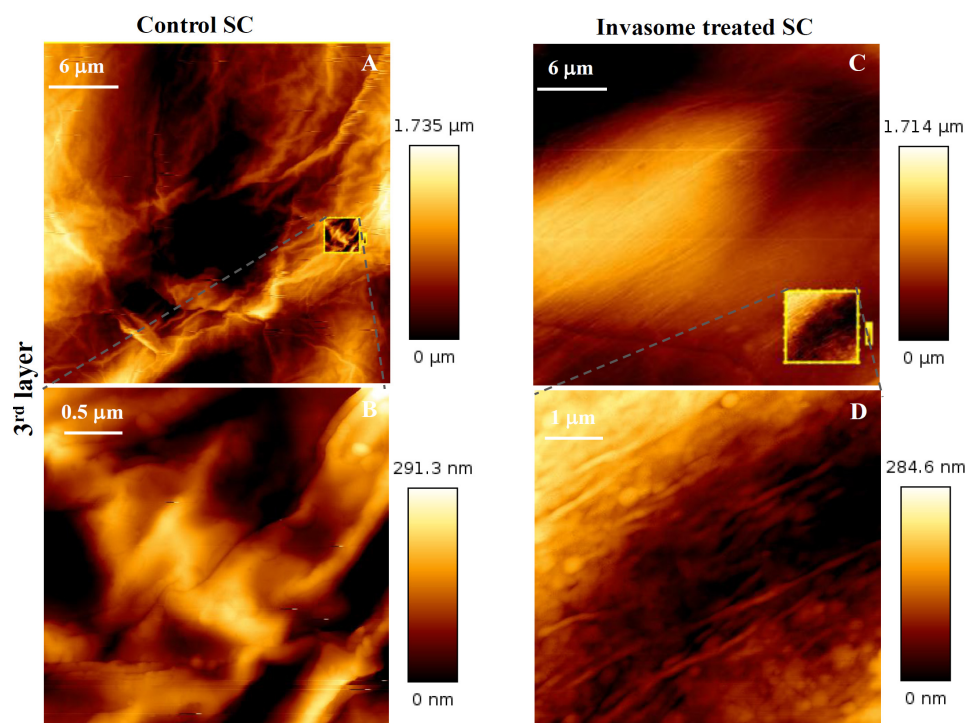


Fig. 6.9.3: AFM topography images of the control (left column, A, B) and invasomes treated (right column, C, D) SC from 3rd strip layer.

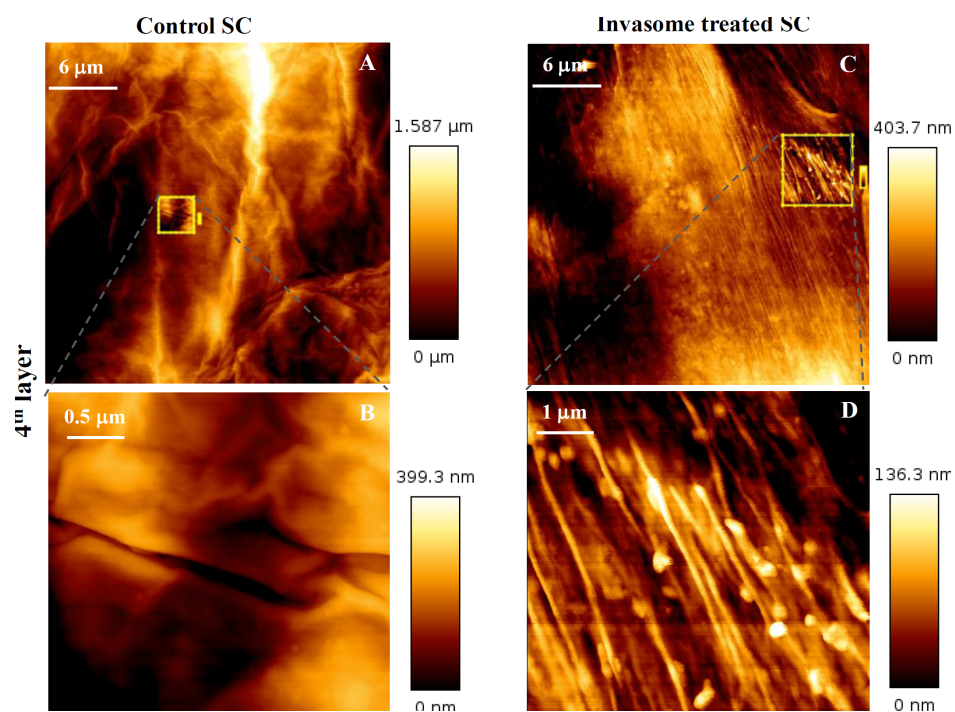


Fig. 6.9.4: AFM topography images of the control (left column, A, B) and invasomes treated (right column, C, D) SC from 4th strip layer.

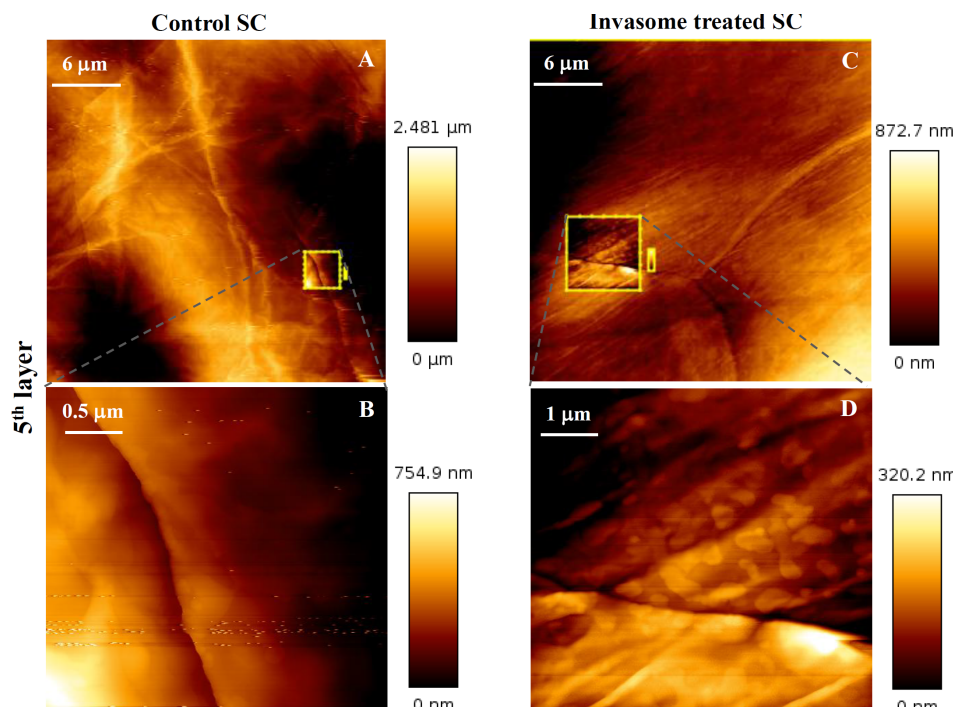


Fig. 6.9.5: AFM topography images of the control (left column, A, B) and invasomes treated (right column, C, D) SC from 5th strip layer.

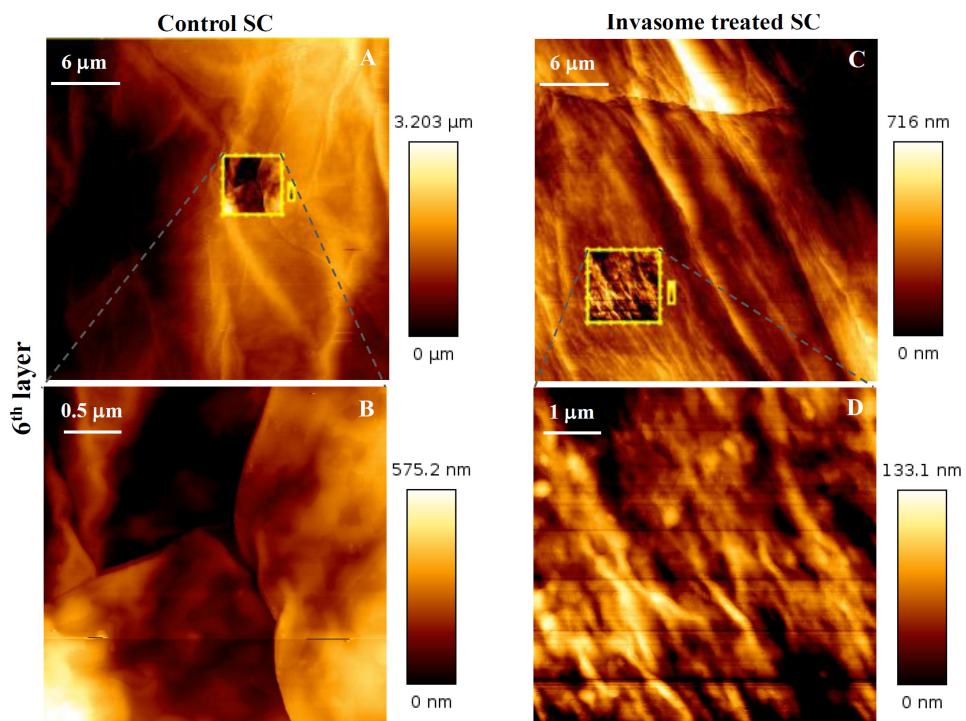


Fig. 6.9.6: AFM topography images of the control (left column, A, B) and invasomes treated (right column, C, D) SC from 6th strip layer.

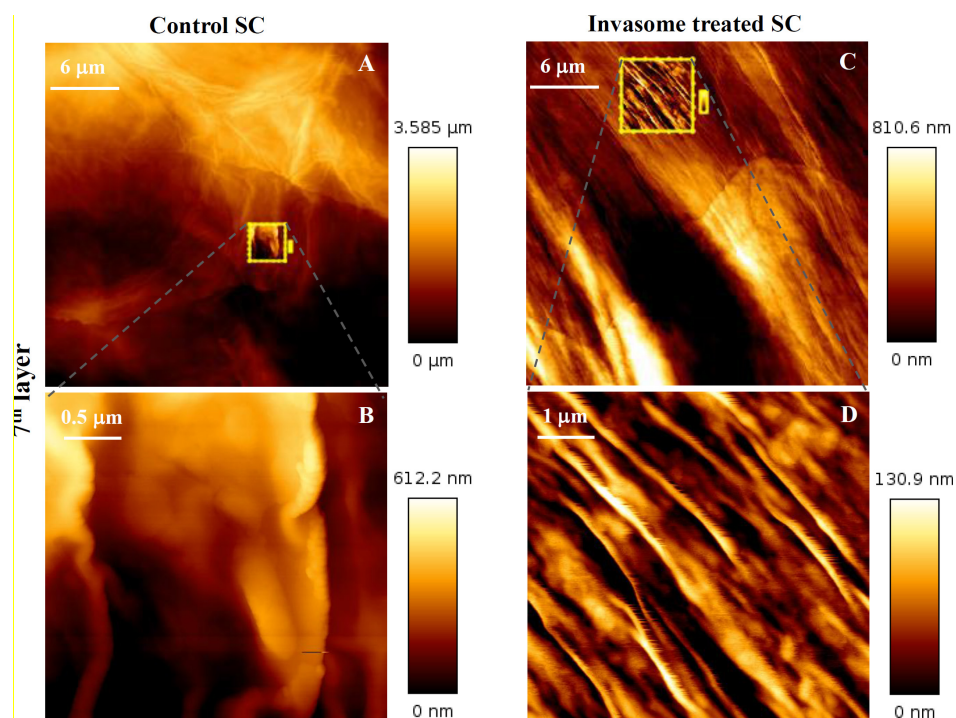


Fig. 6.9.7: AFM topography images of the control (left column, A, B) and invasomes treated (right column, C, D) SC from 7th strip layer.

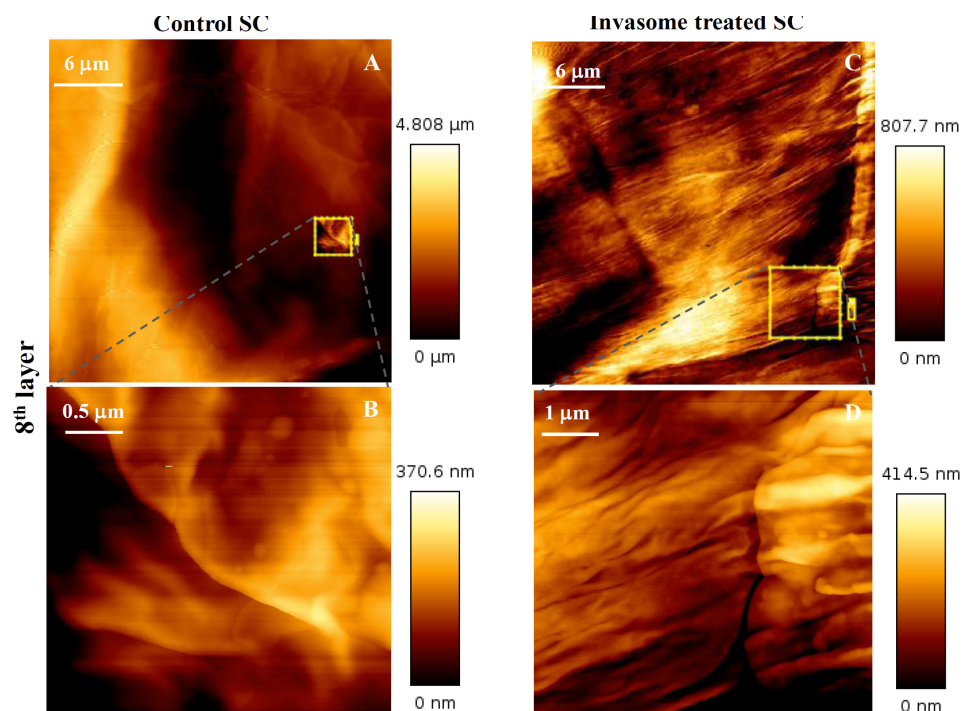


Fig. 6.9.8: AFM topography images of the control (left column, A, B) and invasomes treated (right column, C, D) SC from 8th strip layer.

Chapter 6

Fig. 6.9 shows the AFM topography images of control and invasomes treated skin samples from the skin surface to the 8th strip layer. The SC was removed by tape stripping with a thickness of 1.0 - 1.5 μm for each layer. There are subtle differences in the topography of the corneocytes by comparing the control and the invasomes treated SC. The AFM images of the invasomes treated 4th strip layer SC for example, shows some nanoparticles and cavities on the surface, which are especially clear on the enlarged image on the bottom. The nanoparticles are about 100-200 nm in lateral and 100-150 nm in vertical, which corresponds well with the size of the invasomes and could be assigned to invasome vesicles by topography. However, the component of the nanoparticles is not clear so far and needs to be further identified by TERS. The size of the cavities is a bit larger than that of the nanoparticles, which could be attributed to the traces left by invasomes when they penetrated into the SC. Concerning on the penetration depth, the invasome-like nanoparticles can be found from the first to the 7th strip layer but vanished on the 8th strip layer. From all these morphology changes, it is probable that invasomes act as drug carrier systems by which intact vesicles can enter the SC about 7.0 – 10.0 μm underneath the surface.

6.4.2 Spectra measurements

To confirm if the vesicle like structures in the topography images are really invasomes, SERS measurements were performed on invasomes, and TERS measurements were performed on the second layer of the control and invasomes treated SC respectively. If the bands from invasomes could also be detected on invasomes treated SC, then we can come to the conclusion that the vesicles-like nanoparticles are invasomes.

Fig. 6.10 shows SERS spectra of the invasomes adsorbed on silver islands substrate surface. Spectral features at 966 cm^{-1} , 1130 cm^{-1} , 1152 cm^{-1} , and 1507 cm^{-1} are used as marker bands to trace the invasomes.

Fig. 6.11 shows the TERS measurement on the 2nd strip layer of the control SC. (A) is the topography image and (B) is the spectra measured on the positions indicated in (A) with a step-size of 10 nm. Corneocytes show homogeneous topography while no topographic

Chapter 6

signatures of invasomes can be found in the AFM image. The TERS spectra can be assigned to either lipid or proteins while no spectral signatures of the four marker bands from the invasomes can be found.

Fig. 6.12 shows the TERS measurement on the 2nd strip layer of the invasomes treated SC. (A) is the topography image, (B) is the height profile through the nanoparticle along the line indicated in (A), and (C) is the spectra measured on the positions indicated in (A) with a step-size of 10 nm. In the AFM image, the nanoparticle shows a size of about 200 nm in lateral and 100 nm in vertical dimension, which indicates a distinct vesicular structure of invasomes. Furthermore, the four marker bands from invasomes are found in the TERS spectra which suggests the present of invasomes in the treated stratum corneum

The assignment of all the spectra is in table 6.2 (23-25).

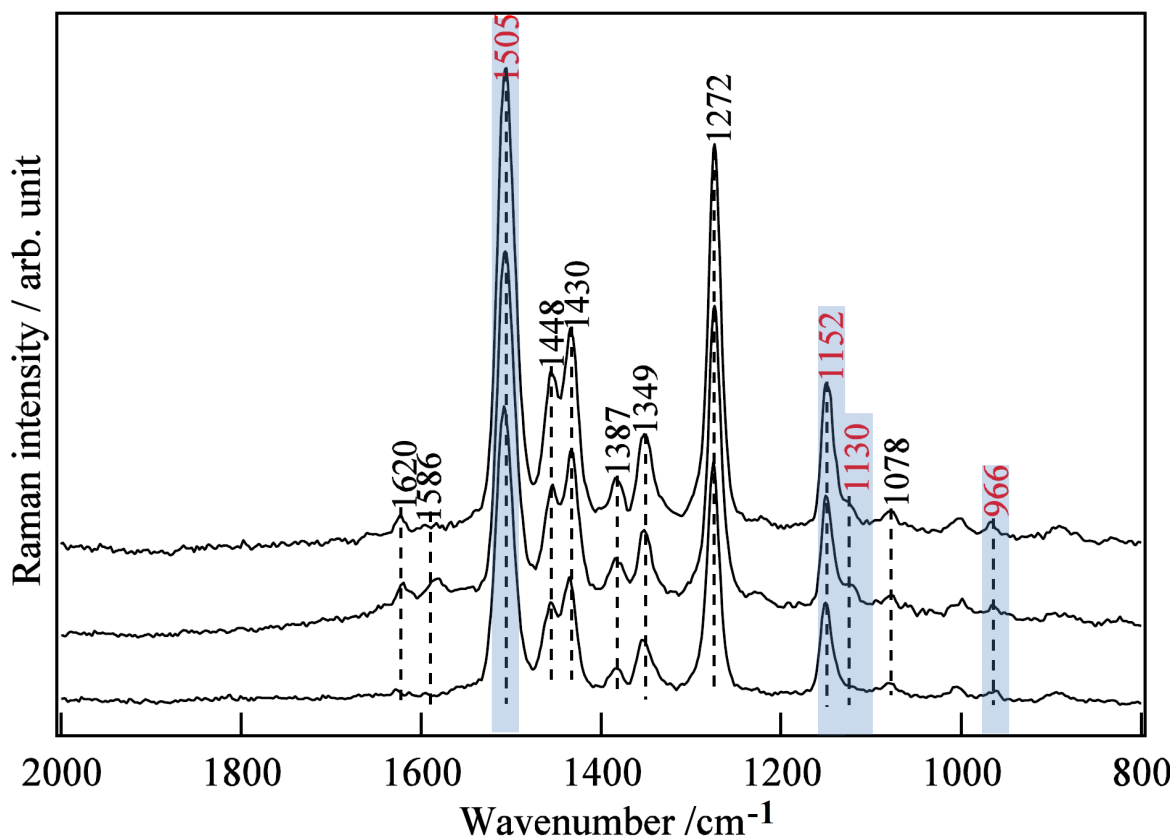


Fig. 6.10: SERS spectra of invasomes on different positions on the silver island substrate surface.

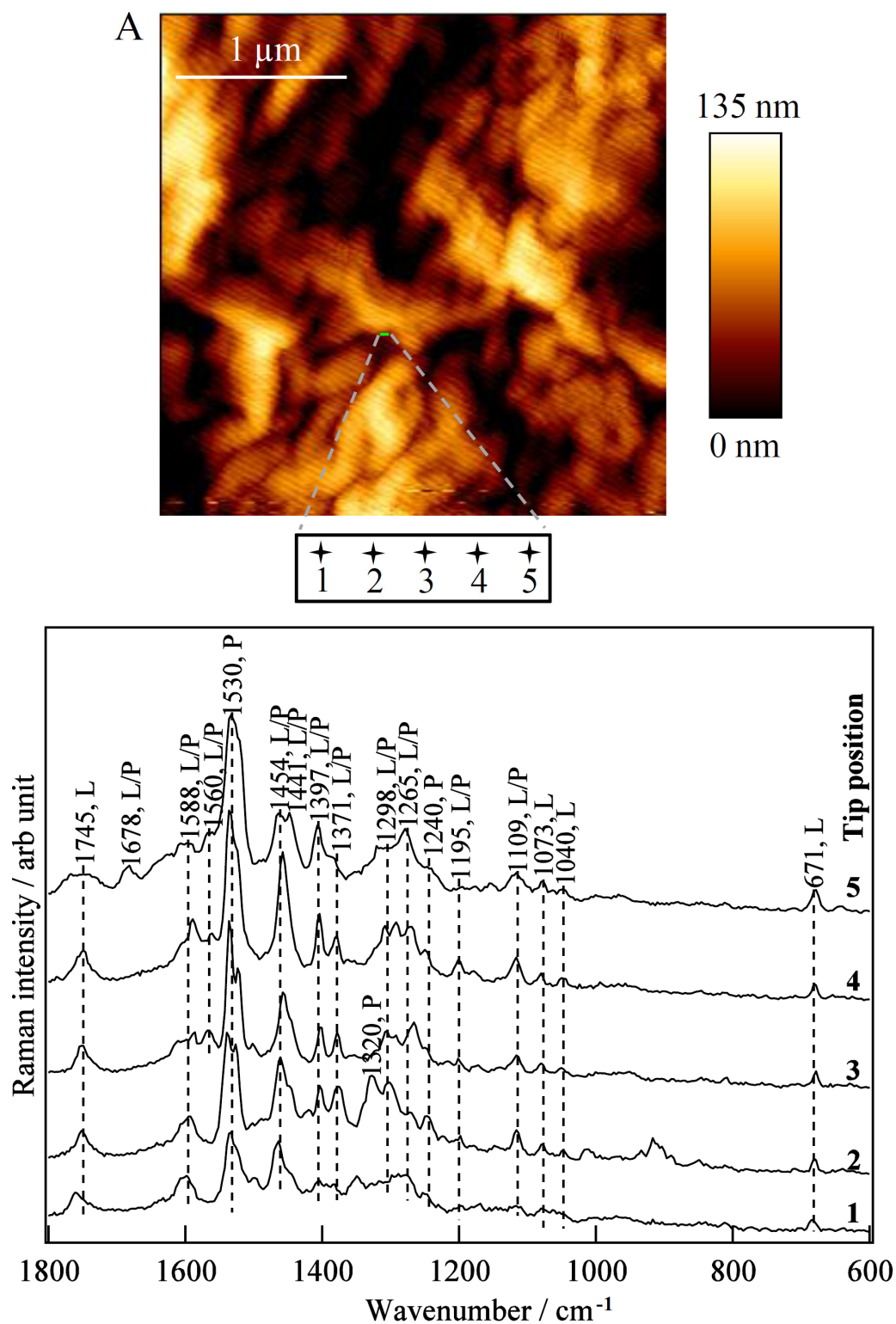


Fig. 6.11: TERS measurement on the control SC (2^{ed} layer). (A) AFM topography images and (B) five TERS spectra obtained on the positions indicated in (A) with a step-size of 10 nm.

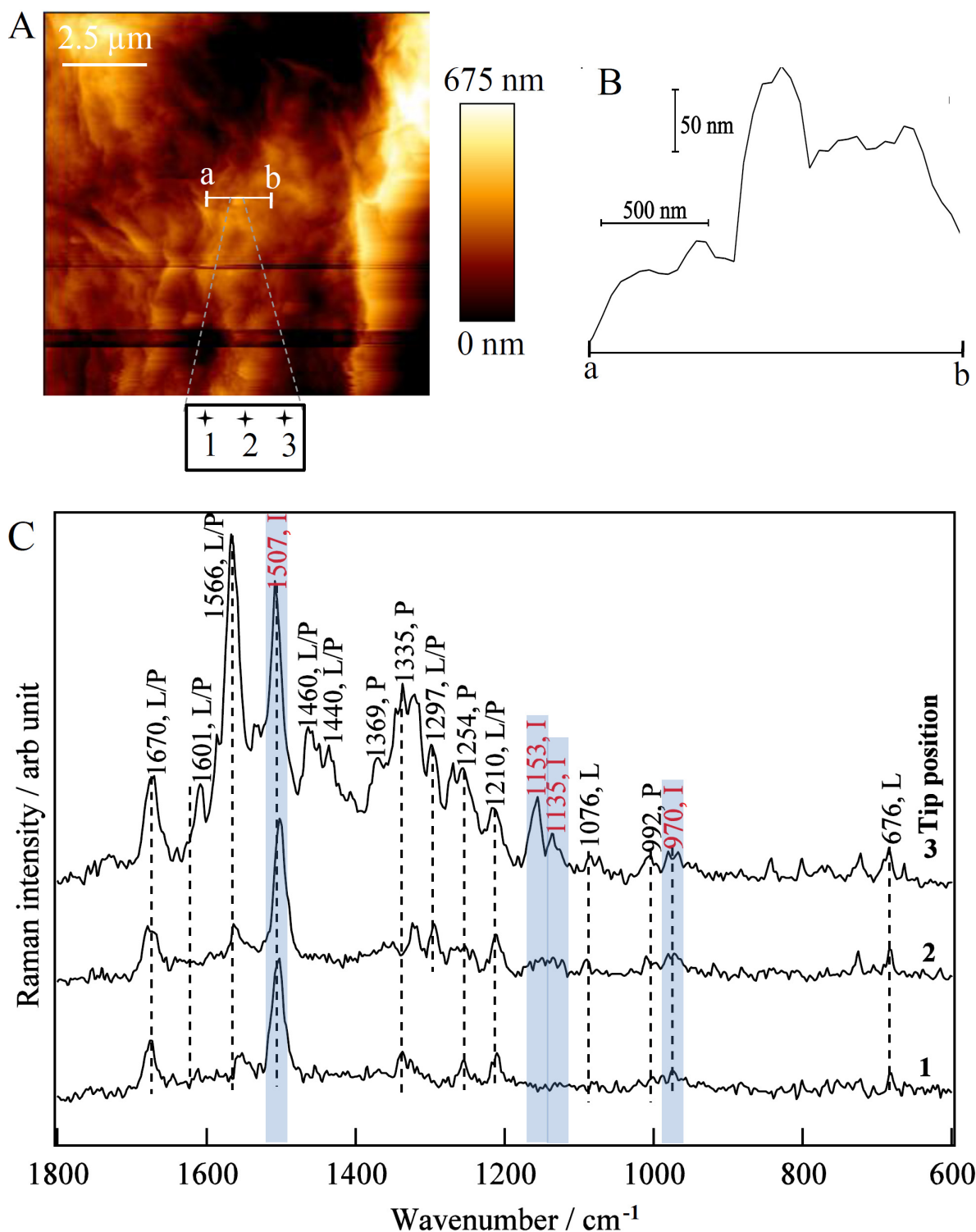


Fig. 6.12: TERS measurement on the invasomes treated SC (2nd layer). (A) AFM topography images, (B) the height profile through the nanoparticle along the line indicated in (A), and (C) three TERS spectra obtained on the positions indicated in (A) with a step-size of 10 nm.

Chapter 6

Table 6.2: Tentative assignment of the SERS spectra from invasomes, TERS spectra from control and invasomes treated SC (23-25).

SC (TERS)	Invasome (SERS)	1 (TERS)	2 (TERS)	3 (TERS)	Tentative assignment
671					Cholesterol
	966	973	970	970	$\delta(=CH)$ (I)
			992	992	Phe (P)
1040					$\nu(C-O-P)$ (L)
1073	1078				$\nu_s(PO_2^-)$, $\nu_s(CO-C-O)$ (L)
1109					$\nu(C-C)$ (L), $\nu(C-N)$ (P)
	1130			1135	$\nu(C-C)$ (I)
	1152			1153	$\nu(CO-O-C)$ (I)
1195		1210	1210	1210	$\nu_{as}(CO-C-O)$ (L), Phe, Tyr, Val (P)
1240		1253		1254	Amide III(P)
1265	1272				Amide III(P), $\delta_{ip}(=CH)$ (L)
1298			1292	1297	$\delta_{twist}(CH_2)$ (L, P)
1320		1335	1325	1335	$\delta(CH)$ Ser (P)
	1349				$\delta(CH)$, $\delta(OH)$ (I)
1371				1369	$\rho(CH)$, (CH_2) wag (L, P)
1397	1387				(CH_2) wag, $\rho(CH_3)$ (L, P)
	1430				$\delta(CH_2)$, $\delta(CH_3)$ (I)
1441	1448			1440	$\delta(CH_2)$, $\delta(CH_3)$ (L, P)
1454				1460	$\delta(CH_2)$, $\delta(CH_3)$ (L,P)
	1505	1507	1507	1507	$\delta(NH_2)$ (I)
1530					Amide II (P)
1560		1566	1566	1566	$\delta(NH_2)$ (L), Amide II (P)
1588	1586			1601	$\nu(C=C)$ (L), Phe, Trp, Tyr (P)
	1620				$\delta(NH_3^+)$ (I)
1678		1670	1670	1670	$\nu(C=C)$ (L), Amide I (P)
1745					$\nu(C=O)$ (L)

Abbreviations: L: lipid; P: protein; ν : stretching; δ : deformation; s: symmetric; as: asymmetric.

6.5 Conclusion and outlook

In this chapter, by analyzing AFM topography images of control and invasomes treated SC from the top surface to the 8th strip layer, SERS spectra of invasomes and AFM topography in combination with TERS spectra on the second strip layer of control and invasomes treated SC, it was found that invasomes probably act as drug carrier systems penetratig 7-

Chapter 6

10 μm into the SC. These results are primary. For fully and systematically understand the penetration mechanism of invasomes, more measurements with respect to statistic relevant data are necessary.

6.6 References

1. R. Mendelsohn, C. R. Flach, D. J. Moore, Determination of molecular conformation and permeation in skin via IR spectroscopy, microscopy, and imaging. *Biochimica Et Biophysica Acta-Biomembranes* **1758**, 923 (2006).
2. C. H. Xiao, D. J. Moore, M. E. Rerek, C. R. Flach, R. Mendelsohn, Feasibility of tracking phospholipid permeation into skin using infrared and raman microscopic imaging. *Journal of Investigative Dermatology* **124**, 622 (2005).
3. C. H. Xiao, D. J. Moore, C. R. Flach, R. Mendelsohn, Permeation of dimyristoylphosphatidylcholine into skin - Structural and spatial information from IR and Raman microscopic imaging. *Vibrational Spectroscopy* **38**, 151 (2005).
4. G. L. Flynn, Cutaneous and transdermal delivery: Processes and systems of delivery. *In Modern Pharmaceutics*, Banker, G.S & Rhodes, C.T, eds. New York, 239 (1996).
5. P. M. Elias, Plastic Wrap Revisited - the Stratum-Corneum 2-Compartment Model and Its Clinical Implications. *Archives of Dermatology* **123**, 1405 (1987).
6. N. Dayan, Pathways for Skin Penetration. *Cosmetics & Toiletries® magazine* **120**, 67 (2005).
7. B. Bhushan, Nanotribological and nanomechanical properties of skin with and without cream treatment using atomic force microscopy and nanoindentation. *Journal of Colloid and Interface Science* **367**, 1 (2012).
8. P. Morganti, E. Ruocco, R. Wolf, V. Ruocco, Percutaneous absorption and delivery systems. *Clinics in Dermatology* **19**, 489 (2001).
9. K. D. McCarley, A.L. Bunge, Review of pharmacokinetic models of dermal absorption. *Journal of Pharmaceut Science* **90**, 1699 (2001).
10. P. M. Elias, Epidermal lipids, barrier function, and desquamation. *Journal of Investigative Dermatology* **80**, S44 (1983).
11. J. Hadgraft, Modulation of the barrier function of the skin. *Skin Pharmacology and Applied Skin Physiology* **14**, 72 (2001).
12. J. de Leeuw, H. C. de Vijlder, P. Bjerring, H. A. M. Neumann, Liposomes in dermatology today. *Journal of the European Academy of Dermatology and Venereology* **23**, 505 (2009).
13. M. B. Brown, G. P. Martin, S. A. Jones, F. K. Akomeah, Dermal and transdermal drug delivery systems: Current and future prospects. *Drug Delivery* **13**, 175 (2006).
14. G. Cevc, U. Vierl, Nanotechnology and the transdermal route A state of the art review and critical appraisal. *Journal of Controlled Release* **141**, 277 (2010).
15. M. Goodman, B. W. Barry, Action of Penetration Enhancers on Human-Skin as Assessed by the Permeation of Model-Drugs 5-Fluorouracil and Estradiol .1. Infinite Dose Technique. *Journal of Investigative Dermatology* **91**, 323 (1988).
16. A. C. Williams, B. W. Barry, Penetration enhancers. *Advanced Drug Delivery Reviews* **56**, 603 (2004).
17. N. A. Megrab, A. C. Williams, B. W. Barry, Estradiol Permeation through Human Skin and Silastic Membrane - Effects of Propylene-Glycol and Supersaturation. *Journal of Controlled Release* **36**, 277 (1995).
18. A. Nanda, S. Nanda, N. M. K. Ghilzai, Current developments using emerging transdermal technologies in physical enhancement methods. *Current drug delivery* **3**, 233 (2006).

Chapter 6

19. M. J. Hope, C. N. Kitson, Liposomes - a Perspective for Dermatologists. *Dermatologic Clinics* **11**, 143 (1993).
20. N. Weiner *et al.*, Liposomes - a Novel Topical Delivery System for Pharmaceutical and Cosmetic Applications. *Journal of Drug Targeting* **2**, 405 (1994).
21. N. Dragicevic-Curic, D. Scheglmann, V. Albrecht, A. Fahr, Temoporfin-loaded invasomes: Development, characterization and in vitro skin penetration studies. *Journal of Controlled Release* **127**, 59 (2008).
22. M. M. A. Elsayed, O. Y. Abdallah, V. F. Naggar, N. M. Khalafallah, Deformable liposomes and ethosomes as carriers for skin delivery of ketotifen. *Pharmazie* **62**, 133 (2007).
23. R. Boehme *et al.*, Towards a specific characterisation of components on a cell surface - combined TERS-investigations of lipids and human cells. *Journal of Raman Spectroscopy* **40**, 1452 (2009).
24. R. Boehme *et al.*, Biochemical imaging below the diffraction limit - probing cellular membrane related structures by tip-enhanced Raman spectroscopy (TERS). *Journal of Biophotonics* **3**, 455 (2010).
25. M. Richter, M. Hedegaard, T. Deckert-Gaudig, P. Lampen, V. Deckert, Laterally Resolved and Direct Spectroscopic Evidence of Nanometer-Sized Lipid and Protein Domains on a Single Cell. *Small* **7**, 209 (2010).

Chapter 7 Summary and Outlook

In the present thesis the advantages of high spectral specificity, sensitivity and super high lateral resolution tip-enhanced Raman spectroscopy (TERS) has been applied for the investigation of biomolecules at the nanometer/sub-nanometer scale.

TERS for label-free DNA sequencing

TERS measurements on different RNA/DNA single strands have been performed to investigate the feasibility of TERS as a label-free DNA sequencing method. First TERS experiments on uracil homopolymer strands clearly demonstrated the reproducibility of this technique in terms of consistent spectra.

In TERS spectra from calf thymus DNA all four DNA nucleobases were assigned and a sequence change underneath the tip could be assumed.

The investigations were extended to specifically for this work synthesized DNA samples. In the obtained TERS spectra from $(A_{10}C_{15})_8$ DNA strands the distinction of adenine and cytosine nucleobases was possible with a sub-nanometer spatial resolution.

From these results it could be concluded that TERS has the potential to directly sequence DNA / RNA strands, which could also be utilized for other chainlike bio-macromolecules (e.g. proteins). In future projects TERS will be applied to synthetic DNA strands with a known sequence containing all four nucleobases. The ultimate goal is the examination of strands with an unknown nucleobase order.

TERS for the direct detection of 5-methylcytosine sites on DNA strands

TERS measurements on methylated DNA single strands $(A_{10}5meC_{10})_4$ have been performed for the first time. The obtained spectra show strikingly different vibrational modes for adenine and 5-methylcytosine, determined by distinct marker bands. Moreover, TERS spectra of cytosine in the unsubstituted DNA $(A_{10}C_{15})_8$ can be easily distinguished from 5-methylcytosine in the methylated DNA $(A_{10}5meC_{10})_4$ by bands arising from the methyl group. These results clearly demonstrate the direct detection and localization of 5-methylcytosine sites in DNA strands with TERS at sub-nanometer resolution. Simultaneously, the nucleobase can be distinguished from its non-substituted analogue. Further examinations in this research area will concentrate on the identification of nitrogen-

Chapter 7

methylated bases (N-4-methylcytosine, N-6-methyladenine). The aim will be the localization of such substituted sites in the strand, a possible step forward to clinical diagnostic and therapy.

AFM-TERS investigations on skin penetration of invasomes

AFM and TERS measurements have been performed on different layers (by tape stripping) of untreated and invasomes treated outermost skin layers (stratum corneum, SC). It was shown that invasomes likely act as drug carrier systems by which intact vesicles can penetrate 7-10 μm into the SC. The invasomes were identified spectroscopically and thus could be discriminated from their environment (SC). The obtained primary results show the potential of TERS to studying the mechanism of skin penetration of invasomes. For a systematic study in this area more measurements with respect to statistic relevant data are necessary.

In conclusion, the results presented in this thesis demonstrate the potential of tip-enhanced Raman spectroscopy (TERS): on the one hand it is suitable for a label-free sequencing of DNA/RNA strands. On the other hand the direct detection of methylation sites on DNA strands is feasible. Last but not least it was shown that with TERS the mechanism of skin penetration of invasomes can be studied. All these results demonstrate that the special attributes of TERS (nanometer/sub-nanometer lateral resolution, high sensitivity and specificity) enable numerous investigations in biosciences to answer raised questions.

Publications and manuscripts in preparation

- [1]. R. Treffer, **X.-M. Lin**, E. Bailo, T.-Deckert. Gaudig, V. Deckert, Distinction of Nucleobases – a Tip-enhanced Raman Approach, *Beilstein J. Nanotechnol*, **2011**, **2**, **628–637**.
- [2]. R. Treffer, R. Böhme, T.-Deckert. Gaudig, K. Lau, S. Tiede, J. Klöpper, **X.-M. Lin**, V. Deckert, Advances in Tip-enhanced Raman Scattering (TERS) for Biochemical Applications, *Biochem. Soc. Trans.*, **2012**, **40**, **609-914**.
- [3]. **X.-M. Lin**, P. Singh, R. Treffer, T.-Deckert. Gaudig, V. Deckert, Sub-nanometer Differentiation on a DNA Strand by Tip-enhanced Raman Spectroscopy, *submitted*.
- [4]. **X.-M. Lin**, R. Treffer, T.-Deckert. Gaudig, V. Deckert, Scanning Near-field Optical Microscopy (SNOM) for Biochemical Applications, *submitted*.
- [5]. **X.-M. Lin**, R. Treffer, T.-Deckert. Gaudig, M. Zeisberger, V. Deckert, Feasibility Evaluation of Tip-Enhanced Raman Scattering (TERS) as a Label-Free DNA Sequencing Method, *in preparation*.
- [6]. **X.-M. Lin**, T.-Deckert. Gaudig, V. Deckert, TERS on Direct Detection of 5-methylcytosine Sites on DNA Strands, *in preparation*.

Conference Posters

- [1]. **X.-M. Lin**, T.-Deckert. Gaudig, R. Treffer, V. Deckert, Tip-Enhanced Raman Scattering (TERS) Of Uracil Strands, the XXII International Conference on Raman Spectroscopy, Boston, America, August 8th – 13th, 2010.
- [2]. R. Treffer, **X.-M. Lin**, V. Deckert, Tip-enhanced Raman Scattering on DNA and RNA Strands, the 11th International Conference on Near-Field Optics, Nanophotonics and Related Techniques (NFO-11), Beijing, China, August 29th - September 2nd, 2010.
- [3]. **X.-M. Lin**, T.-Deckert. Gaudig, R. Treffer, V. Deckert, Tip-Enhanced Raman Scattering (TERS) Of Calf Thymus DNA, ANAKON 2011, ETH in Zurich, Switzerland, March 22nd–25th, 2011.

Publications & manuscripts

[4]. **X.-M. Lin**, T.-Deckert. Gaudig, R. Treffer, V. Deckert, Tip-Enhanced Raman Scattering (TERS) Of Calf Thymus DNA, the Molecular Plasmonics 2011, Jena, Germany, May 19th-21st.

[5]. **X.-M. Lin**, R. Treffer, T.-Deckert. Gaudig, V. Deckert, Distinction of Nucleobases – a Tip-Enhanced Raman Approach, The 8th Workshop of FT-IR Spectroscopy in Microbiological and Medical Diagnostics, Robert Koch-Institute, Berlin, Germany, October 20th-21st, 2011.

[6]. **X.-M. Lin**, T.-Deckert. Gaudig, V. Deckert, Detection of Methylation Sites on DNA Using Tip-Enhanced Raman Spectroscopy, the 23rd International Conference on Raman Spectroscopy, Bangalore, India, August 12th – 17th, 2012.

Ort, Datum

Unterschrift

Acknowledgements

Acknowledgements

This thesis covers my three and half years of PhD work, which contains both theoretical understanding and experimental finding focusing on my research field. Besides, those unselfish help and supports are absolutely necessary in the whole work that will be presented. I would like to acknowledge the following people, without whom I could not proceed my work.

I would like to thank my PhD supervisor Dr. Volker Deckert for three and a half years continual support and encouragement. I thank him for guiding me in the field of both TERS and biochemistry. Through Volker's supervision, I have gained skills and experience that will certainly benefit my future career.

I would like to thank Dr. Tanja Deckert-Gaudig for many good suggestions, support and encouragement in both my work and life. I thank her for training me on operating the TERS instrument and for correcting my manuscripts and thesis.

I thank Prof. Dr. Jürgen Popp for his support and help during my study in IPHT and IPC.

I thank Prof. Dr. Alfred Fahr for the collaboration and discussion on the skin project.

I thank Mr. Konstantin Kirsch and Dr. Henrik Schneidwind for coating nice TERS tips and SERS substrates for all my measurements.

I thank my colleague Rene Bohme for training me on using the AFM setup at the very beginning of my study and suggestions during my measurements. I thank Ming Chen and Mukul Ashtikar for the collaboration on the skin project. They prepared the invasomes and skin samples for our measurements and gave lots constructive suggestions on the proceeding of this project. I thank my colleague Prabha Singh for the proof reading of this work and kind help in my life. I must also thank all my other colleagues who have given me help throughout my PhD.

Acknowledgements

At the end, I would like to thank my husband, my parents, my parents in law, my sisters, and all my friends for the endless love and the encouragement on both of my life and studies abroad.

Selbstständigkeitserklärung

Selbstständigkeitserklärung

Ich erkläre, dass ich die vorliegende Arbeit selbstständig und unter Verwendung der angegebenen Hilfsmittel, persönlichen Mitteilungen und Quellen angefertigt habe.

Ort, Datum

Unterschrift

Curriculum vitae

Curriculum vitae

Personal Data

Name: Xiu-Mei Lin

Gender: Female; Date of birth: 29. 09. 1982

Place of birth: Putian City, Fujian Province, People's Republic of China

Nationality: People's Republic of China

Education

PhD: 06.2009 – 02.2013:

Institute of Photonic Technology (IPHT), Germany

Institute for Physical Chemical (IPC), University of Jena, Germany

PhD thesis: Tip-enhanced Raman Spectroscopy (TERS) for Biomolecular Analysis at
Nanometer / Sub-nanometer Scale

Master of Science: 09. 2005 – 03. 2009

Department of Chemistry, College of Chemistry and Chemical Engineering, Xiamen
University, China

Master thesis: Fabrication and Characterization of Surface-enhanced Raman Scattering
(SERS) Substrates with Highly Uniform SERS Activity and Study the
Enhanced Raman Effect of Microspheres due to Formed Near-field Nanojets

Bachelor of Science: 09. 2001 – 07. 2005

Department of Chemistry, Zhangzhou Normal University, Fujian, China

School:

09. 1998 – 07. 2001, the First Senior High School of Putian, Fujian, China

09. 1995 – 07. 1998, the First Junior High School of Putian, Fujian, China

09. 1990 – 07. 1995, YangCheng Primary School, Putian, Fujian, China

Ort, Datum

Unterschrift